Improved vertical scanning interferometry

INFORMATION TO USERS

This manuscript has been reproduced from the microfilm master. UMI films the text directly from the original or copy submitted. Thus, some thesis and dissertation copies are in typewriter face, while others may be from any type of computer printer.

The quality of this reproduction is dependent upon the quality of the copy submitted. Broken or indistinct print, colored or poor quality illustrations and photographs, print bleedthrough, substandard margins, and improper alignment can adversely affect reproduction.

In the unlikely event that the author did not send UMI a complete manuscript and there are missing pages, these will be noted. Also, if unauthorized copyright material had to be removed, a note will indicate the deletion.

Oversize materials (e.g., maps, drawings, charts) are reproduced by sectioning the original, beginning at the upper left-hand corner and continuing from left to right in equal sections with small overlaps.

Photographs included in the original manuscript have been reproduced xerographically in this copy. Higher quality 6" x 9" black and white photographic prints are available for any photographs or illustrations appearing in this copy for an additional charge. Contact UMI directly to order.

UMI®

IMPROVED VERTICAL SCANNING INTERFEROMETRY

by

Akiko Harasaki

A Dissertation Submitted to the Faculty of the

COMMITTEE ON OPTICAL SCIENCES (GRADUATE)

In Partial Fulfillment of the Requirements
For the Degree of

DOCTOR OF PHILOSOPHY

In the Graduate College

THE UNIVERSITY OF ARIZONA

2 0 0 0

UMI®

THE UNIVERSITY OF ARIZONA ®
GRADUATE COLLEGE

As members of the Final Examination Committee, we certify that we have

read the dissertation prepared by___Akiko Harasaki_____

entitled_Improved Vertical Scanning Interferometry_____

_____

_____

_____

and recommend that it be accepted as fulfilling the dissertation

requirement for the Degree of _Doctor of Philosophy_____

James C. Wyant   March 9, 2000
_____   _____
James C. Wyant   Date

Jack D. Gaskill   March 9, 2000
_____   _____
Jack D. Gaskill   Date

William J. Dallas   March 9 2000
_____   _____
William J. Dallas   Date

_____   _____
                                                    Date

_____   _____
                                                    Date

Final approval and acceptance of this dissertation is contingent upon
the candidate's submission of the final copy of the dissertation to the
Graduate College.

I hereby certify that I have read this dissertation prepared under my
direction and recommend that it be accepted as fulfilling the dissertation
requirement.

James C. Wyant   James C. Wyant   March 21, 2000
_____   _____
Dissertation Director   Date

STATEMENT BY AUTHOR

This dissertation has been submitted in partial fulfillment of requirements for an advanced degree at The University of Arizona and is deposited in the University Library to be made available to borrowers under rules of the Library.

Brief quotations from this dissertation are allowable without special permission, provided that accurate acknowledgment of source is made. Requests for permission for extended quotation from or reproduction of this manuscript in whole or in part may be granted by the head of the major department or the Dean of the Graduate College when in his or her judgment the proposed use of the material is in the interests of scholarship. In all other instances, however, permission must be obtained from the author.

SIGNED: _Akiko Harasaki_

To Hirofumi and Haruko

ACKNOWLEDGEMENTS

TABLE OF CONTENTS

TABLE OF CONTENTS—*Continued*

TABLE OF CONTENTS—*Continued*

LIST OF TABLES

LIST OF FIGURES

LIST OF FIGURES—*Continued*

LIST OF FIGURES—*Continued*

LIST OF FIGURES—*Continued*

ABSTRACT

Vertical scanning interferometers are routinely used for the measurement of optical fiber connectors. There are increasing needs for measurements of such items as machined surfaces, contact lenses, paint texture, cell structure, and integrated circuit devices, to name a few. These structures have too much depth, or are too rough, to measure with standard interferometry methods. Phase-measurement interferometry methods are limited to surfaces that do not have any discontinuities larger than one quarter of the operating wavelength. On the other hand, vertical scanning interferometers can be very effective, even though they have low height resolution compared to that of phase-measurement interferometers. Improving the height resolution of vertical scanning interferometers from the point of hardware improvement and signal processing has been one of the major research interests in the surface metrology area. This work provides a new algorithm, which called here "PSI on the Fly" technique, as a solution for improving height resolution of vertical scanning interferometers.

This dissertation begins with a review of white-light interference microscopes. The height and lateral resolutions are derived based on scalar diffraction theory. Next, various well-established algorithms for finding a topographic map of the small object surface are discussed.

The work proceeds with a discussion of the phase change upon reflection and its influence on the coherence envelope. Then phase measurement interferometry methods are reviewed. The emphasis is in errors in phase measurement resulting from using a white light source instead of a monochromatic light source as in the usual case.

The following chapter describes and examines an often-observed artifact of vertical-scanning interferometry when applied to step heights. The artifact is called "bat wings" because of its appearance. The physical cause of the "bat wings" artifact is discussed through a diffraction model.

The next chapter proposes an improved vertical-scanning interferometry algorithm. The method, called here "PSI on the Fly" technique, has been developed by combining regular vertical-scanning interferometry and a monochromatic phase-shifting interferometry technique. The PSI on the Fly technique improves the surface height resolution of vertical scanning interferometry to that of a phase-shifting interferometry measurement. In addition to the resolution improvement, the algorithm also successfully removes the "bat wings" artifact.

INTRODUCTION

The modern electronics and signal processing theories of the past 20 years enable optical measurement of submicrometer features by vertical-scanning interferometry (VSI). The large spectral bandwidth of a white-light source produces a short coherence length, therefore good contrast fringes are obtained only when the two path lengths of the interferometer are closely matched in length. The interference irradiance distribution along the vertical scanning direction is attenuated by the coherence envelope, the peak of which is located near the best-focus position. VSI techniques map the surface profile by locating the peak position of the coherence envelope. The main research interests have been improving lateral resolution and height resolution both theoretically and experimentally. As the height resolution improves, unexpected false information starts to appear in height profiles of objects with sharp discontinuities less than the coherence length of the light source in use. Because of the shape of the false information, the artifact is called "bat wings". This will be further explained in the later chapters. Some "bat wings" samples are shown in Fig. 1 - Fig. 3. There have been many attempts at understanding and removing these bat wings so that the surface structure close to an edge discontinuity can be measured. To our knowledge, no solution has been proposed except the use of a low pass filter or median filter to simply cut off the wings at the expense of losing the information close to the edge structures.

This dissertation discusses a diffraction model that is able to explain the physical mechanism of the bat wings artifact. And, based on the results of the analysis of bat wings, an improved vertical-scanning algorithm is proposed, which not only greatly improves the height resolution but also removes the bat-wings artifact.

The bat-wings artifact appears at sharp discontinuities that are less than the coherence length of the light source of the interferometric microscope. Fig. 1 - Fig. 3 show the artifact in a few optical elements measured by an interference microscope (Veeco, NT-2000) and displayed by WYKO Vision32 software. The artifact may look like Gibbs phenomenon, but they are surface profiles retrieved from interference correlograms, not the irradiance at each position. Therefore it is a totally different phenomenon from the Gibbs phenomenon, which is caused by the loss of high spatial frequencies by going through a lens.

It is clear that the bat wings hide the surface information close to the discontinuities and also prevent the precise step height measurement, which is critical in some samples such as magnetic reading heads and phase masks. The questions rising here are

1. What causes these bat wings?

2. Can we fix it? and how?

The answer to both questions will be clarified and solved in this dissertation.

The above two issues can be rephrased as understanding and solving the bat wings problem. Chapters 1 through 5 are dedicated to understanding the physics of the phenomenon. Chapter 6 provides a solution to the bat wings problem and develops a new algorithm which can reveal the surface structures close to the edges. It will be clear that the new algorithm results from a full understanding of the mechanism of the
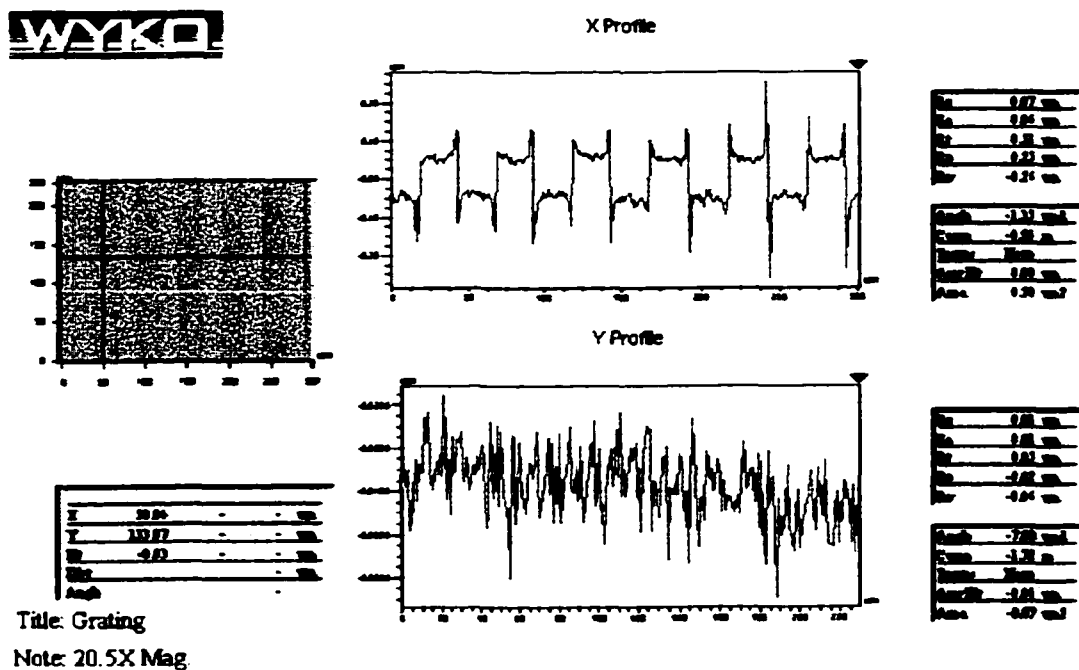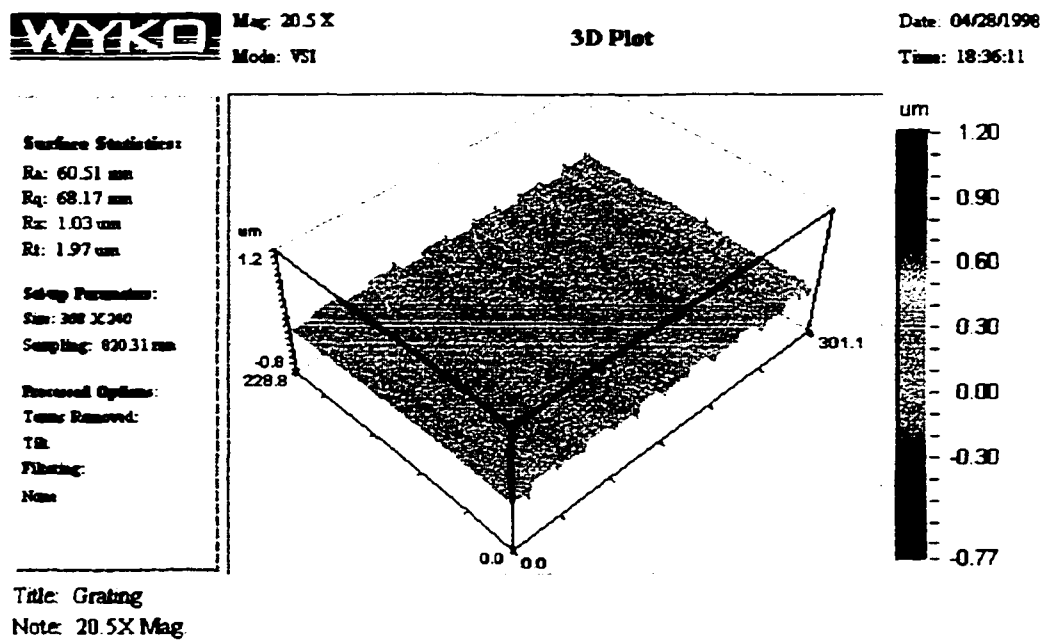
Figure 1: **The 3-dimensional surface profile of an 88 nm grating and its cross profiles.**
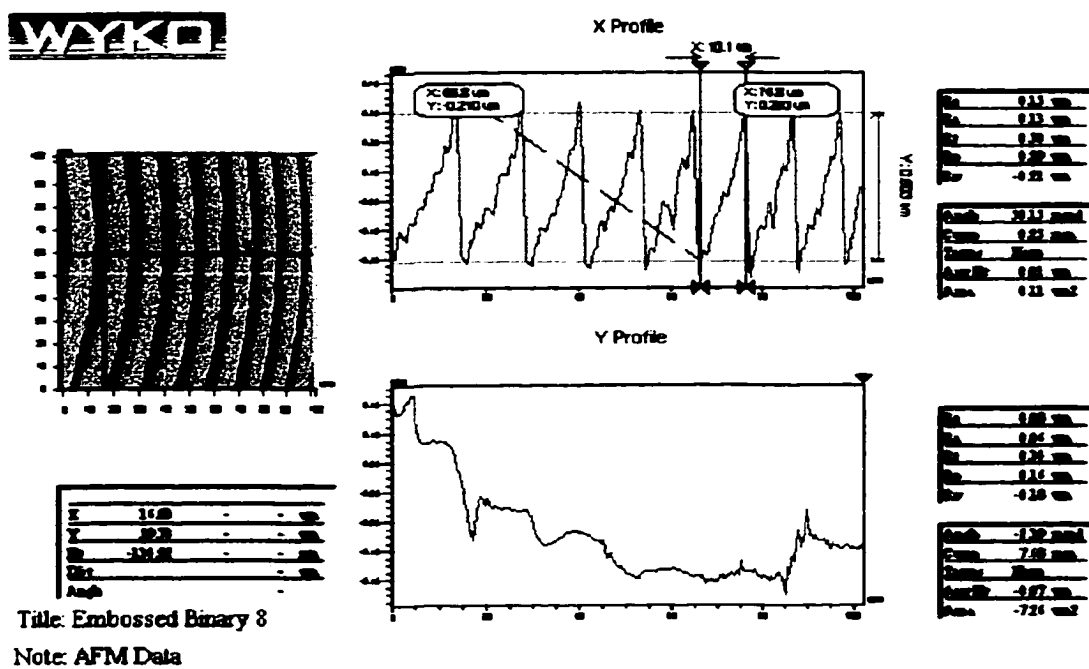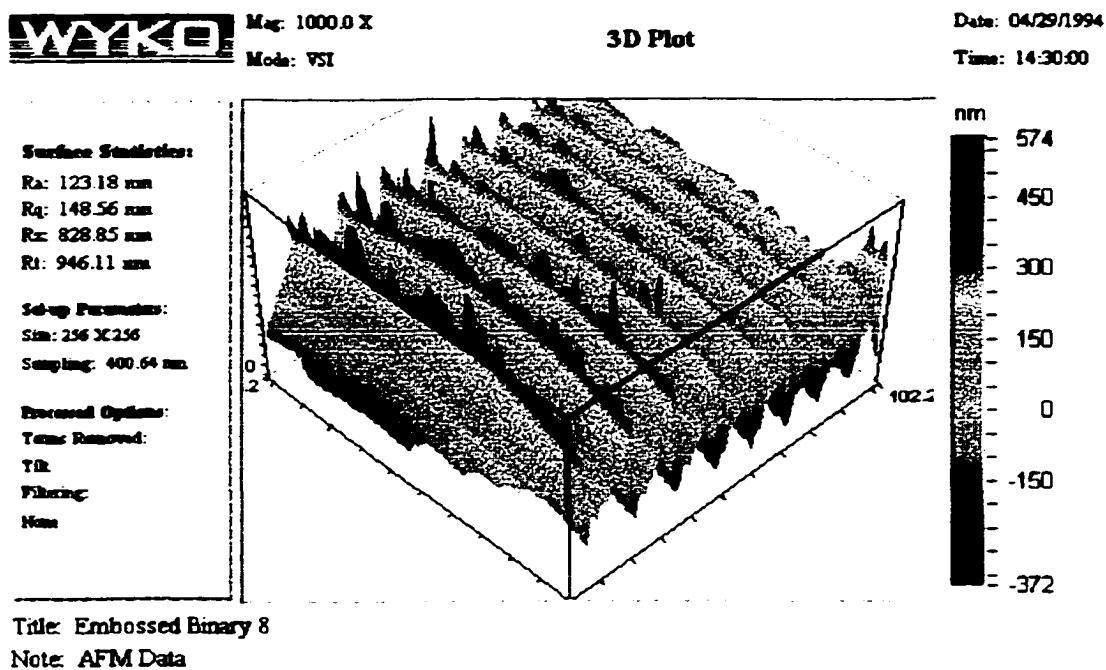
Figure 2: **The 3-dimensional surface profile of a Kino form Fresnel lens and its cross profiles.**
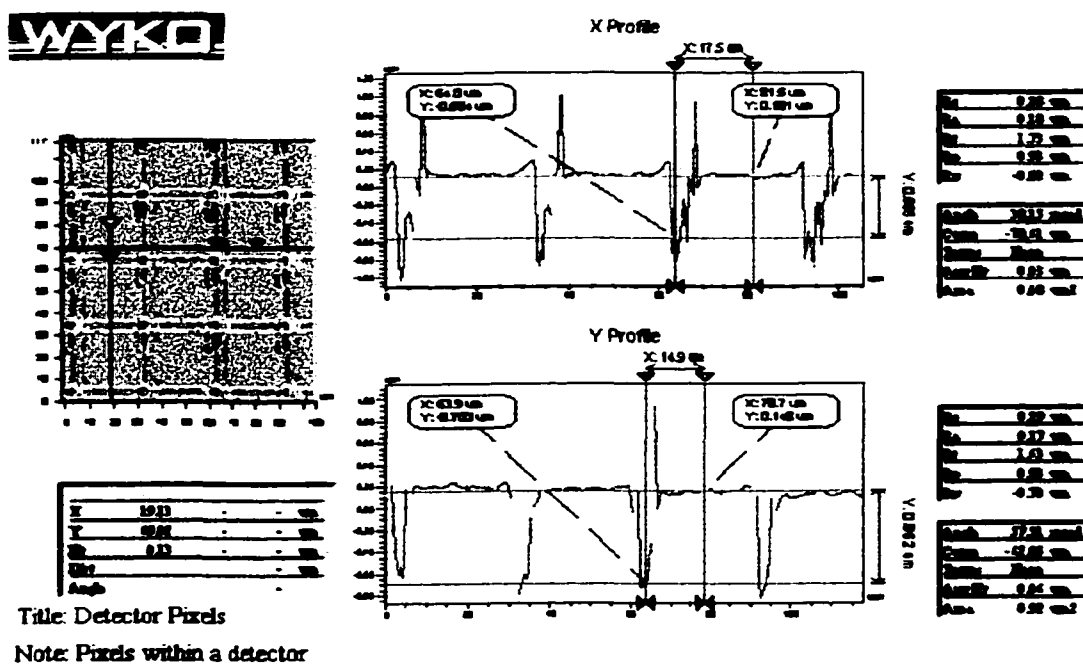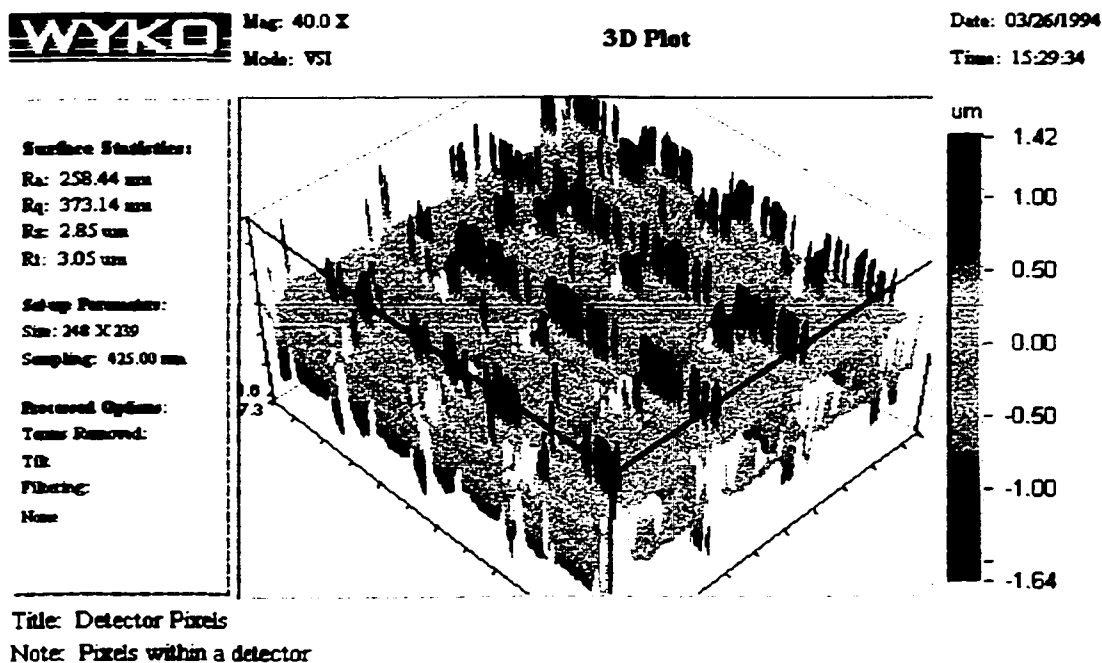
Figure 3: **The 3-dimensional surface profile of a CCD and its cross profiles.**

bat-wings effect. We propose to solve this problem by combining vertical scanning interferometry (VSI) and phase-shifting interferometry (PSI). Since the fractional phase is measured at the scanning position close to the coherence envelope peak during vertical scan, the method is called PSI on the Fly.

The ultimate goal is to show that the PSI on the Fly algorithm indeed resolves the bat wings problem. In order to achieve our goal, Chapter 1 reviews the interference microscope and Chapter 2 discusses various established vertical scanning algorithms. Chapter 2 includes the error analysis of the Hariharan's five step phase-shifting error compensation algorithm that is adopted in the PSI on the Fly technique discussed in Chapter 6. There is an independent chapter on the phase change upon reflection, because in many cases the substrate materials are different on each side of the discontinuity, which in turn affects the step-height measurement as discussed in Chapter 3. The detailed analysis on bat wings is given in Chapter 5 to show the theoretical basis for development of the PSI of the Fly algorithm.

Chapter 1

WHITE-LIGHT INTERFERENCE MICROSCOPE

In this chapter the imaging theory for white-light interference microscopes, given by Kino and Chim in reference [34], is reviewed. The range resolution (height resolution) for a perfect plane reflector is derived for a broadband light source and finite numerical aperture.

1.1   Introduction

White-light interferometry (WLI) employs a broadband light source for illumination since it has the following advantages[64] over laser illumination:

1. no spurious fringes

2. can measure large steps - multiple wavelength operation

3. easy to determine focus

There are many applications for WLI. It has largely been used with interference microscopes to look at small structures which have too much depth or are too rough.

They are unable to be measured with standard phase-measurement interferometry (PMI) methods in which the optical path is only changed by about a wavelength.

Three interference-objective configurations are most commonly used: Michelson, Mirau and Linnik. These are shown in Fig. 1.1-Fig. 1.3. Their advantages and disadvantages can be summarized as follows:

- Mirau Interference Objectives

  - Medium magnification

  - Central obscuration

  - Limited numerical aperture

- Michelson Interference Objectives

  - Low magnification, large field-of-view

  - Beamsplitter limits working distance

  - No central obscuration

- Linnik Interference Objectives

  - Large numerical aperture, large magnification

  - Beamsplitter does not limit working distance

  - Expensive, matched objectives required

The lateral resolution and range resolution for interference microscopes, which indicate the system performance, are not as familiar as those for regular microscopes[8]. The three dimensional imaging theory for interference microscopes was derived by Kino and Chim[34]. Their original results were obtained from scalar theory. They
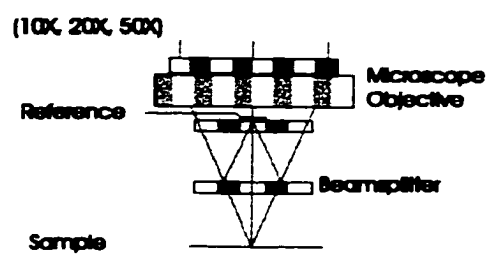
Figure 1.1: **Mirau interference microscope objective.**
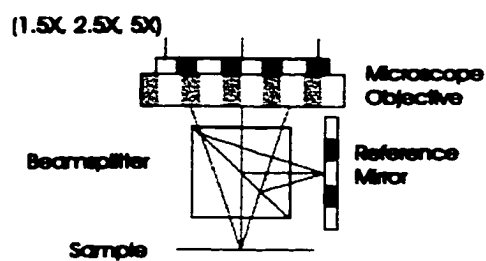
Figure 1.2: **Michelson interference microscope objective.**
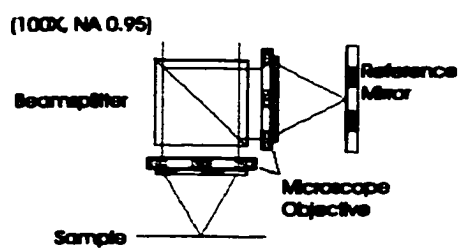
Figure 1.3: **Linnik interference microscope objective.**

recently updated their results in terms of Richards and Wolf's vector theory[13, 53] and showed that the vector results are identical in depth response and nearly identical in transverse definition to those obtained from scalar theory. Therefore we will not describe the vector theory here. The rest of this chapter is based on their first paper.

1.2 Response of a interference microscope to a planar reflector

The lateral and range resolutions can be derived from the response of the interference microscope to a planar reflector at a distance z from the focus. The Fourier transform of the incident light field $u(x, y)$ is

$$U(k_x, k_y) = \int \int_{-\infty}^{\infty} u(x, y) e^{i(k_x x + k_y y)} dx dy. \tag{1.2.1}$$

The reflected wave component $U_S(k_x, k_y)$ from the sample surface with spatial frequencies $(k_x/2\pi, k_y/2\pi)$ can be written as

$$U_S(k_x, k_y) = BU(-k_x, -k_y) e^{-i(2k_z z + \phi)}, \tag{1.2.2}$$

where ϕ is the phase change on reflection from the sample and reference combined, and $\vec{k} = (k_x, k_y, k_z)$ is the wave vector. The wave vector can be expressed by wavelength as $k = |\vec{k}| = \sqrt{k_x^2 + k_y^2 + k_z^2} = \frac{2\pi}{\lambda}$. The reference wave component $U_R(k_x, k_y)$ from the reference mirror at the reference focal plane $z = z_0$ is

$$U_R(k_x, k_y) = AU(-k_x, -k_y) e^{-i2k_z z_0} \tag{1.2.3}$$

where A and B are the reflectivities from the planar object and reference mirror, respectively. Switching to cylindrical coordinates as shown in Fig. 1.4 would make
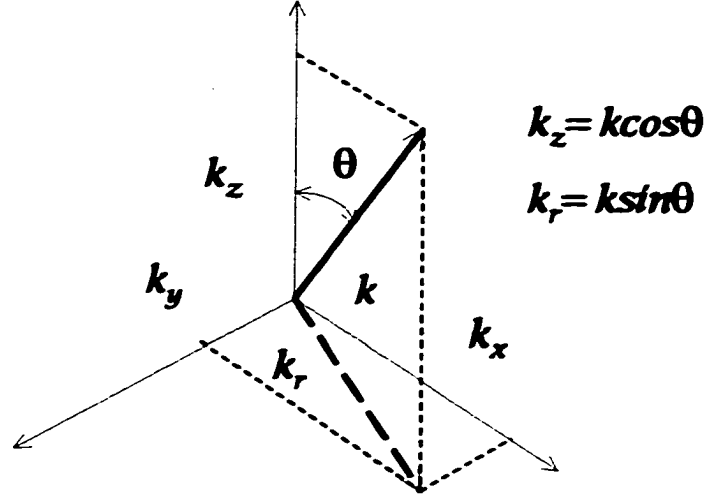
Figure 1.4: **The coordinate of wave vector** $\vec{k}$.

further analysis simpler since the system has rotational symmetry.

The numerical aperture of the objective is $N.A. = \sin\theta_0$, so that $|U(k_x, k_y)|$ is constant for $\theta \leq \theta_0$ and zero for $\theta > \theta_0$, i.e. uniform angular illumination. Then the output current from the detector is of the form,

$$i(z) = \int |U_R + U_S|^2\, 2\pi k_r dk_r \qquad (1.2.4)$$

$$= 4\pi k^2 |U|^2 \int_0^\pi \{A^2 + B^2 + 2AB\cos[2k(z - z_0)\cos\theta + \phi]\}$$

$$\times rect\left(\frac{\theta - \theta_0/2}{\theta_0}\right) \sin\theta\cos\theta d\theta.$$

Only the modulation part in Eq. (1.2.4), which is the third term and also referred as the correlation term, carries the surface height information either through the modulation envelope peak position or the phase of the fringes. Therefore, analysis of this term is enough for further treatment.

When the light source has a finite bandwidth with an intensity variation $F(\lambda)$, the correlation term is given by

$$I_{AB}^w(z) = 8\pi AB|U|^2 \int_{bandwidth} \int_0^\pi k^2 \{\cos[2k(z-z_0)\cos\theta + \phi] \qquad (1.2.5)$$
$$\times rect\left(\frac{\theta - \theta_0/2}{\theta_0}\right) \sin\theta\cos\theta d\theta\} F(\lambda)d\lambda$$

where the superscript w stands for white-light source.

1.3 Range resolution

The range resolution derived from Eq. (1.2.5) is discussed for three cases:

1. point source

2. monochromatic extended source

3. general case.

1.3.1 Point source

When the light source is a point source, the rectangular function in Eq. 1.2.5 reduces to a delta function. It can be shown by variable replacement of $\cos\theta = t$ and requiring $t \to 1$:

$$-\sin\theta d\theta = dt$$
$$rect\left(\frac{\theta - \theta_0/2}{\theta_0}\right) = \delta(t-1).$$

Then the integral over the numerical aperture can be carried out:

$$\Gamma^w_{AB}(z) = -8\pi AB|U|^2 \int_{bandwidth} \cos[2k(z - z_0) + \phi]F(\lambda)k^2 d\lambda \qquad (1.3.1)$$

$$= -8\pi AB|U|^2 Re\left[\int_{bandwidth} \exp\{-i[2k(z - z_0) + \phi]\}F(\lambda)k^2 d\lambda\right]$$

$$= -8\pi AB|U|^2 Re\left[e^{-i\phi}\int_{bandwidth} e^{-i2k(z-z_0)}F(\lambda)k^2 d\lambda\right].$$

Notice that $k^2 d\lambda = -2\pi dk$ and rewrite $F(\lambda)$ as $\hat{F}(k)$, the equation is simplified to

$$\Gamma^w_{AB}(z) = 16\pi^2 AB|U|^2 Re\left[e^{-i\phi}\int_{bandwidth} e^{-i2k(z-z_0)}\hat{F}(k)dk\right] \qquad (1.3.2)$$

$$= 16\pi^2 AB|U|^2 Re\left[e^{-i\phi}F.T.\left[\hat{F}(k)\right]\Big|_{\xi=\frac{2(z-z_0)}{2\pi}}\right].$$

When the source has a flat distribution in the wavenumber range of $[k_1, k_2]$, the
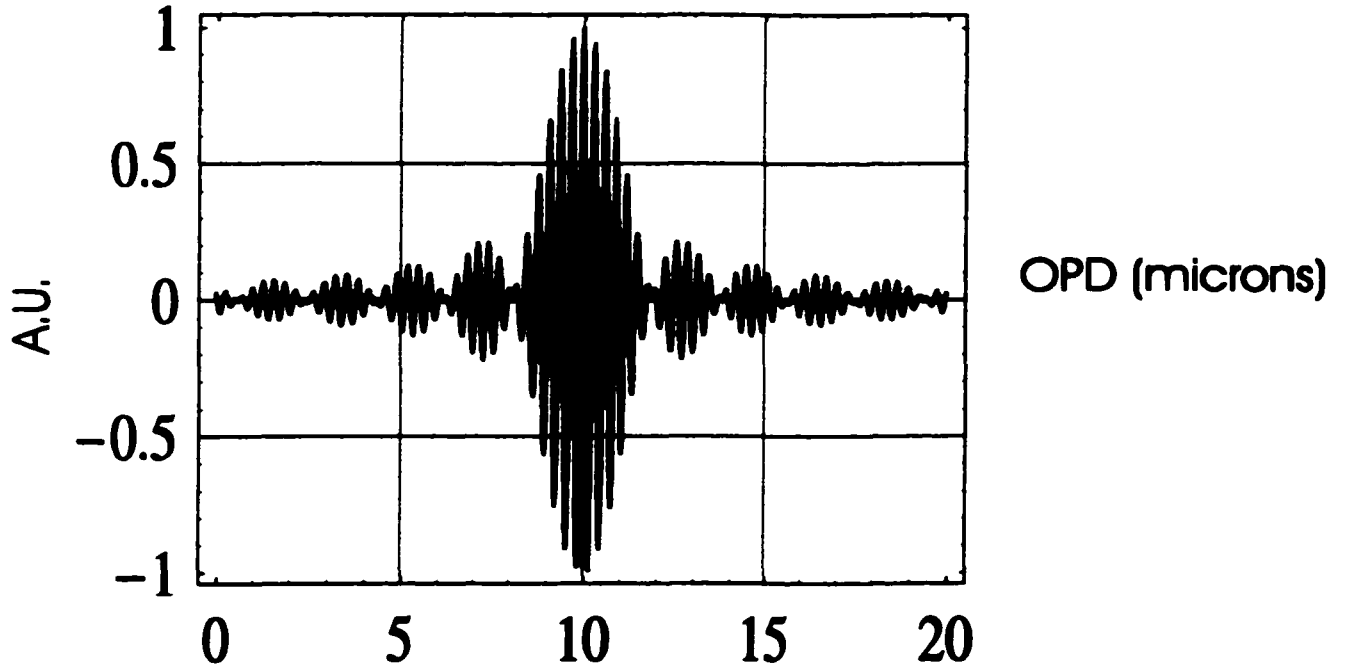
Figure 1.5: **White-light fringes.**

center wavenumber is $\bar{k} = \frac{k_1 + k_2}{2}$ and bandwidth is $\Delta k = k_2 - k_1$. The temporal

source distribution is expressed as

$$\hat{F}(k) = rect\left(\frac{k - \bar{k}}{\Delta k}\right). \tag{1.3.3}$$

The Fourier transform of the source distribution is

$$F.T.\left[\hat{F}(k)\right] = e^{i2\pi \bar{k}\xi} \Delta k \, sinc(\Delta k\xi). \tag{1.3.4}$$

$\Gamma_{AB}^{w}(z)$ arrives at a sinusoidal variation modified by a *sinc* function envelope which has a maximum at $z = z_0$ and falls off with $|z - z_0|$. The modulation part of fringes is given by

$$\Gamma_{AB}^{w} \propto \cos\left[\frac{2\pi}{\lambda}2(z - z_0)\right] sinc\left[\frac{2(z - z_0)}{\lambda^2/\Delta\lambda}\right] \tag{1.3.5}$$

and is displayed in Fig. 1.5.

A Gaussian function with Δk being the full width at the half maximum (FWHM) is another typical light source representation. According to the Fourier theory Eq. 1.3.2 results in a Gaussian envelope with the FWHM of $\Delta z = 2\pi/\Delta k = \bar{\lambda}^2/\Delta\lambda$ in this case.

1.3.2   Monochromatic extended source

Monochromatic extended source is the other simple case, that is, $F(\lambda) = \delta(\lambda_0)$. Eq. 1.2.5 reduces to

$$\begin{aligned}
I_{AB}(z) &= 8\pi \left(\frac{2\pi}{\lambda_0}\right)^2 AB|U|^2 \int_0^{\theta_0} \cos[\frac{4\pi}{\lambda_0}(z - z_0)\cos\theta + \phi] \tag{1.3.6}\\
&\quad \times \sin\theta\cos\theta d\theta\\
&= 8\pi \left(\frac{2\pi}{\lambda_0}\right)^2 AB|U|^2 Re\left[e^{-i\phi} \int_0^{\theta_0} e^{-i\frac{4\pi}{\lambda_0}(z-z_0)\cos\theta} \sin\theta\cos\theta d\theta\right].
\end{aligned}$$

This formula is identical to that for the amplitude variation with the distance z of the confocal microscope[58]. For a narrowband system, the variation of the output signal

from the detector (which is proportional to irradiance) is identical to the amplitude variation with distance z of the wave passing through the pinhole of a confocal scanning optical microscope[16, 33, 59]. Following the analysis given in these references and using the paraxial assumption $\cos\theta \simeq 1$ to eliminate the obliquity factor, the integral in Eq. 1.3.6 can be easily carried out:

$$
\begin{aligned}
I_{AB}(z) &= 8\pi \left(\frac{2\pi}{\lambda_0}\right)^2 AB|U|^2 \pi \left(1 - \cos\theta_0\right) \cos\left[\frac{2\pi}{\lambda_0}(z - z_0)(1 + \cos\theta_0) + \phi\right] \\
&\quad \times sinc\left[\frac{2}{\lambda_0}(z - z_0)(1 - \cos\theta_0)\right]
\end{aligned}
\tag{1.3.7}
$$

where $sinc(x) = \frac{\sin\pi x}{\pi x}$. The signal output can be normalized at $z = z_0$ then

$$
I_{AB}^{normalize}(z) = \cos\left[\frac{2\pi}{\lambda_0}2(z - z_0)\cos^2\theta_0 + \phi\right] sinc\left[\frac{2}{\lambda_0}2(z - z_0)\sin^2\theta_0\right].
\tag{1.3.8}
$$

Eq. 1.3.8 appears as a carrier with a wavelength of $\frac{\lambda_0/2}{\cos^2\theta_0}$, modulated by a $sinc$ function. The modulation is caused by the superposition of a flat wavelength distribution of width $\Delta k = \frac{2\pi}{\lambda_0}2\sin^2\theta_0$. Also the numerical aperture changes the effective carrier frequency (fringe spacing) and therefore the surface height measured with that objective. This effect is called numerical aperture effect[11, 17]. If we define the range resolution, d_z, as the distance of half the maximum value of $\left[I_{AB}^{normalize}(z)\right]^2$ for monochromatic illumination, then

$$
d_z = \frac{0.45\lambda_0}{1 - \cos\theta}
\tag{1.3.9}
$$

1.3.3 General case

The range resolution for the general case of finite aperture and polychromatic illumination is treated in this section. Eq.(1.2.5) is the starting point, first assuming the paraxial approximation and performing the integral over the numerical aperture

as done in Eq.(1.3.6):

$$\Gamma^w_{AB}(z) = 8\pi AB|U|^2\pi(1-\cos\theta_0)\int_{bandwidth} k^2\cos\left[k(z-z_0)(1+\cos\theta_0)+\phi\right]$$

$$\times sinc\left[k(z-z_0)(1-\cos\theta_0)\right]F(\lambda)d\lambda$$

$$= 8\pi AB|U|^2\pi(1-\cos\theta_0)\int_{-\frac{\Delta k}{2}}^{\frac{\Delta k}{2}}\cos\left[(k_0-\delta k)(z-z_0)(1+\cos\theta_0)+\phi\right]$$

$$\times sinc\left[(k_0-\delta k)(z-z_0)(1-\cos\theta_0)\right]d\delta k. \tag{1.3.10}$$

For simplicity, A flat broad-band source centered at a frequency corresponding to $k_0 = \frac{2\pi}{\lambda_0}$ and with a wavenumber bandwidth Δk is assumed. Since the $sinc$ function in Eq. 1.3.10 localizes at the center wavenumber k_0 the variable k can be substituted with k_0. Take the $sinc$ function out of the integral, then

$$\Gamma^w_{AB}(z) = 8\pi AB|U|^2\pi(1-\cos\theta_0)\,sinc\left[k_0(z-z_0)(1-\cos\theta_0)\right] \tag{1.3.11}$$

$$\times \int_{-\frac{\Delta k}{2}}^{\frac{\Delta k}{2}}\cos\left[(k_0-\delta k)(z-z_0)(1+\cos\theta_0)+\phi\right]d\delta k$$

$$= 8\pi AB|U|^2\pi(1-\cos\theta_0)\,sinc\left[k_0(z-z_0)(1-\cos\theta_0)\right]$$

$$\times Re\left[e^{-i[k_0(z-z_0)(1+\cos\theta_0)+\phi]}\int_{-\frac{\Delta k}{2}}^{\frac{\Delta k}{2}}e^{i\delta k(z-z_0)(1+\cos\theta_0)}d\delta k\right]$$

$$= 8\pi AB|U|^2\pi(1-\cos\theta_0)\,sinc\left[k_0(z-z_0)(1-\cos\theta_0)\right]$$

$$\times Re\left[e^{-i[k_0(z-z_0)(1+\cos\theta_0)+\phi]}F.T.\left[rect\left(\frac{\delta k}{\Delta k}\right)\right]\Big|_{\xi=\frac{(z-z_0)(1+\cos\theta_0)}{2\pi}}\right]$$

$$= 8\pi AB|U|^2\pi(1-\cos\theta_0)\,sinc\left[k_0(z-z_0)(1-\cos\theta_0)\right]$$

$$\times Re\left[e^{-i[k_0(z-z_0)(1+\cos\theta_0)+\phi]}\Delta k\,sinc\left[\Delta k\frac{(z-z_0)(1+\cos\theta_0)}{2\pi}\right]\right].$$

Next normalizing the signal output to its irradiance at $z=z_0$, the final expression is

$$\Gamma^{w,normalize}_{AB}(z) = \cos\left[k_0(z-z_0)(1+\cos\theta_0)+\phi\right] \tag{1.3.12}$$

$$\times sinc\left[k_0(z-z_0)(1-\cos\theta_0)\right]sinc\left[\Delta k\frac{(z-z_0)(1+\cos\theta_0)}{2\pi}\right].$$

There are two envelope functions modifying the fringes. One comes from the aperture effect with the coherence length of $l^{N.A.}_c = \frac{\lambda_0}{1-\cos\theta_0}$. The other results from both the

aperture effect and the broadband light source with the coherence length of $l_c^w =$ $\frac{\lambda_0^2}{\Delta\lambda}\frac{1}{1+\cos\theta_0}$, where $\Delta\lambda = \frac{2\pi}{k_0^2}\Delta k$. The coherence envelope with the shortest coherence length forms the observable envelope for the fringes in z direction. Therefore to have good range resolution we could either use large aperture objectives or introduce a broadband light source.

For instance, the second *sinc* function in Eq.(1.3.12) is the dominant factor when using a broadband light source. The range resolution between half power points, as defined in previous sections, would be limited by the bandwidth. And

$$d_z = 0.89\frac{\lambda_0^2}{\Delta\lambda}\frac{1}{1 + \cos\theta_0} \qquad (1.3.13)$$

is the expression for the range resolution.

More generally with finite bandwidth and a finite aperture, the range resolution is smaller than its value due to either effect alone. The decrease of range resolution can be explained as a product of two *sinc* functions with comparable width or based on spatial frequency response in the z direction[45]. A second explanation is simpler and more insightful. Let's assume the maximum range of spatial frequency available is due to the numerical aperture of the objective and the bandwidth of the light source. When a single frequency ray at the maximum angle θ_0 to the axis is reflected from a planar substrate, the total change in wavenumber is $\delta k_z = 2k_0\cos\theta_0$. On the other hand, the on-axis ray has the change of $\delta k_z = 2k_0$. Therefore the maximum range of spatial frequency extent is $\Delta k_z = 2k_0(1 - \cos\theta_0)$. This frequency extent causes the *sinc* function in Eq. (1.3.8). If, in addition, the illumination bandwidth corresponds to a range of wavenumbers Δk, the range of spatial frequency in z direction is increased by $\delta k_z = 2\Delta k$. The total frequency extent in the z direction is the sum of the two effects, i.e. the frequency extent at the lowest frequency k_1 plus the source

bandwidth

$$\Delta k_z \simeq 2k_1(1 - \cos\theta_0) + 2\Delta k$$

$$= 2k_0(1 - \cos\theta_0) + \Delta k(1 + \cos\theta_0). \qquad (1.3.14)$$

k_0 here is the center wavenumber.

1.4 Lateral resolution

The lateral resolution can be found by standard imaging theory; a good reference is the paper by Davidson[39]. At the image plane (x_i, y_i), the reference $(u_R(x_i, y_i))$ and test wave $(u_S(x_i, y_i))$ can be written as

$$u_R(x_i, y_i) = \int h(x_i - x_0, y_i - y_0)u_R(x_0, y_0)dx_0 dy_0 \qquad (1.4.1)$$

$$u_S(x_i, y_i) = \int h(x_i - x, y_i - y)u_S(x, y)dx dy \qquad (1.4.2)$$

and

$$u_R(x_0, y_0) = A(x_0, y_0)e^{i\phi_R(x_0, y_0)} \qquad (1.4.3)$$

$$u_S(x, y) = B(x, y)e^{i\phi_S(x, y)}, \qquad (1.4.4)$$

where x_0 and x are the reference and test wave coordinates, respectively. $h(x, y)$ is the coherent point spread function[25]. The signal detected by CCD camera is

$$I(x_i, y_i) = |< u_R(x_i, y_i) + u_S(x_i, y_i) >|^2 \qquad (1.4.5)$$

$$= |u_R(x_i, y_i)|^2 + |u_S(x_i, y_i)|^2 + 2Re[u_R(x_i, y_i)^* u_S(x_i, y_i)],$$

where $< \quad >$ denotes assemble average. Again we are only interested in the cross product

$$I_{AB}(x_i, y_i) = \int \int h(x_i - x_0, y_i - y_0)^* h(x_i - x_0, y_i - y_0) \qquad (1.4.6)$$

$$\times 2Re[< u_R(x_i, y_i)^* u_S(x_i, y_i) >]dx_0 dy_0 dx dy.$$

For a spatially incoherent source, $< u_R(x_i, y_i)^* u_S(x_i, y_i) >$ is zero, unless (x_0, y_0) and (x, y) are identical, such that $< u_R(x_i, y_i)^* u_S(x_i, y_i) > \propto \delta(x_0 - x, y_0 - y)$. Eq. (1.4.6) is simplified to

$$I_{AB}(x_i, y_i) = \int 2AB \cos \left[\phi_R(x, y) - \phi_S(x, y) \right] |h(x_i - x, y_i - y)|^2 dx dy. \qquad (1.4.7)$$

The point spread function dominating the interference microscope is the same $|h(x, y)|^2$ as for the regular microscope. For a cylindrically symmetric paraxial system, the normalized value of $h(r)$ is given by a *somb* function[9, 24],

$$\begin{aligned} h(r) &= somb \left(\frac{r}{\lambda \sin \theta_0} \right) \qquad (1.4.8) \\ &= \frac{2J_1 \left(\frac{r}{\lambda \sin \theta_0} \right)}{\frac{r}{\lambda \sin \theta_0}}, \end{aligned}$$

and here $r = \sqrt{x^2 + y^2}$. The lateral resolution can be expressed as half the Airy disk diameter or $1.22 \frac{\lambda}{N.A.}$ according to Rayleigh's criterion[9].

Chapter 2

COHERENCE-PEAK-SENSING ALGORITHMS

In this chapter, the algorithms[5, 15, 19, 22, 23, 34, 35, 52, 54] for extracting 3-dimensional information from low coherence inference fringes is reviewed. Each algorithm tries to obtain an accurate representation of the surface topography with a minimum of calculations. The basis of the coherent-peak-sensing is somehow to locate the peak position of the coherence envelope of the white light fringes. This can be done either in the spatial or the frequency domain. The important requirements for a good algorithm are

1. speed

2. requires minimal amount of data

3. accurate

4. immune to noise

5. adaptable to different sample spacings

6. easy to implement

7. reliable and repeatable

2.1 Introduction

The light irradiance recorded by the camera in a white light interferometer that is spatially incoherent has the form

$$i(x, y, z) = i_{avg}(x, y) + c(x, y)\gamma\left[z - h(x, y)\right]\cos\left[\frac{2\pi}{\lambda}2z - \alpha(x, y)\right], \qquad (2.1.1)$$

where the coordinates x and y refer to the pixel locations in the camera, and z corresponds to the height scan position of the object. $I_{avg}(x, y)$ is a constant off-set corresponding to the DC irradiance value. $c(x, y)$ is determined by the relative reflectances of the object and reference surface. $\gamma(x, y, z)$ is the interference fringe envelope function which we want to extract from the fringes to determine the height map $h(x, y)$ on the object surface. $\bar{\lambda}$ is the center wavelength of the white light source. $\alpha(x, y)$ is a function of the phase change upon reflection at the object surface. Although there is no wavelength dependency explicitly in Eq. (2.1.1), the envelope location has dependencies on the phase dispersion upon reflection. We will treat this effect in Chapter 3. The peak of $\gamma(x, y, z)$ occurs when the optical path difference (OPD) is zero in this expression. The sample surface can be profiled by finding zero OPD positions over entire xy plane.

We can categorize the signal demodulation techniques into two major groups, recovering the envelope function from the discrete white light fringes or using the fringe maximums for height evaluation. The former group contains two totally different mathematical methods to do the envelope function extracting: white light interferometry algorithms[23, 35] and Fourier-Hilbert transform algorithms[15, 34]. The latter contain the primitive method of locating the largest intensity position which may limit the height resolution to the sampling step (If the measurement time is not a limiting factor, this brute-force type surface profiler does exist[10].), simple Gaussian

envelope fitting[52, 54] and a very sophisticated method based on the shift theorem of the Fourier transform[19, 22]. There is another patented fast algorithm[5] by Veeco Corporation (formerly WYKO Corporation), which falls into neither category but is worth mentioning in coming sections. In this chapter these established algorithms are described in great detail and their performances are compared, especially on the bat wings effect.

2.2 Fourier transform algorithm

The Fourier transform analysis of white light interference fringes is briefly discussed in this section. The Fourier transform, on z, of Eq. (2.1.1) is

$$I(x,y,k) = I_{avg}(x,y)\delta(k) + \frac{C(x,y)}{2}\Gamma(k)e^{-2\pi ikh(x,y)} * \left[e^{i\alpha}\delta(k-k_0) + e^{-i\alpha}\delta(k+k_0)\right],$$

$$(2.2.1)$$

where $*$ denotes a 1-dimensional convolution, k denotes spatial frequency in the z direction and $k_0 = \frac{2}{\lambda}$ is the carrier frequency for the above reflection scheme. $\Gamma(k)$ is the Fourier transform of $\gamma(z)$. Eq. (2.2.1) contains three terms: a constant at zero frequency and two sidebands centered at $\pm k_0$. One of the sidebands needs to be filtered to recover the envelope function $\gamma(x,y,z)$. These three terms have to be well separated for perfect recovery. After the filtering, the sidelobe is shifted to the center to lower the spatial frequencies as much as possible, as shown in Fig. 2.1. During the filtering process we have to keep the phase which gives the position shift[24] in real space. The inverse Fourier transformed spectrum is

$$I.F.T\left[\frac{C(x,y)}{2}\Gamma(k)e^{i[-2\pi kh(x,y)+\alpha]}\right] = \frac{c(x,y)}{2}\gamma(z)e^{i\alpha} * \delta[z-h(x,y)]$$

$$= \frac{c(x,y)}{2}\gamma(z-h(x,y))e^{i\alpha}. \qquad (2.2.2)$$
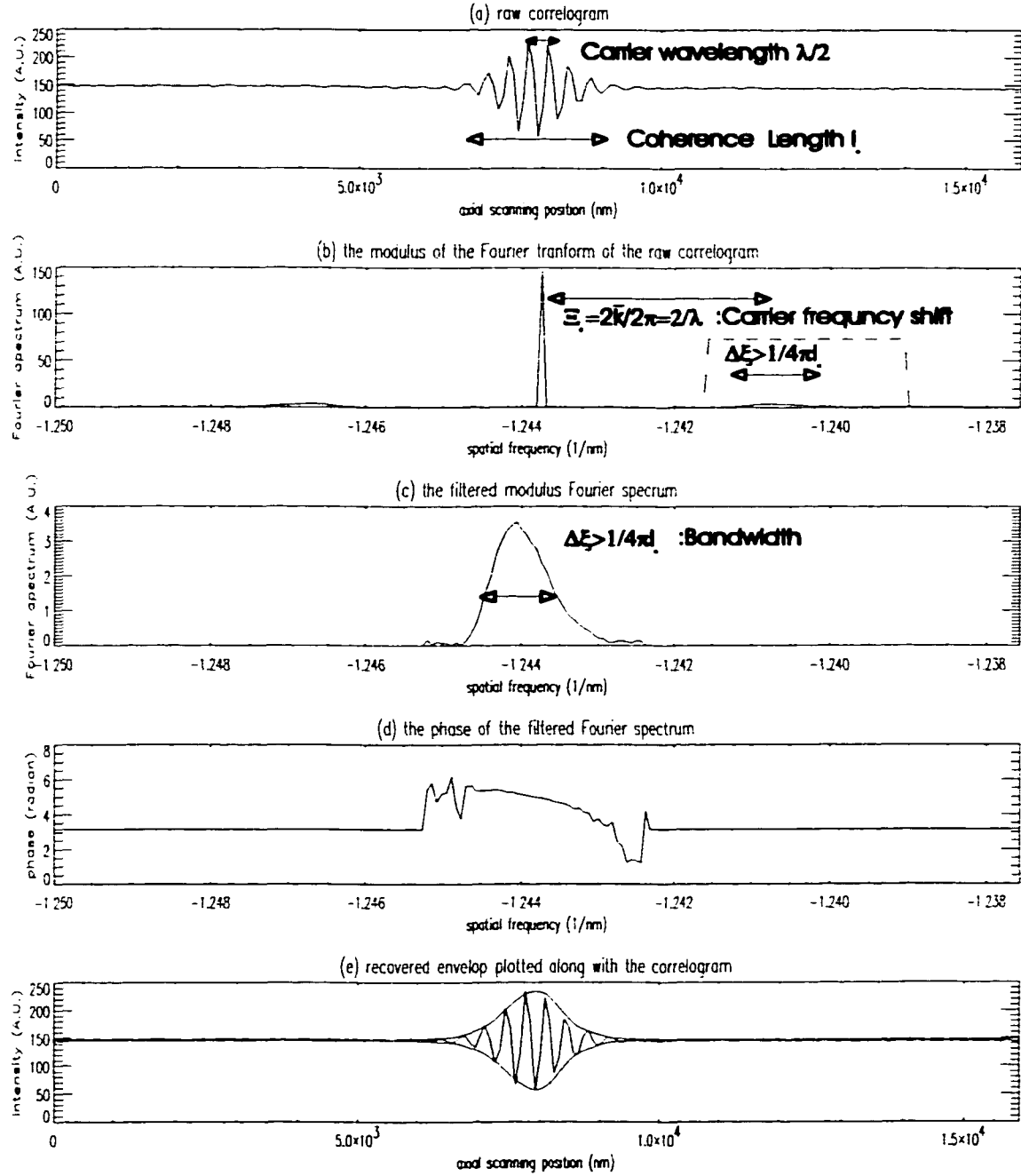
Figure 2.1: **Fourier transform analysis of a correlogram. (a) The raw correlogram obtained through vertical scanning. (b) The modulus of the Fourier transform of the correlogram, i.e.** $|I(x, y, k)|$**. (c) The filtered modulus of the Fourier spectrum as indicated in part (b). (d) The phase of the Fourier spectrum as indicated in part (b). (e) Recovered coherence envelope function by taking the modulus of the inverse Fourier transform of the filtered Fourier spectrum.**

The modulus of Eq. (2.2.2) gives us the coherence function, i.e. $\gamma[z - h(x, y)] \propto |I.F.T.[filtered \; spectrum]|$. This method is the basis of the technique used by Kino[34].

The requirement for using this method is that the Fourier transformed spectrum $\Gamma(k)$ should be well band-limited. Otherwise the sidebands overlap with the center lobe and the filtering process can not pick out only one of the sidelobes. As a result, aliasing occurs. This requirement is contradictory to the range resolution requirement we discussed in Chapter 1. High range resolution requires a small coherence length, $l_c = \frac{\lambda^2}{\Delta\lambda}$, which means $\gamma(z)$ has a narrow width. Thus the Fourier transform $\Gamma(k)$ has a wide spread in the Fourier domain, which implies a relationship between the coherence length and mean carrier wavelength λ. From Fig. 2.1 the relationship,

$$\Delta k \leq 2\bar{k}, \qquad (2.2.3)$$

is easily found, where Δk is the bandwidth of $\Gamma(k)$. Using the uncertainty principle, it can be expressed as

$$\Delta k \geq \frac{1}{2l_c} \qquad (2.2.4)$$

and $\bar{k} = \frac{2\pi}{\lambda}$ is the mean carrier frequency. A Gaussian coherence envelope has the smallest uncertainty which is well known, for this case Eq. (2.2.3) can be written as

$$\bar{\lambda} \geq \frac{\Delta\lambda}{8\pi}. \qquad (2.2.5)$$

For most of the cases, the center or mean carrier wavelength is larger than the wavelength distribution of the light source. For example, Fig. 2.2 and Fig. 2.3 show the response of the CCD camera (Chou) and light distributions of a nominal tungsten light bulb which is preferred as a light source for white light interferometry. The condition of Eq. (2.2.5) is easy to meet. Actually, there are other conditions that
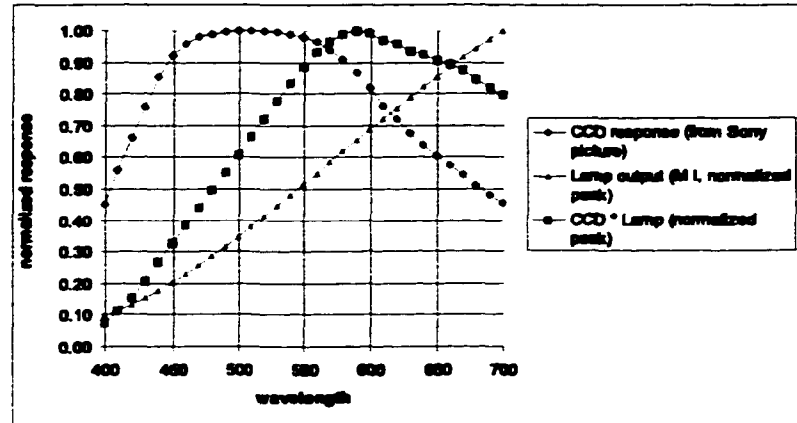
Figure 2.2: **A CCD camera response and a light bulb wavelength distribution.**
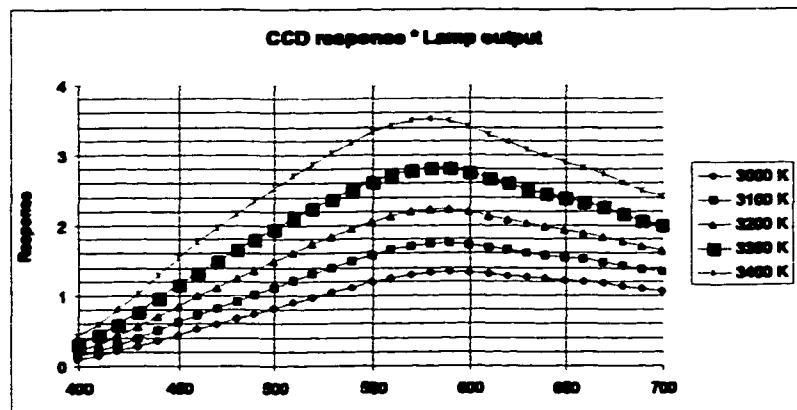
Figure 2.3: **The total response of a CCD camera and a tungsten light bulb as a function of tungsten temperature.**

we must carefully discuss: the sampling distance and the bandwidth of $\Gamma(k)$. The sampling distance Δ in the scanning direction limits the highest spatial frequency we can have in the Fourier space:

$$\xi_{max} = \frac{1}{\Delta}. \qquad (2.2.6)$$

The requirement is

$$2\bar{k} + \Delta k \leq 2\pi\xi_{max}. \qquad (2.2.7)$$

Rewriting the equation for a Gaussian coherence function, we have

$$\frac{4\pi}{\lambda} + \frac{1}{2l_c} \leq \frac{2\pi}{\Delta} \qquad (2.2.8)$$

In the Mirau interference microscope the center wavelength is 500 nm and the coherence length is about 1.2 microns[42], so that the first term in Eq. (2.2.8) is the dominant term. Eq. (2.2.8) simply tells us that the short wavelength or coherence length tends to reduce the sampling distance in the scanning direction and increase the measurement time.

2.3 Hilbert transform algorithm

S. S. C. Chim[15] proposed an algorithm based on the Hibert transform for reconstructing a surface profile from correlograms. This is an alternative Fourier algorithm used when the DC component in the correlogram is constant, i.e. $c(x, y)$ in Eq. (2.1.1) does not have z dependence. The modulation part is easily separated from the fringes for a constant $c(x, y)$. Then the center lobe in Fourier domain in Eq. 2.2.1 is eliminated if the modulation part can be extracted:

$$i^m(x, y, z) = c(x, y)\gamma\left[z - h(x, y)\right]\cos\left[\frac{2\pi}{\lambda}2z - \alpha(x, y)\right]. \qquad (2.3.1)$$

Multiplying a signal function to $I^m(x,y,k) = F.T.[i^m(x,y,z)]$ to cut off the negative frequency part and then perform an inverse Fourier transform on the result, $c(x,y)\gamma[z - h(x,y)]e^{i[\frac{2\pi}{\lambda}2z - \alpha(x,y)]}$ is obtained. The above process can be expressed as a Hilbert transform as follows:

$$I.F.T.[I^m(x,y,k)step(k)] = i^m(x,y,z) * \frac{1}{2\pi}\left(\frac{1}{2}\delta(\frac{z}{2\pi}) - \frac{1}{iz}\right) \qquad (2.3.2)$$

$$= \frac{1}{2}\left\{i^m(x,y,z) + i\frac{1}{\pi}\int_{-\infty}^{\infty} i^m(x,y,z')\frac{1}{z-z'}dz'\right\}$$

$$= \frac{1}{2}\{i^m(x,y,z) + i\mathcal{H}[i^m(x,y,z)]\}.$$

The coherence envelope is recovered by taking the modulus of Eq. (2.3.2). The advantage of this Hilbert transform method is that direct discrete convolution may use less time than performing the Fourier transform twice as described in Section 2.2 when the Hilbert filter has a small width. Meanwhile, the disadvantage of this algorithm is that the modulation part has to be separated from the fringes first before doing the Hilbert transform. This is not a problem if the DC component is a constant throughout the vertical scan, but unfortunately that is not always the case. Fig. 2.4 shows a simple case, in which the DC component changes while scanning through the focus. When the objective is more than one focal length away from the sample, the effective numerical aperture (N.A.) is smaller than the N.A. of the objective. After going through the focus, the objective collects the amount of light defined by the N.A. of the objective. So the DC component increases until the objective scans through the focus and then flattens out. The effect shown in Fig. 2.4 is one of many aperture effects[11, 17], which are very important in both white light interferometry and phase-shifting interferometry. A detailed discussion on aperture effects can be found in references [11, 17]. Deck et al.[22] proposed a sophisticated way for picking up the AC or the modulation part from the fringes. When the scanning step Δ is
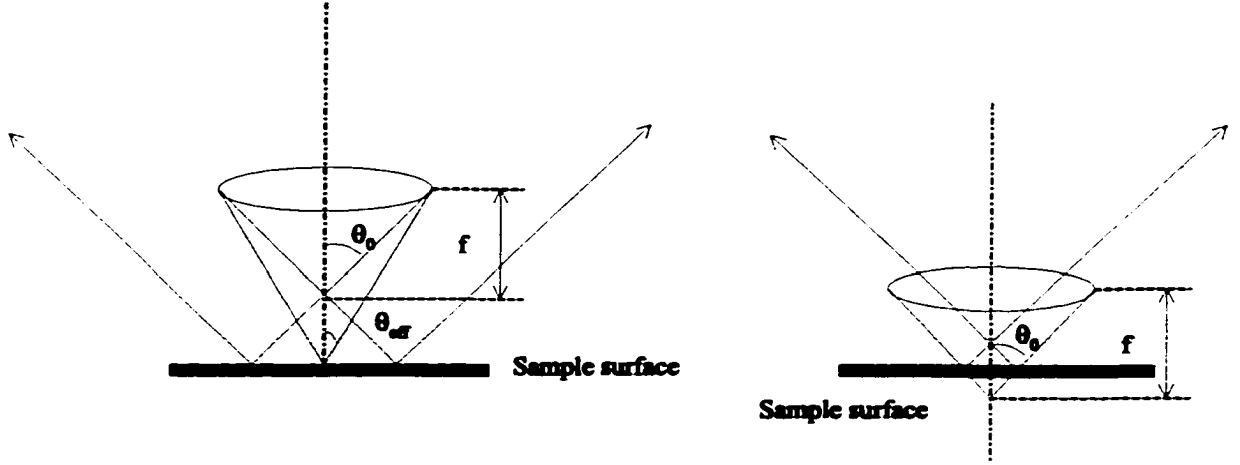
Figure 2.4: **The effective numerical aperture through vertical scanning.**

$\frac{\lambda}{8}$ or $\frac{3\lambda}{8}$ which correspond to 90° and 270° fringe shift per frame, the next neighbor frames are 180° apart, such that in discrete data point expression,

$$i(x, y, n\Delta) = A^2 + B^2 + \frac{c(x, y)}{2}\gamma\left[n\Delta - h(x, y)\right]\cos\left[\frac{2\pi}{\lambda}2n\Delta - \alpha\right] \qquad (2.3.3)$$

and

$$i(x, y, (n - 2)\Delta) \qquad (2.3.4)$$

$$= A^2 + B^2 + \frac{c(x, y)}{2}\gamma\left[(n - 2)\Delta - h(x, y)\right]\cos\left[\frac{2\pi}{\lambda}2n\Delta - \alpha - \pi\right]$$

$$= A^2 + B^2 - \frac{c(x, y)}{2}\gamma\left[(n - 2)\Delta - h(x, y)\right]\cos\left[\frac{2\pi}{\lambda}2n\Delta - \alpha\right].$$

Δ is the step size. If assuming $\gamma(z)$ is slowly varying compared to the cosine carrier, then

$$\gamma\left[(n - 2)\Delta - h(x, y)\right] \simeq \gamma\left[n\Delta - h(x, y)\right].$$

By taking the difference of Eq. (2.3.3) and Eq. (2.3.4), the resulting signal is

$$i^m(x, y, n\Delta) = c(x, y)\gamma\left[n\Delta - h(x, y)\right]\cos\left[\frac{2\pi}{\lambda}2n\Delta - \alpha\right]. \qquad (2.3.5)$$

The Hilbert transform algorithm can be applied to this signal according to the procedure proposed by Chim et al.[15]

A Hilbert transform has the frequency response,

$$H[e^{i\omega}] \quad = \quad -i \qquad 0 \leq \omega < \pi \tag{2.3.6}$$

$$= \quad i \qquad \pi \leq \omega < 2\pi.$$

The angular frequency ω is defined as $2\pi\xi_z\Delta$, where ξ_z is the spatial frequency along the z axis. The impulse response $h(n)$ of the Hilbert transform is given by[51]

$$h(n) \quad = \quad \frac{2}{\pi n} \qquad n \quad odd \tag{2.3.7}$$

$$= \quad 0 \qquad otherwise.$$

The discrete Hilbert transform can be written

$$\mathcal{H}[i^m(x,y,z)] \quad = \quad i^m(n) * h(n) \tag{2.3.8}$$

$$= \quad \sum_{m=-M}^{M} i^m(n-m)h(m).$$

$i^m(n)$ is the abbreviation of $i^m(x,y,n\Delta)$. $2M+1$ is the total number of the Hilbert filter elements. The impulse response $h(n)$ can be redefined as

$$h(n) \quad = \quad \frac{2}{\pi}\frac{1}{n} \qquad if \quad |n| \leq M \quad and \quad n \quad is \quad odd \tag{2.3.9}$$

$$= \quad 0 \qquad otherwise.$$

A finite number of elements introduces ripples into the ideal frequency response of the Hilbert transform. By choosing the sampling frequency close to the Nyquist rate, we can locate the spectrum of the correlogram signal near to the passband center of the Hilbert response, thus minimizing the effects of the ripples. Since the impulse
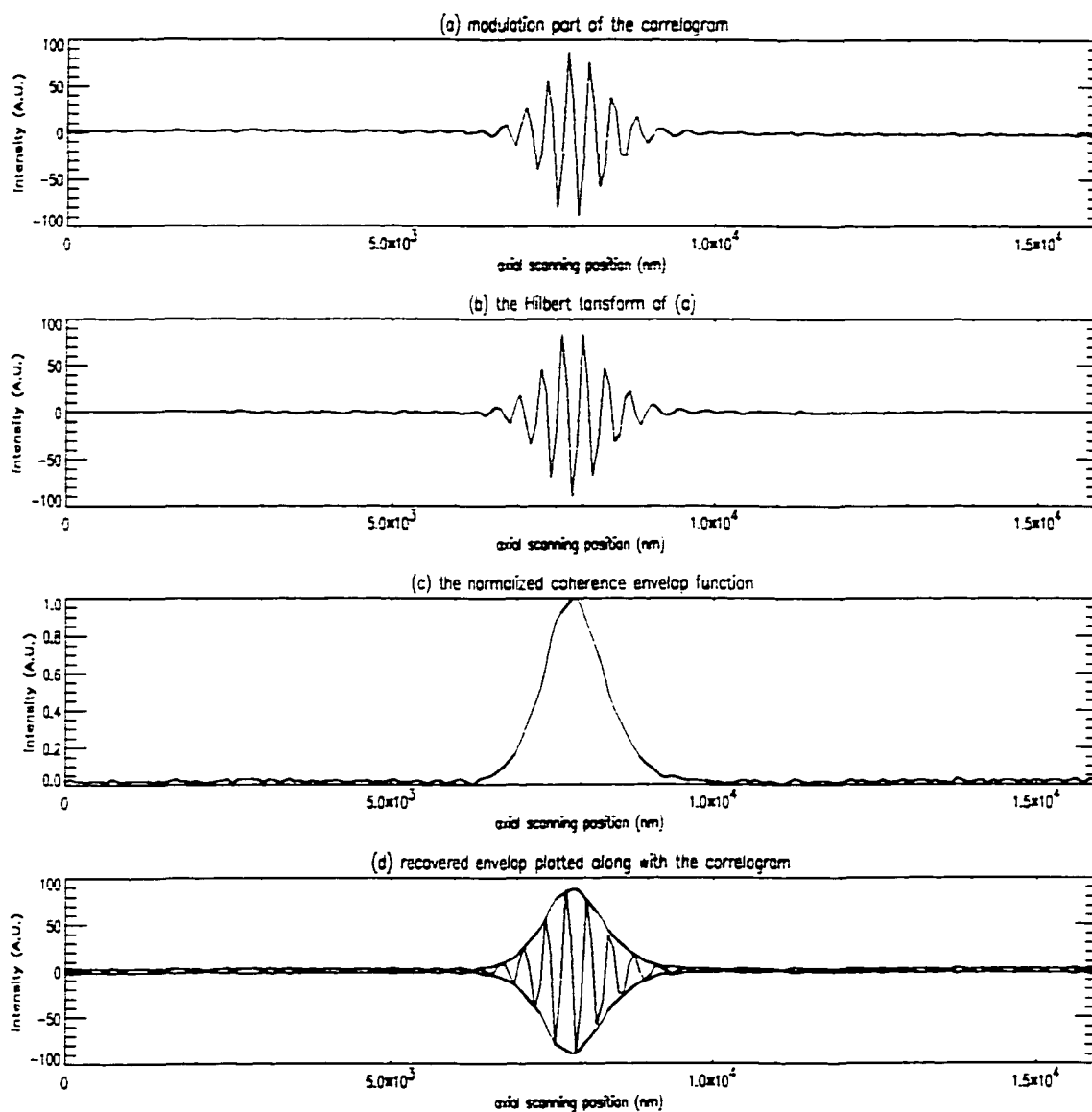
Figure 2.5: **The coherence envelope function obtained from the Hilbert transform algorithm. (a) The modulation part of the correlogram. (b) The Hilbert transform of (a). (c) The retrieved coherence envelope function (Normalized). (d) The coherence envelope function plotted along with the correlogram.**

response is antisymmetric about $n = 0$ and it is zero for even n, Eq. (2.3.8) simplifies to

$$\mathcal{H}[i^m(n)] = \frac{2}{\pi} \sum_{m=1;m \ odd}^{M} \frac{i^m(n-m) - i^m(n+m)}{m}.$$ (2.3.10)

The modulation contrast can be retrieved as

$$|\gamma(n)| = \sqrt{[i^m(n)]^2 + [\mathcal{H}[i^m(n)]]^2}.$$ (2.3.11)

The phase is

$$arg[\gamma(n)] = \arctan \left[\frac{\mathcal{H}[i^m(n)]}{i^m(n)} \right].$$ (2.3.12)

The number of nontrivial multiplications (or divisions) involved in a $2M + 1$ point Hilbert transform is $(M-1)/2$. which is a factor of 4 fewer than that of most other finite impulse response digital filters[51], as illustrated by Eq. (2.3.10). On the other hand, the number of operations required for the fast Fourier transform (FFT)[27] is $N \log_2 N$ complex additions and $\frac{1}{2}N \log_2 N$ complex multiplications, where N is the total number of the discrete data points. The Fourier transform algorithm described in the previous section must perform FFT twice, such that the number of total operations is $3N \log_2 N$. Hence a computing time reduction can be expected for the Hilbert transform algorithm by giving up some accuracy. Fig. 2.5 shows the procedure for $M = 30$ out of $N = 200$ data points. The recovered coherence envelope overlaps very well on the correlogram. The surface height can be determined by least square fitting (LSF) a Gaussian to the discrete data or calculating the centroid[35]. There will be discussion on the advantages and disadvantages of the LSF and centroid methods in later sections.

2.4 White light interferometry algorithms

These techniques come from phase-measurement interferometry (PMI) [18]. There is a separate review chapter on white light phase-shifting algorithms (WLPSI) and their error analysis later in this dissertation. As a result, only the principle of extracting the fringe contrast using PMI algorithms is covered in this section. PMI, as the name suggests, provides phase information of the fringes. However PMI also provides the coherence envelope while extracting the contrast from the correlogram during the scan in the z-direction.

If the OPD is varied by increments of $\lambda/4$ the following four frames of interference fringe data are obtained:

$$I_1 = I_0 \left[1 + \gamma \cos(\phi)\right] \tag{2.4.1}$$

$$I_2 = I_0 \left[1 + \gamma \cos\left(\phi + \frac{\pi}{2}\right)\right] = I_0 \left[1 - \gamma \sin(\phi)\right] \tag{2.4.2}$$

$$I_3 = I_0 \left[1 + \gamma \cos(\phi + \pi)\right] = I_0 \left[1 - \gamma \cos(\phi)\right] \tag{2.4.3}$$

$$I_4 = I_0 \left[1 + \gamma \cos\left(\phi + \frac{3\pi}{2}\right)\right] = I_0 \left[1 + \gamma \sin(\phi)\right] \tag{2.4.4}$$

This type of technique is mostly used to calculate the phase at each data point, i.e.

$$\phi = \arctan\left[\frac{I_4 - I_2}{I_1 - I_3}\right]. \tag{2.4.5}$$

However the same equation can be used to calculate the fringe visibility (or contrast)

$$\gamma = \frac{\sqrt{(I_4 - I_2)^2 + (I_1 - I_3)^2}}{2I_0}. \tag{2.4.6}$$

Performing Eq. (2.4.6) is not difficult and it can be easily calculated as the object is scanned. Moreover, the absolute value of the contrast is not important since we are only interested in the coherence peak location. The process can be implemented using the computer more easily by ignoring the denominator because the DC irradiance I_0 is assumed to be constant for each pixel. Also the peak location will be the same

whether or not the square root is taken. Therefore, we can simply keep track of

$$(2I_0\gamma)^2 = (I_4 - I_2)^2 + (I_1 - I_3)^2 \qquad (2.4.7)$$

for each pixel as the object is scanned in 90° increments.

This can be done with three phase steps as shown by Dresel et al[57]. There are three unknowns in Eq. (2.4.1), so three measurements are enough to determine I_0, γ and ϕ, if there are no system errors such as miscalibration of the phase shifter, nonlinearity due to the detector, quantization of the detector signal, reference surface errors, aberrations in the optics of the interferometer, air turbulence or vibrations. However, in practice there are always system errors, hence the algorithms have to be capable of compensating for these errors. The detailed discussion on these PMI algorithms can be found on Dr. J. C. Wyant's web site[28]. Hariharan's five frame error compensating algorithm[6] is discussed in this section since his algorithm is used extensively in later chapters.

The irradiance I_1, I_2, I_3, I_4 and I_5 are five consecutive frames separated by α in phase,

$$I_1 = I_0 \left[1 + \gamma \cos(\phi - 2\alpha) \right] \qquad (2.4.8)$$

$$I_2 = I_0 \left[1 + \gamma \cos(\phi - \alpha) \right] \qquad (2.4.9)$$

$$I_3 = I_0 \left[1 + \gamma \cos(\phi) \right] \qquad (2.4.10)$$

$$I_4 = I_0 \left[1 + \gamma \cos(\phi + \alpha) \right] \qquad (2.4.11)$$

$$I_5 = I_0 \left[1 + \gamma \cos(\phi + 2\alpha) \right]. \qquad (2.4.12)$$

When the phase shifting step α is close to 90° or 270°, the modulation contrast and phase can be expressed as

$$\gamma^2 \propto (I_2 - I_4)^2 + (I_1 - I_3)(I_3 - I_5). \qquad (2.4.13)$$

and

$$\phi = \arctan\left[\frac{\sqrt{4(I_2 - I_4)^2 - (I_1 - I_5)^2}}{-I_1 + 2I_3 - I_5}\right].$$ (2.4.14)

More information on error compensating algorithms can be found in references [47, 55, 56]. Fig. 2.6 shows the modulation contrast and the phase retrieved using Hariharan's five frame algorithm. The recovered modulation contrast overlaps very well with the correlogram. When the correlogram contains N discrete data points, the total operation required for this five frame algorithm is $3N$ additions and $2N$ multiplications. Thus this process has a computing speed much faster than those of the Fourier and Hilbert transform algorithms. The speed comparison of well-established coherence-peak-sensing algorithms is given later in this chapter.
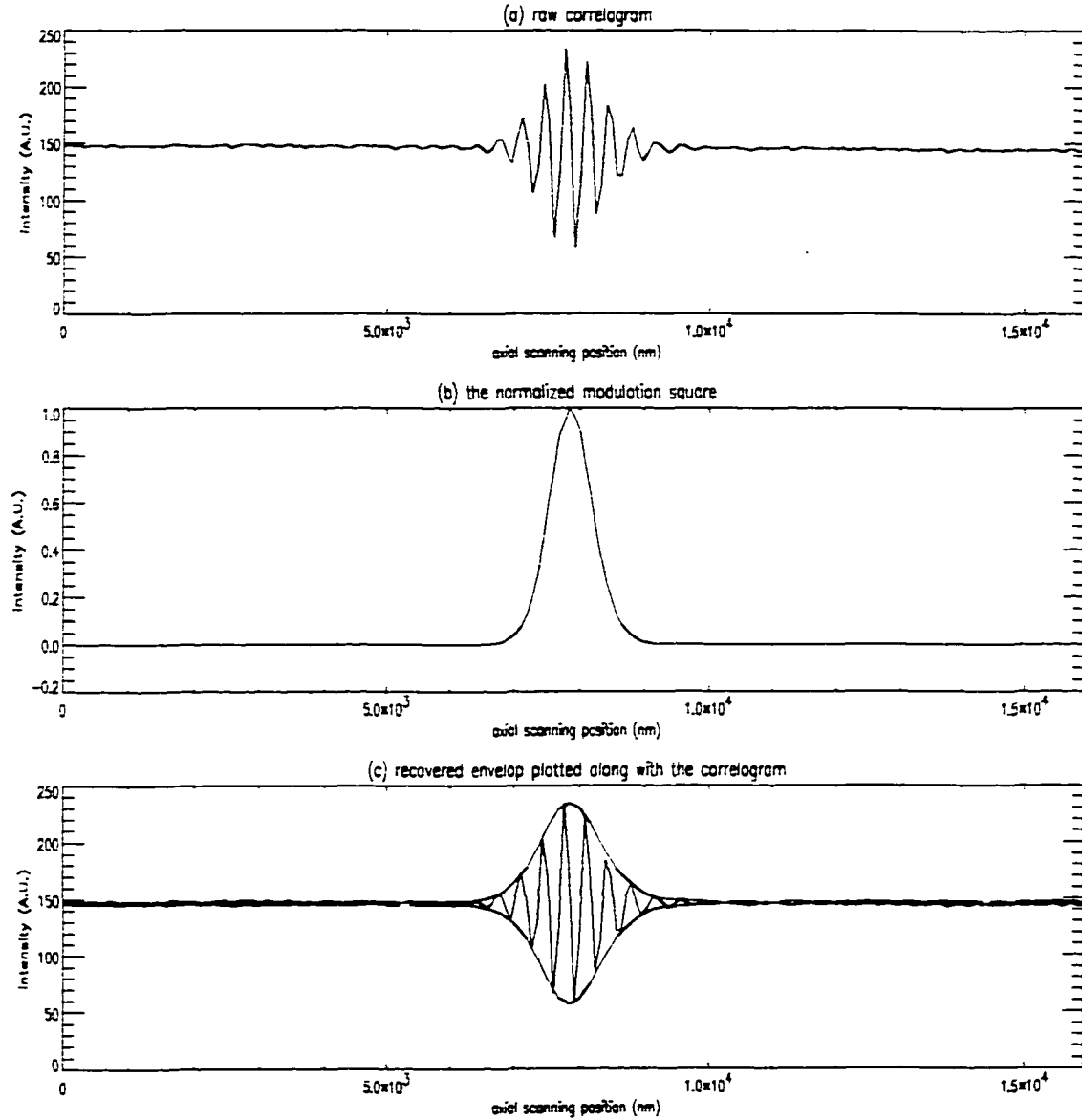
Figure 2.6: **The modulation contrast obtained from the five frame phase-shifting algorithm. (a) The raw correlogram obtained through vertical scanning. (b) The retrieved modulation contrast square (Normalized). (c) The modulation contrast plotted along with the correlogram.**

2.5 Wavelet transform algorithm

Although the wavelet transform technique is widely used in image recognition and classification, the first published paper applying the wavelet transform method to white light interferometry is Patrick Sandoz's paper[54] in 1997. The analysis in this section uses his method. For mathematical simplicity, in this section Eq. (2.1.1) is rewritten as

$$i(x, y, z) = i_{bg}(x, y) \left\{ 1 + c(x, y) \gamma \left[z(x, y) \right] \cos \left[4\pi\sigma_0 z + \alpha(x, y) \right] \right\}, \qquad (2.5.1)$$

where $\sigma_0 = \frac{1}{\lambda}$ is the mean wavenumber, while $i_{bg}(x, y)$ is the background irradiance, $c(x, y)$ is the fringe contrast, and $\gamma \left[z(x, y) \right]$ is the coherence envelope. Considering a light source with a Gaussian power spectrum density given by

$$B(\sigma) = \exp \left\{ - \left[\frac{\sigma - \sigma_0}{\Delta \sigma} \right]^2 \right\}, \qquad (2.5.2)$$

where σ_0 is the mean wavenumber and $\Delta \sigma$ represents the spectral width, it is easy to show that the coherence envelope is also a Gaussian function and can be expressed as

$$\gamma(z) = \exp \left[-(\frac{z}{l_c})^2 \right], \qquad (2.5.3)$$

where l_c represents the light source's coherence length. The output irradiance of the interferometer can be written as

$$i(x, y, z) = i_{bg}(x, y) + i_{bg}(x, y) c(x, y) \exp \left[-(\frac{z}{l_c})^2 \right] \cos \left[4\pi\sigma_0 z + \alpha(x, y) \right]. \qquad (2.5.4)$$

The wavelet transform[3] has been proposed as a solution to locate the coherence function peak position which occurs at the zero OPD position in most cases. Assuming

the carrier frequency of the correlograms is obtained from the calibration procedure, then a Gaussian envelope for the mother wavelet can be introduced as

$$\Psi(z) = \exp\left[-(\frac{z}{l_w})^2\right] \exp\left[i(4\pi\sigma_0 z)\right],\qquad(2.5.5)$$

where l_w represents the wavelet length (or duration) whose value will be discussed later in this section. That mother wavelet leads to a complete set of daughter wavelets expressed as a function of parameters **a** and **b**,

$$\Psi_{a,b}(z) = \sqrt{a}\Psi\left[\frac{z-b}{a}\right],\qquad(2.5.6)$$

where **a** is a parameter related to the frequency domain and to the investigation of different frequencies. For this particular application only the frequency of the mother wavelet is explored so that **a** is kept to 1, **b** is a parameter related to the spatial domain and corresponds to a translation of the wavelet along the z axis. The general form of the wavelet transform of a signal is given by the coefficient $W_{a,b}$,

$$\begin{aligned} W_{a,b} &= \int_{-\infty}^{\infty} i(z)\Psi_{a,b}(z)dz \qquad(2.5.7)\\ &= \int_{-\infty}^{\infty} i(z)\sqrt{a}\Psi\left[\frac{z-b}{a}\right]dz\\ &= i(z)\bigstar\Psi_{a,b}(z)\\ &= i(z) * \Psi_{a,b}^{*}(-z). \end{aligned}$$

The argument and the modulus of the complex number $W_{a,b}$ give the phase $\phi_{a,b}$ and the modulus $I_{a,b}$, respectively.

In the case of the application to the location of the white light source correlogram, $\phi_{1,b}$ represents the relative phase difference between the correlogram and the mother wavelet centered in $z = b$, whereas $I_{1,b}$ represents their degree of overlap. If the correlogram is located at $z = b$, then $I_{1,b}$ is the maximum value.

Correlograms are usually formed by discrete signals, Eq. (2.5.7) must be rewritten in a finite summation series instead of the integral. We define the following series,

$$\Psi_k = \exp\left[-\left(\frac{k\delta z}{l_w}\right)^2\right]\exp[i(4\pi\sigma_0 k\delta z)], \tag{2.5.8}$$

where δz is the sampling distance used for the data acquisition and k is an integer that varies from $-N$ to $+N$. The value of N has to be adapted to the wavelet length and to the sampling distance to ensure the correct sampling of the corresponding continuous wavelet.

For any position z_j along the vertical scanning, a wavelet coefficient can be computed as follows:

$$W_{i,j} = \sum_{k=-N}^{N} \Psi_k i(z_j + k\delta z). \tag{2.5.9}$$

There would be an optimal value of l_w. A larger value of l_w reduces the ultimate error made in the phase measurement, but a larger z variation has to be considered, and the value of N as well as the computation time is increased. Hence the optimal value of l_w is the shortest length in which the phase accuracy is limited only by the detection signal-to-noise ratio and not by too short a value l_w, while the short value N, which determines the computation time, is kept.

It is clear from Eq. (2.5.7) that the wavelet transform modulus corresponds not to the fringe envelope but to the following convolution product,

$$G(z) = \exp\left[-(\frac{z}{l_c})^2\right] * \exp\left[-(\frac{z}{l_w})^2\right], \tag{2.5.10}$$

and locates at $z = b$. By calculating the centroid of $W_{1,b}$, the surface height is determined.
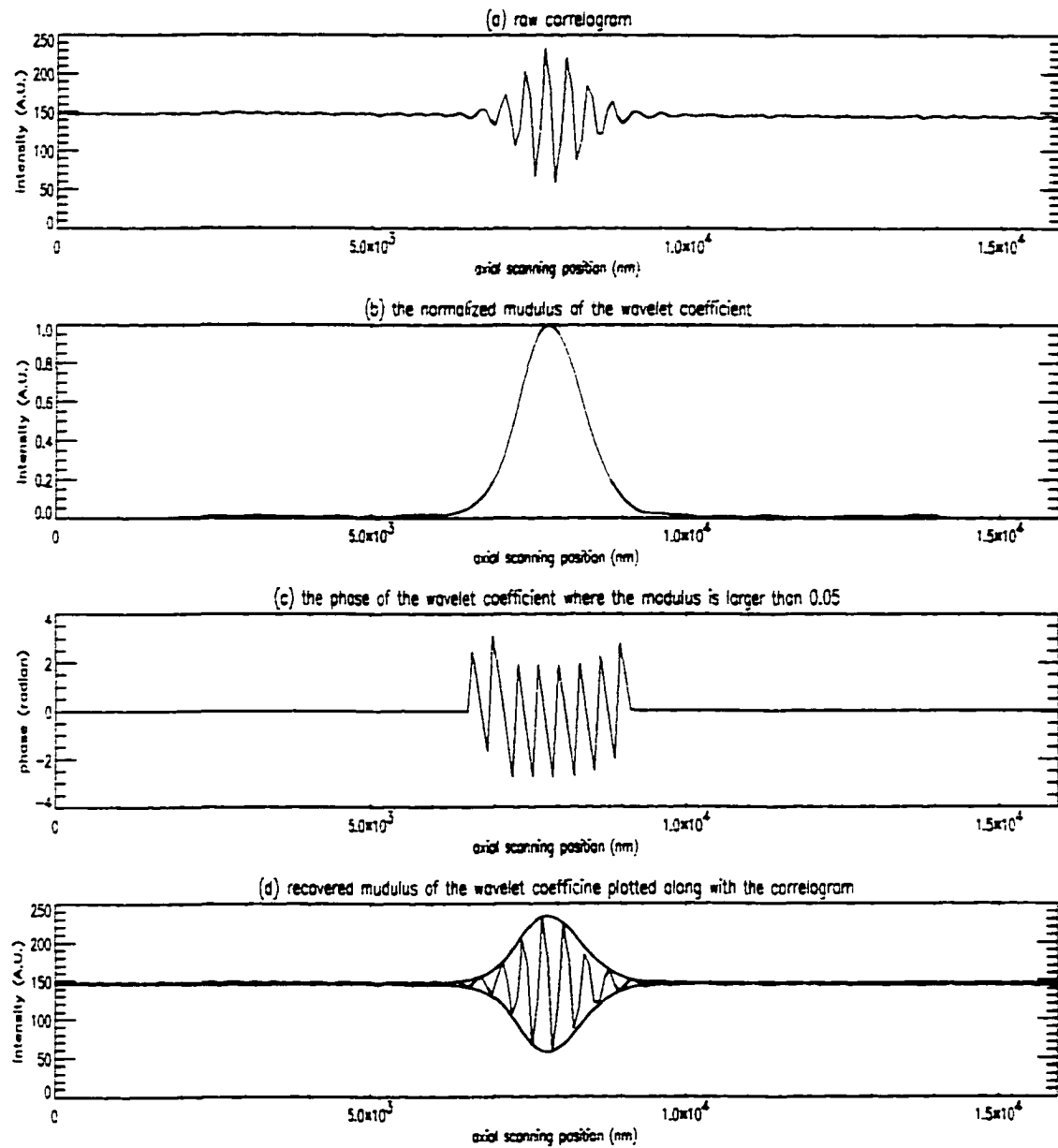
Figure 2.7: **The wavelet coefficient calculated from daughter wavelets with wavelet length** $l_w = \frac{\lambda}{2}$. **(a) The raw correlogram. (b) The modulus of the wavelet coefficient. (c) The phase of the wavelet coefficient. (d) The modulus of the wavelet coefficient plotted along with the correlogram.**

Fig. 2.7 shows the modulus and phase of the wavelet coefficient along with correlogram to demonstrate the wavelet transform algorithm. The calculation is performed with the parameters, $N = 25$, $l_w = \frac{\bar{\lambda}}{2} = 300$ nm. The coherence length l_c here is 1.2 microns and the wavelet length l_w is 300 nm, so that the coefficient width is dominated by the coherent length.

2.6 WYKO's centroid approach

This is a patented algorithm[5] which requires probably the least computing time of published algorithms. Ai et al. found that the centroid of the function,

$$m(n) = [i(n) - i(n - 1)]^2 \qquad (2.6.1)$$

is a good estimator for the surface height. It can be shown as follows. For mathematical simplicity the continuous expression for correlograms:

$$i(n) = i_{avg} + c\gamma \left[z - h\right] \cos \left[\frac{2\pi}{\bar{\lambda}} 2z\right] \qquad (2.6.2)$$

$$i(n - 1) = i_{avg} + c\gamma \left[z - \frac{\bar{\lambda}}{8} - h\right] \cos \left[\frac{2\pi}{\bar{\lambda}} 2(z - \frac{\bar{\lambda}}{8})\right] \qquad (2.6.3)$$

$$= i_{avg} + c\gamma \left[z - \frac{\bar{\lambda}}{8} - h\right] \sin \left[\frac{2\pi}{\bar{\lambda}} 2z\right]$$

is used.

$\gamma(z)$ is slowly varying so that $\gamma(z-h) \approx \gamma\left[z - \frac{\lambda}{8} - h\right]$ is a proper approximation, then $m(z) = m(n)$ can be written as

$$
\begin{aligned}
m(z) &= \left\{c\gamma\,(z-h)\left[\cos\left(\frac{2\pi}{\lambda}2z\right) - \sin\left(\frac{2\pi}{\lambda}2z\right)\right]\right\}^2 \qquad (2.6.4)\\
&= 2c^2\gamma^2\,(z-h)\cos^2\left(\frac{2\pi}{\lambda}2z + \frac{\pi}{4}\right)\\
&= c^2\gamma^2\,(z-h)\left[1 + \cos\left(\frac{2\pi}{\lambda}4z + \frac{\pi}{2}\right)\right]\\
&= c^2\gamma^2\,(z-h)\left[1 - \sin\left(\frac{2\pi}{\lambda}4z\right)\right]\\
&= \hat{\gamma}\,(z-h)\left[1 - \sin\left(\frac{2\pi}{\lambda}4z\right)\right].
\end{aligned}
$$

Here $c^2\gamma^2(z)$ is rewritten as $\hat{\gamma}(z)$. Then the centroid is calculated as

$$
\begin{aligned}
\bar{z} &= \frac{\int_{-\infty}^{\infty} z m(z)dz}{\int_{-\infty}^{\infty} m(z)dz} \qquad (2.6.5)\\
&= \frac{M'(0)}{-i2\pi M(0)}.
\end{aligned}
$$

$M(\xi)$ and $M'(\xi)$ are the Fourier transform of $m(z)$ and its first derivative, respectively. They are

$$
M(\xi) = \Gamma(\xi)e^{-i2\pi\xi h} - \frac{1}{2i}\left[\Gamma\left(\xi - \frac{4}{\lambda}\right)e^{-i2\pi(\xi-\frac{4}{\lambda})h} - \Gamma\left(\xi + \frac{4}{\lambda}\right)e^{-i2\pi(\xi+\frac{4}{\lambda})h}\right] \qquad (2.6.6)
$$

and

$$
\begin{aligned}
M'(\xi) &= \left[\Gamma'(\xi) - i2\pi h\Gamma(\xi)\right]e^{-i2\pi\xi h} - \frac{1}{2i}\left\{\left[\Gamma'\left(\xi - \frac{4}{\lambda}\right) - i2\pi h\Gamma\left(\xi - \frac{4}{\lambda}\right)\right]e^{-i2\pi(\xi-\frac{4}{\lambda})h}\right.\\
&\quad \left. - \left[\Gamma'\left(\xi + \frac{4}{\lambda}\right) - i2\pi h\Gamma\left(\xi + \frac{4}{\lambda}\right)\right]e^{-i2\pi(\xi+\frac{4}{\lambda})h}\right\}, \qquad (2.6.7)
\end{aligned}
$$

where $\Gamma(\xi)$ is the Fourier transform of $\hat{\gamma}(z)$.

Assuming a Gaussian envelope, then the Fourier transform of a Gaussian is still a Gaussian. $\Gamma(\xi)$ has the following properties:

$$\Gamma(0) = Maximum$$

$$\Gamma(-\xi) = \Gamma(\xi)$$

$$\Gamma'(0) = 0$$

$$\Gamma(-\xi) = -\Gamma(\xi).$$

When evaluating $M(\xi)$ and $M'(\xi)$ at $\xi = 0$, we have

$$M(0) = \Gamma(0) - \frac{1}{2i}\left[\Gamma\left(-\frac{4}{\lambda}\right)e^{i2\pi\frac{4}{\lambda}h} - \Gamma\left(\frac{4}{\lambda}\right)e^{-i2\pi\frac{4}{\lambda}h}\right]$$

$$= \Gamma(0) + \Gamma\left(\frac{4}{\lambda}\right)\sin\left(2\pi\frac{4}{\lambda}h\right) \tag{2.6.8}$$

and

$$M'(0) = \Gamma'(0) - i2\pi h\Gamma(0) - \frac{1}{2i}\left\{\left[\Gamma'\left(-\frac{4}{\lambda}\right) - i2\pi h\Gamma\left(-\frac{4}{\lambda}\right)\right]e^{i2\pi\frac{4}{\lambda}h}\right.$$

$$\left. - \left[\Gamma'\left(\frac{4}{\lambda}\right) - i2\pi h\Gamma\left(\frac{4}{\lambda}\right)\right]e^{-i2\pi\frac{4}{\lambda}h}\right\} \tag{2.6.9}$$

$$= -i\Gamma'\left(\frac{4}{\lambda}\right)\cos\left(2\pi\frac{4}{\lambda}h\right) - i2\pi h\left[\Gamma(0) + \Gamma\left(\frac{4}{\lambda}\right)\sin\left(2\pi\frac{4}{\lambda}h\right)\right].$$

After substituting the above equations, the centroid is expressed as

$$\bar{z} = h + \frac{\Gamma'\left(\frac{4}{\lambda}\right)\cos\left(2\pi\frac{4}{\lambda}h\right)}{2\pi\left[\Gamma(0) + \Gamma\left(\frac{4}{\lambda}\right)\sin\left(2\pi\frac{4}{\lambda}\right)h\right]}. \tag{2.6.10}$$

As discussed in Section 2.2, the Fourier transform of the coherent envelope has the width of $\Delta\xi = \frac{1}{4\pi l_c} = \frac{1}{4\pi}\frac{\Delta\lambda}{\lambda^2}$. Using $\bar{\lambda} = 0.6$ microns and $\Delta\lambda = 0.3$ microns, we have $\frac{4}{\lambda} = 6.7$ and $\Delta\xi = 0.066$ lines/micron. The spatial $\frac{4}{\lambda}$ is far from the center so that $\Gamma(\frac{4}{\lambda})$ is very small compared to $\Gamma(0)$. Thus the second term of Eq. (2.6.10) can be eliminated and WYKO's algorithm does give us the correct height estimation from correlograms.

2.7 Phase slope algorithm

This is an algorithm introduced and used by ZYGO Corporation[22]. It is regarded as a fast algorithm since it only requires one Fourier transform. The mathematics is very simple and Section 2.2 provides enough information for its derivation. Eq. (2.2.1) says that the phase slopes of sidelobes of the Fourier transformed correlogram give us the height information. First of all, the correlogram must be Fourier transformed, and then one of the sidelobes is filtered out. The phase of the sidelobe can be expressed as

$$\phi(k) = -2\pi k h(x, y) + \alpha(x, y). \tag{2.7.1}$$

Then the surface height can be calculated by taking the phase slope,

$$h(x, y) = -\frac{1}{2\pi} \frac{d\phi(k)}{dk}. \tag{2.7.2}$$

The computing time is expected to be half that of the Fourier transform algorithm discussed in Section 2.2, since this algorithm only requires one Fourier transform. As supplemental information, the modulus of the sidelobe could be used as the weighting factor for better accuracy in linear fitting.

2.8 3-dimensional surface profiles

Well-established algorithms to extract 3-dimensional surface data with vertical scanning interferometry have been described. In this section they are applied to profiling a step height standard (VLSI Standards Inc., SHS4600Å) for demonstration purpose. Fig. 2.8 shows profiles obtained by various algorithms. Not surprisingly, the profiles look very similar despite the different processes. Interestingly, they all
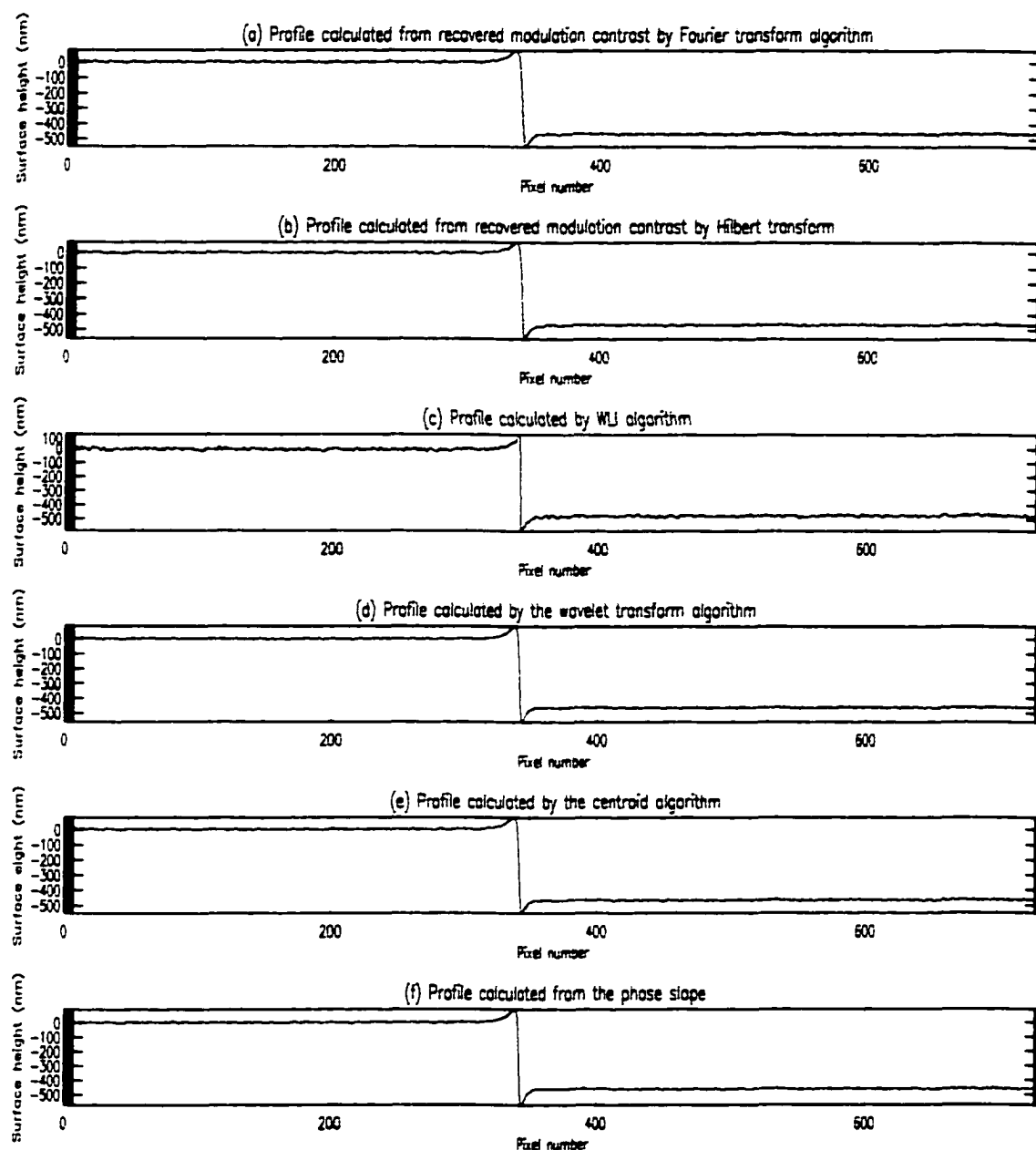
Figure 2.8: **The surface profile obtained from various vertical scanning algorithms. (a) Calculated by FFT algorithm. See Section 2.2. (b) Calculated by Hilbert transform algorithm. See Section 2.3. (c) Calculated by WLI algorithms. See Section 2.4. (d) Calculated by wavelet transform algorithm. See Section 2.5. (e) Calculated by WYKO's centroid approach. See Section 2.6. (f) Calculated by the phase slope algorithm. See Section 2.7.**

Table 2.1: The number of operations required for recovering the fringe modulation envelope.

Algorithm	Number of Additions/Subtractions	Number of Multiplications/divisons
Fourier Transform	$2N \log_2 N$	$N \log_2 N$
Hilbert Transform	$N \frac{J-3}{4}$	$N \frac{J-3}{2}$
WLI	$3N$	$2N$
Wavelet Transform	$N(J-1)$	NJ
WYKO	$N-1$	
ZYGO	$N \log_2 N$	$\frac{1}{2} N \log_2 N$

Table 2.2: The number of operations required for locating the fringe modulation peak position between discrete data points.

	Number of Additions/ Subtractions	Number of Multiplications/ divisions	Number of Other Operations
Fourier Transform	$2(N-1)$	$N+1$	
Hilbert Transform	$2(N-1)$	$N+1$	
WLI	5	3	5
Wavelet Transform	$2(N-1)$	$N+1$	
WYKO	$2(N-2)$	N	
ZYGO	4J-1	5J+1	
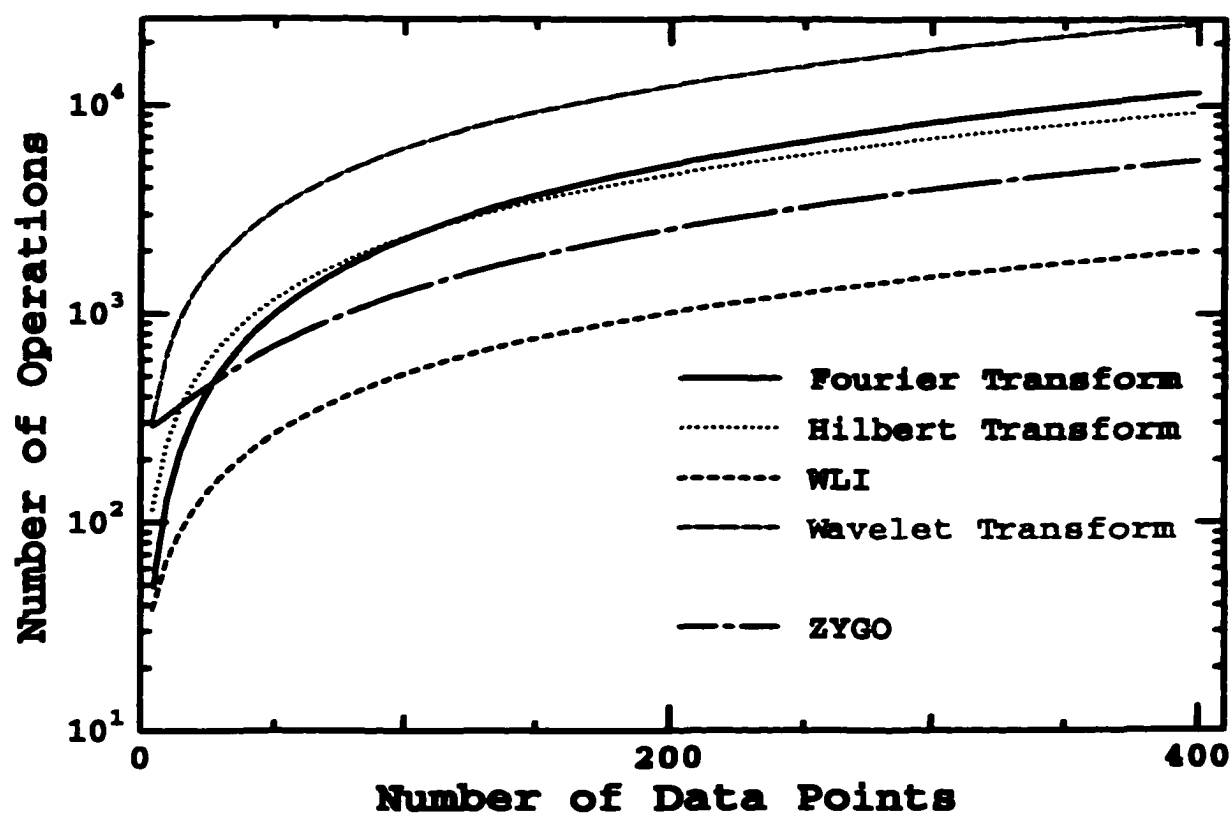
Figure 2.9: **The number of operations required for each algorithm as a function of the number of data points in correlograms.**

show the bat wings artifact at the step edges. That is why we need to develop a new algorithm to remove the bat wings and reveal the surface profile close to the edge.

The required operations in each algorithm are summarized in Table 2.1 and 2.2, which gives us the idea about their speed so that we can determine which ones are fast algorithms and which ones are not. Here J is the number of points contained in the coherence envelope, which determines the Hilbert kernel length, the wavelet length, as well as the number of data points for LSF in ZYGO's algorithm. N is the total number of data points in the correlogram. When the WYKO NT-2000 operates in the vertical scanning interferometry (VSI) mode, the coherence length of the light source is about 1.2 microns. Therefore there are about 30 data points under the coherence envelope. The other operations appearing in the WLI algorithm (in Table 2.2) are the logarithms of five consecutive data values of fringe modulation contrast. Fig. 2.9 shows the total number of operations required for each algorithm as a function of N, where J is chosen to be 30. The figure indicates that WYKO's algorithm is an extremely fast algorithm compared to the others. The five frame WLI algorithm ends up in second place, which is beneficial since it is adopted to our PSI on the Fly techniques.

2.9 Error Analysis

From the previous section, it is clear that the five frame WLI algorithm and WYKO's centroid approach can be regarded as practical algorithms in terms of their processing speed. In this section the error tolerance of these two methods is derived and discussed.

There are many noise sources in the WLI measurement, being a combination of such factors as vibration, photon noises, CCD noise, quantization and motor error, to

Table 2.3: rms peak location error for WLI and centroid algorithm of 90° scanning step. The error is in the unit of sampling spacing.

	Peak Detection	Centroid
0%	0.0197880	0.00771274
2%	0.152480	0.152374
4%	0.298653	0.524230
6%	0.449208	1.05861
8%	0.600702	1.67120
10%	0.739864	2.29154

name just a few. They are rather complicated, so a great simplification without losing generality is required. Two well-defined noises, zero-mean Gaussian intensity noise and long period motor error can be easily treated. The former case can be considered the combination of all the noises except motor error. The latter specifically describes the error coming from the motor nonlinearity, i.e. the sampling step errors. In the next two sections we will find that the WLI peak detection algorithm is less sensitive to the Gaussian distribution intensity noise and the centroid approach has better noise resistance for periodic motor noise. However since the Gaussian intensity noise has a much larger effect to the surface profile, we can conclude that the WLI peak detection algorithm is superior from the noise resistance point of view.

2.9.1 Gaussian intensity noise
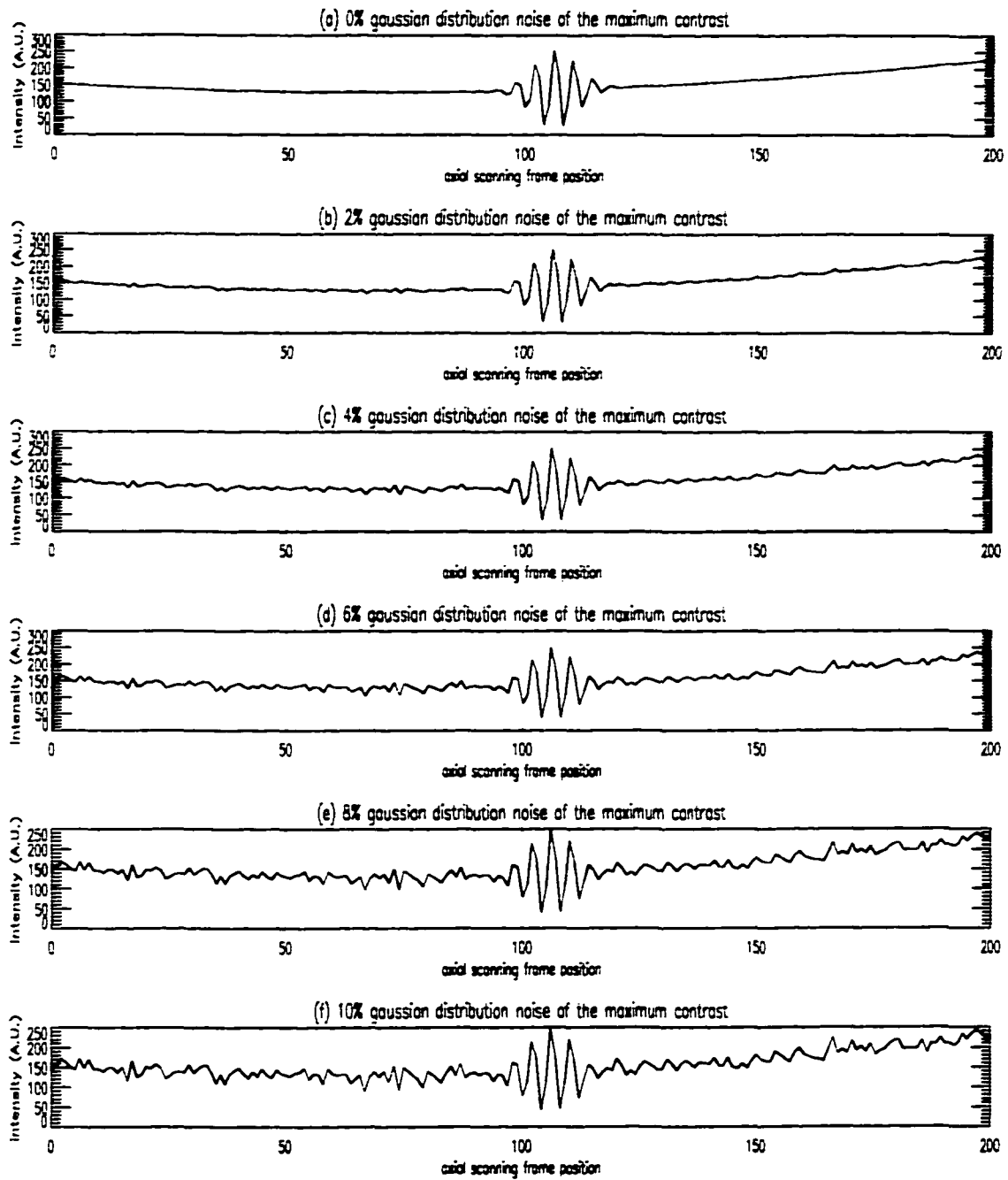
Figure 2.10: **Simulated correlograms of 90° scanning step with 0-10% Gaussian distribution random noise of maximum contrast.**
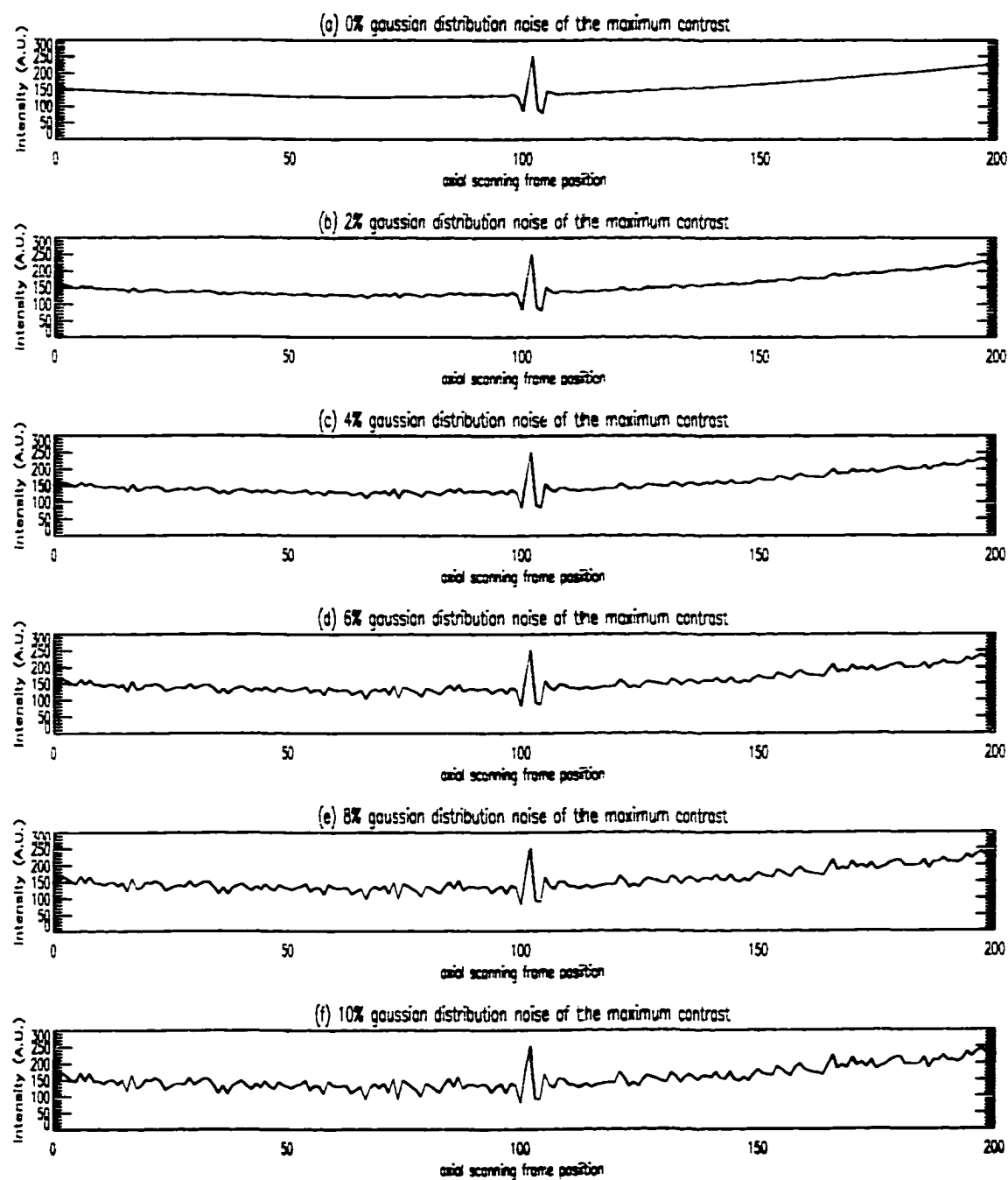
Figure 2.11: **Simulated correlograms of 270° scanning step with 0-10% Gaussian distribution random noise of maximum contrast.**

Table 2.4: rms peak location error for WLI and centroid algorithm of 270° scanning step. The error is in the unit of sampling spacing.

	Peak Detection	Centroid
0%	0.0126826	0.0134024
2%	0.0403260	0.384479
4%	0.0786758	1.30888
6%	0.117758	2.37689
8%	0.157198	3.32850
10%	0.196578	4.08478
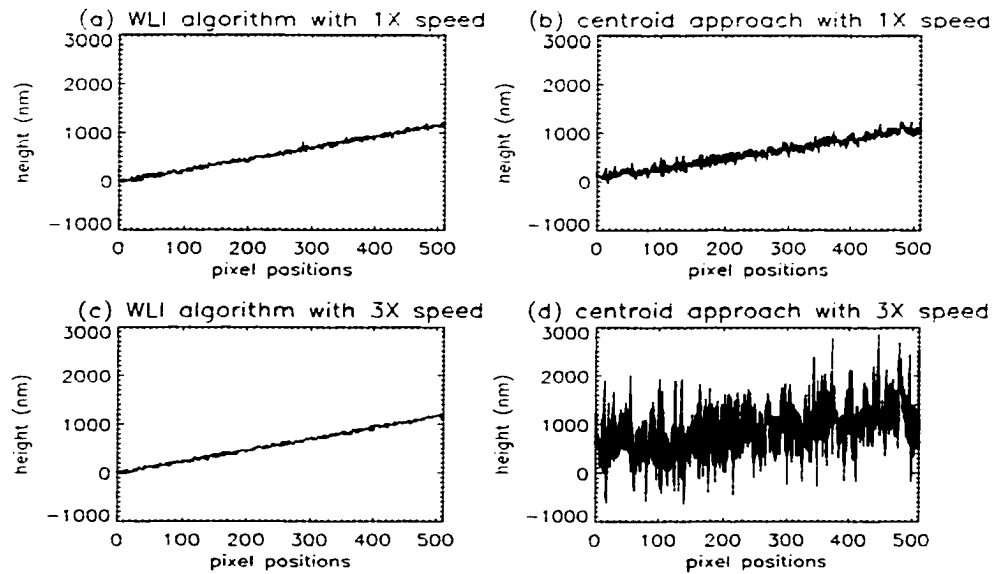
Figure 2.12: **The surface profile obtained from simulated correlograms with 6% Gaussian distribution random noise of maximum contrast.**

The Gaussian intensity noise case is discussed first. The treatment is simple. And for further simplicity we use a tilted surface, such that we can break down our problem to a 1-dimensional line without losing generality. Assuming that the coherence envelope is Gaussian (for most cases it is), the intensity data in a correlogram can be written as

$$i(x, z) = INT \left[\frac{2^8}{2} + \frac{2^8}{2} \exp \left(\frac{-z_s^2}{\sigma^2} \right) \cos \left(\frac{2\pi}{\lambda} 2z_s \right) + n(x, z) + background \right] \quad (2.9.1)$$

for an 8-bit camera system with a maximum modulation contrast of 1. The $INT(\cdot)$ function rounds down the argument input. The z sample locations are defined by $z_s = z - h(x)$, where $h(x)$ is the surface shape. For the simple case of a tilted surface with 4 fringes across it, $h(x)$ is of the form $\frac{4\frac{\lambda}{2}}{512}x - 100\Delta$ for 512 lateral points. $n(x, z)$ is the zero-mean Gaussian distributed random noise with a standard deviation (or rms) value specified in the range of 0%-10% of the maximum modulation value. $\sigma = 6.7\Delta$ is selected so that the correlogram has about same width fringes as in the actual case. To make the correlogram more realistic, a small z^2 background intensity is added. Fig. 2.10 shows the simulated correlograms with various $n(x, z)$ for a 90° sampling step or 1X speed. And the rms roughness, defined as

$$R_q = \sqrt{\frac{1}{N} \sum_{i=1}^{N} [z(i) - z_{fit}(i)]^2}, \quad (2.9.2)$$

is shown in Table 2.3 in the unit of sampling spacings. The z_{fit} is the fitted surface from the simulated correlogram.

The same analysis can be applied to the 270° scanning step case as well. The correlogram is shown in Fig. 2.11 and the rms error is listed in Table 2.4. To visualize how noise affects the surface profile, Fig. 2.12 shows the processed surface profiles from the simulated correlograms with Gaussian noise that is 6% of the maximum

modulation for both the 1X and 3X speeds. The WLI algorithm which seeks the actual envelope peak possesses more noise resistance for the Gaussian distributed random noise, compared to the centroid approach. This explains why peak detection gives better repeatability than centroid calculation, which is well known in the interference microscope community.

2.9.2 Motor noise

Now moving on to periodic motor noise, in our setup of a Mirau interferometer the motor has about $\pm10\%$ step error when it moves about 1 mm. The scanning step can be modeled as

$$\Delta(z) = \Delta_0 + \Delta_{error} \sin\left[2\pi\frac{z - z_0}{L}\right] \qquad (2.9.3)$$

where L is the period of the motor error and z_0 is the position where the motor has an exactly calibrated step Δ_0. For a real system L is in the mm range and Δ_{error} is about 10% of the 90° scanning step, such that $\Delta_{error} = 0.1\Delta_0$. Fig. 2.13 shows the simulated correlogram with this motor noise, and Table 2.5 summarizes the rms errors in scanning steps. The results tell us that the motor error does not affect the surface profiling significantly compared to the Gaussian distribution intensity error we discussed in the previous section. Interestingly, the rms error in the surface profile for the 1X speed from the motor error has a smaller value when processed by the centroid approach. Maybe this will become clear if we examine the correlogram. The modulation of the fringes looks like

$$M(z') = \gamma(z' - h)\cos\left[\frac{2\pi}{\lambda}2(z' - h)\right], \qquad (2.9.4)$$

where z' can be expressed as

$$z' = z + \Delta_{error} \sin\left[2\pi\frac{z - z_0}{L}\right].$$
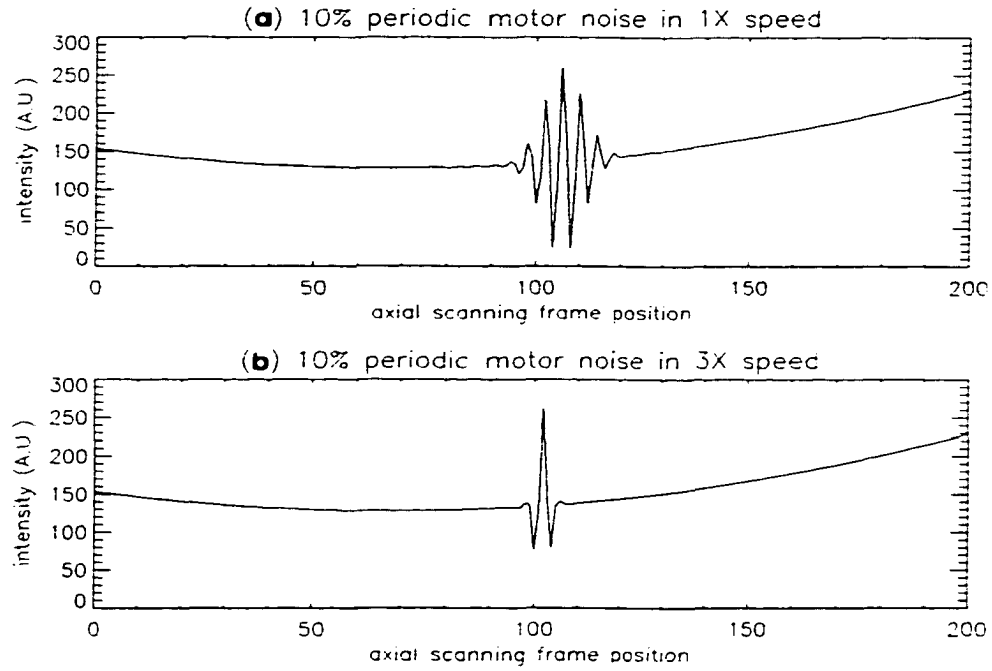
Figure 2.13: **Simulated correlograms with 10% periodic motor noise.** (a) 90° **phase shift (1X speed).** (b) 270° **phase shift (3X speed).**

Table 2.5: rms peak location error for WLI and centroid algorithm. The error is in the unit of sampling spacing.

	Peak Detection	Centroid
90°(1X speed)	0.0195672	0.00775160
270°(3X speed)	0.0127999	0.0131333
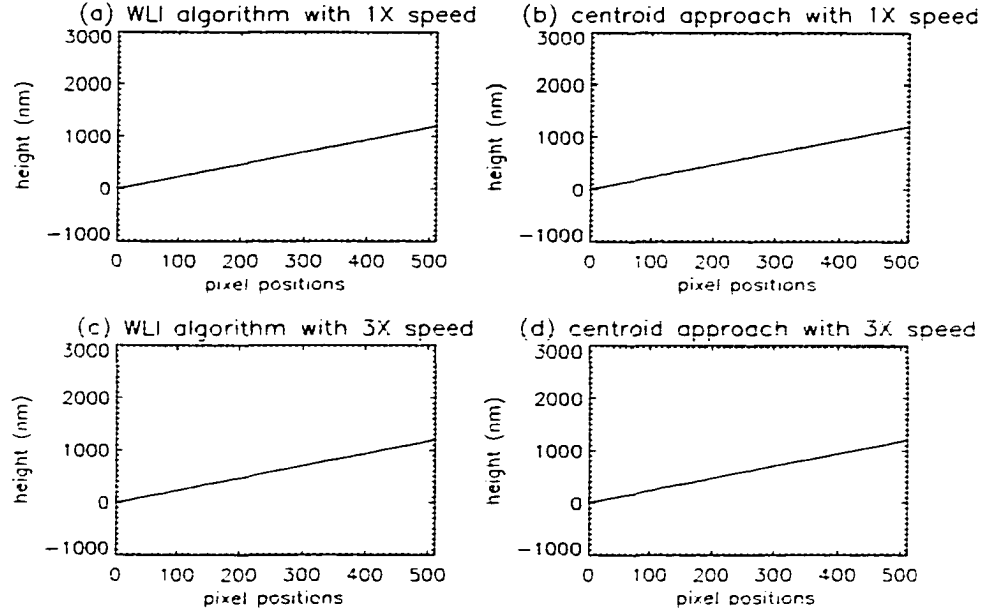
Figure 2.14: **The surface profile obtained from simulated correlograms with 10% periodic motor noise.**

Rewrite $M(z)$ with z and we obtain

$$M(z) = \gamma \left\{ z + \Delta_{error} \sin\left[2\pi\frac{z-z_0}{L}\right] - h \right\} \cos\left\{ \frac{2\pi}{\lambda}2\left[z + \Delta_{error} \sin\left[2\pi\frac{z-z_0}{L}\right] - h\right]\right\},$$

$$(2.9.5)$$

assuming that somehow the envelope $\gamma\left\{ z + \Delta_{error} \sin\left[2\pi\frac{z-z_0}{L}\right] - h \right\}$ is recovered. Here $\Delta_{error} \ll z - h$, so that γ can be expanded around $z - h$:

$$\hat{\gamma}(z) = \gamma\left\{ z + \Delta_{error} \sin\left[2\pi\frac{z-z_0}{L}\right] - h \right\} \qquad (2.9.6)$$

$$= \gamma(z - h) \qquad (2.9.7)$$

$$+\gamma'(z - h)\Delta_{error} \sin\left[2\pi\frac{z-z_0}{L}\right]$$

$$+\frac{1}{2}\gamma''(z - h)\left\{ \Delta_{error}^2 \sin\left[2\pi\frac{z-z_0}{L}\right] \right\}^2 + \cdots.$$

Now we must analyze the above equation for two cases: one in which the period of the motor error is much smaller than the scanning length, and the other in which it is much larger than the scanning length. For the first case, the second and higher terms oscillate in much higher frequencies than the first term. Thus only the first term remains in the centroid,

$$\frac{\int dz\, z\hat{\gamma}(z)}{\int dz\, \hat{\gamma}(z)},$$

so the centroid results in the correct estimation despite the existence of noise. Now look at the second case: the period L is much larger than the scan length. The sin function in Eq. (2.9.6) can be approximated as

$$\sin\left[\frac{2\pi}{L}(z-z_0)\right] \approx \frac{2\pi}{L}(z-z_0). \tag{2.9.8}$$

Then the modulation can be expressed as

$$\hat{\gamma}(z) = \gamma\left\{z + \Delta_{error}\sin\left[2\pi\frac{z-z_0}{L}\right] - h\right\} \tag{2.9.9}$$

$$= \gamma(z-h) \tag{2.9.10}$$

$$+\gamma'(z-h)\Delta_{error}2\pi\frac{z-z_0}{L}$$

$$+\frac{1}{2}\gamma''(z-h)\left\{\Delta_{error}2\pi\frac{z-z_0}{L}\right\}^2 + \cdots.$$

When calculating the centroid of this function, since $\Delta_{error}2\pi\frac{z-z_0}{L}$ is a slow varying function, the integral only has significant contribution from the neighborhood of $z = h(x,y)$, where $\gamma(z-h)$, $\gamma'(z-h)$ and $\gamma''(z-h)$ have non-zero values. The range of non-zero $\gamma(z-h)$ and its derivatives is the coherence length of the white light source, and over this range $\Delta_{error}2\pi\frac{z-z_0}{L}$ and its higher powers have only very small variations, such that the contribution to the centroid equation from the second and higher terms in Eq. (2.9.9) is less than Δ_{error} itself. By integrating the influence of the motor noise

is effectively reduced. Comparing this to the WLI peak detection algorithm which can be thought of as having the maximum peak shift of $\Delta_{error} \times (total\ scan\ length)$, less rms noise is expected in the centroid approach.

2.10   Conclusion

Coherence-peak-sensing algorithms have been reviewed. Among the discussed algorithms, the WLI algorithm and WYKO's centroid approach are practical methods to retrieve surface profiles from correlograms in regard to the required computing time, which is a very important commercial issue. After a simple error analysis by comparing the noise resistivity between the WLI algorithm and WYKO's centroid approach, we conclude that the WLI algorithm is preferred, since it reduces rms errors significantly in surface profiles.

Chapter 3

PHASE CHANGE UPON REFLECTION

In this chapter the phase change upon reflection from a test surface is discussed. The dispersion of the substrate's refractive index and extinction coefficient is analyzed and its influence on the white light coherence envelope of correlograms is estimated.

3.1 Introduction

The phase change upon reflection of a test surface has been treated as a constant for all wavelengths contained in the white light source in previous chapters. This is true for glasses with an extinction coefficient $\kappa = 0$, but for non-zero extinction coefficients, as in metals, the dispersion effect of the phase change must be examined in a more rigorous way. In the next section we first discuss the wavenumber dependence of the phase change for several materials, and then in Section 3.3 we see how the dispersion of the phase change upon reflection changes the envelope shape or the peak location. Once these issues have been resolved, VSI techniques is ready to be applied to dissimilar materials.

3.2 Dispersion of the phase change upon reflection

The phase change upon reflection for normal incident light can be expressed as[9]

$$\phi_0(\nu) = \arctan \left[\frac{2\kappa(\nu)}{1 - \kappa^2(\nu) - n^2(\nu)} \right] \tag{3.2.1}$$

where n and κ are the refractive index and extinction coefficient, respectively, and ν is the wavenumber. Fig. 3.1 shows the phase change upon reflection which differs from π for several materials. The wavenumbers, $\nu = \frac{1}{\lambda}$, are chosen to correspond to the wavelength (λ) of 400 - 700 nm. Fig. 3.1 can be summarized as follows:

1. The phase change of metallic materials has dispersion up to 0.6 radian (35°) in 400-700 nm wavelength region.

2. The dispersion of nonmetallic materials is more than an order of magnitude smaller than metallic materials.

3. The functional form of the phase change upon reflection of metallic materials is simpler than that of nonmetallic materials and can be approximated as a power series of wavenumber ν.

Only metallic materials have non-negligible dispersion, which may affect the coherence envelope of the correlogram.

For the above reasons, metallic materials are the primary interest in the rest of this chapter. For metals Eq.(3.2.1) can be rewritten as

$$\phi_0(\nu) = a_0 + a_1\nu + a_2\nu^2 + a_3\nu^3 + \cdots . \tag{3.2.2}$$

Because the dispersion of the phase change is smaller than 0.6 radian, we can assume $a_1\nu + a_2\nu^2 + a_3\nu^2 + \cdots < 0.6$. In the next section we will examine how this phase dispersion upon reflection affects the coherence envelope for the case, $a_2\nu^2 + a_3\nu^3 + \cdots \ll a_0 + a_1\nu$, exclusively.
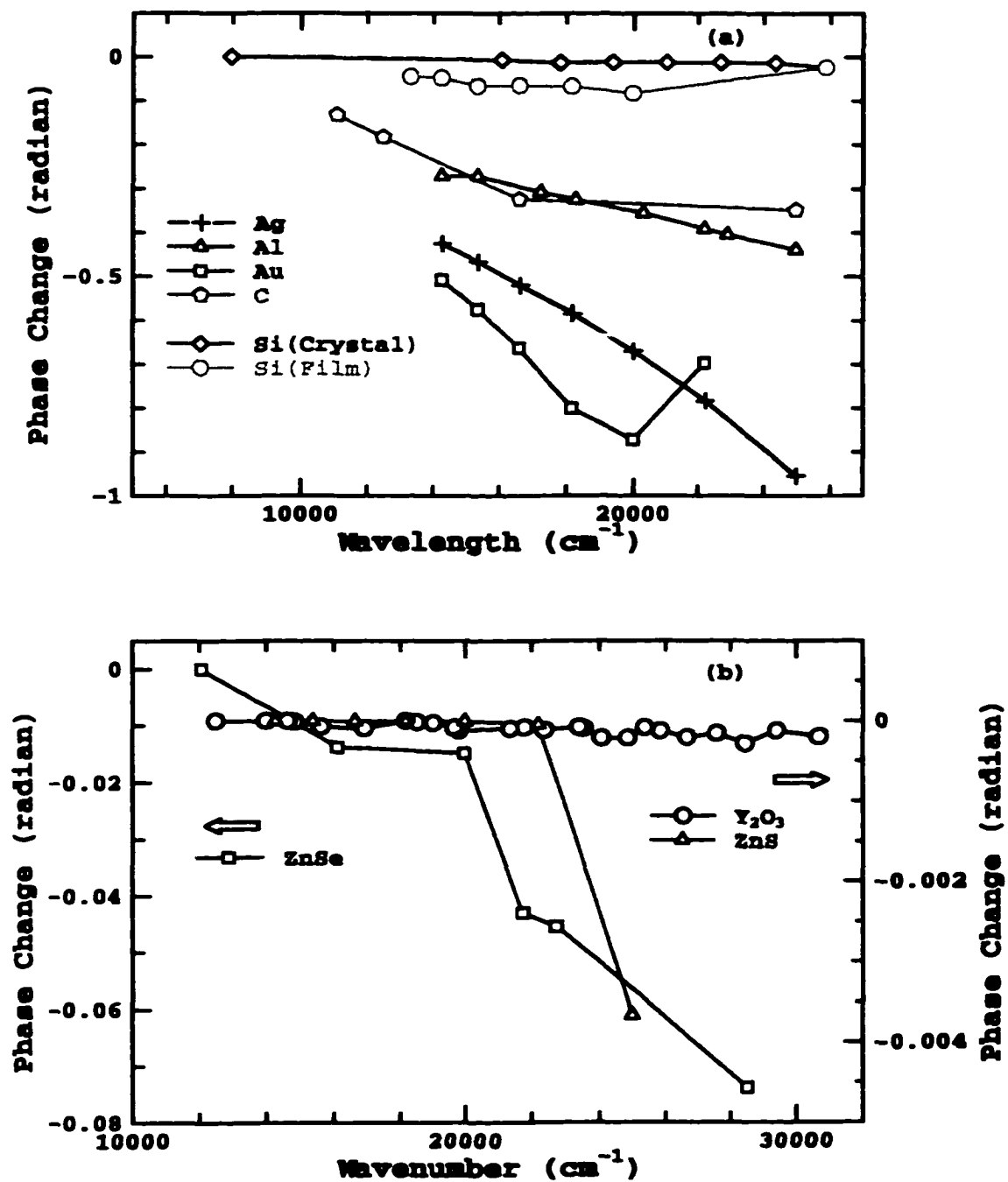
Figure 3.1: **Phase change upon reflection of several metal and nonmetal materials. (a) Metals. (b) Nonmetals.** $ZnSe$ **uses left axis,** ZnS **and** Y_2O_3 **use right axis, as indicated in the figure.**

3.3 Peak location shift of the coherence envelope function

The modulation part of a correlogram with a flat broad-band light distribution $[\nu_1, \nu_2]$:

$$M(z) \propto \int_{\nu_1}^{\nu_2} \cos\left[2\pi\nu 2z + \phi_0(\nu)\right] d\nu. \tag{3.3.1}$$

is the starting point to examine the influence of the phase dispersion on the coherence envelope function. Next Eq. (3.2.2) from the previous section is substituted into Eq. (3.3.1),

$$
\begin{aligned}
M(z) \quad &\propto \quad \int_{-\nu_1}^{\nu_2} \cos\left[2\pi\nu 2z + a_0 + a_1\nu + a_2\nu^2 + a_3\nu^3 + \cdots\right] d\nu \tag{3.3.2}\\
&= \quad \int_{\nu_1}^{\nu_2} \cos\left[2\pi\nu\left(2z + \frac{a_1}{2\pi}\right) + a_0 + a_2\nu^2 + a_3\nu^3 + \cdots\right] d\nu \\
&= \quad Re\left\{\int_{-\nu_1}^{\nu_2} e^{-i\left[2\pi\nu\left(2z+\frac{a_1}{2\pi}\right)+a_0\right]} \times e^{-i\left(a_2\nu^2+a_3\nu^3+\cdots\right)} d\nu\right\}.
\end{aligned}
$$

An approximation must be made for further calculation. From the analysis of phase change dependence on wavenumber ν for several metallic and nonmetallic materials in the previous section, for most cases,

$$a_2\nu^2 + a_3\nu^3 + \cdots \ll a_0 + a_1\nu \ll 2\pi. \tag{3.3.3}$$

is a reasonable assumption. Then the second exponential term in Eq. (3.3.2) is expanded as

$$e^{-i\left(a_2\nu^2+a_3\nu^3+\cdots\right)} = 1 - ia_2\nu^2 - ia_3\nu^3 - \cdots. \tag{3.3.4}$$

Substituting this expression back into Eq. (3.3.2), we have

$$M(z) \propto Re\left\{\int_{-\nu_1}^{\nu_2} e^{-i[2\pi\nu(2z+\frac{a_1}{2\pi})+a_0]} \times (1 - ia_2\nu^2 - ia_3\nu^3 - \cdots)d\nu\right\} \quad (3.3.5)$$

$$= Re\left\{\int_{\nu_1}^{\nu_2} e^{-i[2\pi\nu(2z+\frac{a_1}{2\pi})+a_0]}d\nu\right\}$$

$$- Re\left\{ia_2 \int_{\nu_1}^{\nu_2} \nu^2 e^{-i[2\pi\nu(2z+\frac{a_1}{2\pi})+a_0]}d\nu\right\}$$

$$- Re\left\{ia_3 \int_{\nu_1}^{\nu_2} \nu^3 e^{-i[2\pi\nu(2z+\frac{a_1}{2\pi})+a_0]}d\nu\right\}$$

$$- \cdots\cdots.$$

Here we define some quantities:

$$\bar{\nu} \equiv \frac{\nu_1 + \nu_2}{2}$$

and

$$\Delta\nu \equiv \nu_2 - \nu_1.$$

They correspond to the mean wavenumber and bandwidth of the light source, respectively. Then the equation becomes

$$M(z) \propto Re\left\{\int_{-\infty}^{\infty} rect\left(\frac{\nu - \bar{\nu}}{\Delta\nu}\right) e^{-i[2\pi\nu(2z+\frac{a_1}{2\pi})+a_0]}d\nu\right\} \quad (3.3.6)$$

$$- Re\left\{ia_2 \int_{-\infty}^{\infty} rect\left(\frac{\nu - \bar{\nu}}{\Delta\nu}\right) \nu^2 e^{-i[2\pi\nu(2z+\frac{a_1}{2\pi})+a_0]}d\nu\right\}$$

$$- Re\left\{ia_3 \int_{-\infty}^{\infty} rect\left(\frac{\nu - \bar{\nu}}{\Delta\nu}\right) \nu^3 e^{-i[2\pi\nu(2z+\frac{a_1}{2\pi})+a_0]}d\nu\right\}$$

$$- \cdots\cdots$$

$$= Re\left\{e^{-ia_0} F.T.\left[rect\left(\frac{\nu - \bar{\nu}}{\Delta\nu}\right)\right]\Big|_{\xi=2z+\frac{a_1}{2\pi}}\right\}$$

$$- Re\left\{e^{-ia_0} \frac{ia_2}{(-i2\pi)^2} \frac{d^2}{d^2\xi} F.T.\left[rect\left(\frac{\nu - \bar{\nu}}{\Delta\nu}\right)\right]\Big|_{\xi=2z+\frac{a_1}{2\pi}}\right\}$$

$$- Re\left\{e^{-ia_0} \frac{ia_3}{(-i2\pi)^3} \frac{d^3}{d^3\xi} F.T.\left[rect\left(\frac{\nu - \bar{\nu}}{\Delta\nu}\right)\right]\Big|_{\xi=2z+\frac{a_1}{2\pi}}\right\}$$

$$- \cdots\cdots.$$

The Fourier theory tells us

$$F.T. \left[rect \left(\frac{\nu - \bar{\nu}}{\Delta \nu} \right) \right] = e^{-i2\pi\bar{\nu}\xi} \Delta \nu sinc(\Delta \xi).$$

Substitute this into Eq. (3.3.6) and we have

$$
\begin{aligned}
M(z) \quad \propto \quad & Re \left\{ e^{-ia_0} \left[e^{-i2\pi\bar{\nu}\xi} \Delta \nu \ sinc(\Delta \nu \xi) \right] |_{\xi=2z+\frac{a_1}{2\pi}} \right\} \qquad (3.3.7) \\
- \quad & Re \left\{ e^{-ia_0} \frac{ia_2}{(-i2\pi)^2} \frac{d^2}{d^2\xi} \left[e^{-i2\pi\bar{\nu}\xi} \Delta \nu \ sinc(\Delta \nu \xi) \right] |_{\xi=2z+\frac{a_1}{2\pi}} \right\} \\
- \quad & Re \left\{ e^{-ia_0} \frac{ia_3}{(-i2\pi)^3} \frac{d^3}{d^3\xi} \left[e^{-i2\pi\bar{\nu}\xi} \Delta \nu \ sinc(\Delta \nu \xi) \right] |_{\xi=2z+\frac{a_1}{2\pi}} \right\} \\
- \quad & \cdots\cdots .
\end{aligned}
$$

The derivative operator in Eq. (3.3.7) must be taken care of for further calculation. When applying $\frac{d}{d\xi}$ once to $e^{-i2\pi\bar{\nu}\xi}$, we have $\bar{\nu}$ out. And, applying $\frac{d}{d\xi}$ once to $sinc(\Delta \nu \xi)$, we have $\Delta \nu$ out. Since usually $\Delta \nu \ll \bar{\nu}$ can be assumed, so that the terms with higher order $\Delta \nu$ are dropped from the equation . Then Eq. (3.3.7) can be simplified as

$$
\begin{aligned}
M(z) \quad \propto \quad & Re \left\{ e^{-ia_0} \left[e^{-i2\pi\bar{\nu}\xi} \Delta \nu \ sinc(\Delta \nu \xi) \right] |_{\xi=2z+\frac{a_1}{2\pi}} \right\} \qquad (3.3.8) \\
- \quad & Re \left\{ e^{-ia_0} ia_2 \bar{\nu}^2 \left[e^{-i2\pi\bar{\nu}\xi} \Delta \nu \ sinc(\Delta \nu \xi) \right] |_{\xi=2z+\frac{a_1}{2\pi}} \right\} \\
- \quad & Re \left\{ e^{-ia_0} ia_3 \bar{\nu}^3 \left[e^{-i2\pi\bar{\nu}\xi} \Delta \nu \ sinc(\Delta \nu \xi) \right] |_{\xi=2z+\frac{a_1}{2\pi}} \right\} \\
- \quad & \cdots\cdots \\
= \quad & \Delta \nu \ cos(2\pi\bar{\nu}\xi + a_0) sinc(\Delta \nu \xi)|_{\xi=2z+\frac{a_1}{2\pi}} \\
- \quad & a_2 \bar{\nu}^2 \Delta \nu \ sin(2\pi\bar{\nu}\xi + a_0) sinc(\Delta \nu \xi)|_{\xi=2z+\frac{a_1}{2\pi}} \\
- \quad & a_3 \bar{\nu}^3 \Delta \nu \ sin(2\pi\bar{\nu}\xi + a_0) sinc(\Delta \nu \xi)|_{\xi=2z+\frac{a_1}{2\pi}} \\
- \quad & \cdots\cdots \\
= \quad & \Delta \nu \ sinc(\Delta \nu \xi) \left[cos(2\pi\bar{\nu}\xi + a_0) \right. \\
& \left. -(a_2 \bar{\nu}^2 + a_3 \bar{\nu}^3 + \cdots) sin(2\pi\bar{\nu}\xi + a_0) \right] |_{\xi=2z+\frac{a_1}{2\pi}}.
\end{aligned}
$$

The final expression is

$$M(z) \propto \Delta\nu \; sinc(\Delta\nu\xi)\cos(2\pi\bar{\nu}\xi + a_0 - \alpha)|_{\xi=2z+\frac{a_1}{2\pi}}, \qquad (3.3.9)$$

and the phase α is given by

$$\alpha = \arctan(a_2\bar{\nu}^2 + a_3\bar{\nu}^3 + \cdots) \simeq a_2\bar{\nu}^2 + a_3\bar{\nu}^3 + \cdots . \qquad (3.3.10)$$

The result is quite interesting. It tells us that as long as the dispersion of the phase change upon the reflection has small dependence on the second and higher order of the wavenumber, the shape of the coherence envelope is preserved as there is no dispersion. The linear dependence of the wavenumber ν shifts the location of the coherence envelope peak by an amount of $-\frac{a_1}{4\pi}$, and the constant term and higher order terms only shift the fringes underneath the coherence envelope. S. Suja Helen et al. have observed that the coherence peak envelope position shifted from the zero OPD position about 110 nm without shape deformations in the envelope[37].

Usually coherence-peak-sensing technique is used to profile same-material objects since the shift of different coherence peak location of dissimilar materials will cause height measuring errors. However from the above analysis, technically, if the refractive indices and extinction coefficients of the object being tested are known, the height error might be corrected during the data processing. We have to realize that the surface metrology field is so mature that nm range resolution is required after the height correction. On the other hand, the refractive indices and extinction coefficients are not available to provide this nm height correction for every material. We believe having an experimental correction table for different material pairs is the practical way to deal with height error correction problems for dissimilar materials.

Chapter 4

PHASE-SHIFTING ALGORITHMS

Later in this dissertation we are going to discuss the combined technique of vertical scanning interferometry and phase-shifting interferometry, called here the "PSI on the Fly" technique or white light phase-shifting interferometry (WLPSI). Before the discussion of WLPSI, a brief review of regular or monochromatic phase-shifting interferometry is presented.

4.1 Introduction

Many phase-shifting interferometry (PSI) algorithms were developed in the 1960s and 70s. Since they were developed for either defense or company proprietary projects [2, 29, 49, 60], many important works have not been released to the general public. The earliest reference on the subject seems to be in a paper by Carré[46]. The applications for these early works included optical testing, real-time wavefront sensing for active optics, distance measuring interferometry, and microscopy. When high quality CCDs and small powerful computers became available in the 1980s, PSI techniques started to fully display their power.

In this chapter we are not going to discuss the details of the monochromatic PSI which have already been discussed by many authors and are well-understood.

Instead, the discussion and analysis concentrate on the PSI algorithm chosen for the "PSI on the FLY" method. Therefore, first the Schwider-Haraharan five step PSI algorithm is briefly introduced. Then the discussion moves on to the error analysis of PSI measurement using a white light source, where there are contrast variations between frames. For more detailed discussion on monochromatic PSI, there are two excellent review book chapters (Creath 1988; Greivenkamp and Bruning 1992). Also we strongly recommend Dr. J. C. Wyant's classnotes[61] for his Optical Shop testing course at the University of Arizona for understanding the power and elegance of PSI techniques.

4.2   Concept of PSI

The basic equation for two beam interference is

$$I(x,y) = I_a + I_b \cos \theta(x,y) \tag{4.2.1}$$

or

$$I(x,y) = I_{avarage}[1 + \gamma \cos \theta(x,y)] \tag{4.2.2}$$

and

$$\gamma = \frac{I_b}{I_a} = \frac{AC}{DC}. \tag{4.2.3}$$

The phase $\theta(x,y)$ consists of two terms, a variable $\phi(x,y)$ which depends upon position x and y, and a constant value δ, which is a piston term we have control over. For monochromatic PSI measurement, we can assume the contrast γ is a constant while we shift the phase, i.e. changing δ. But for "PSI on the Fly" type measurement (white light source), the contrast changes between frames and also could cause errors, which is discussed later in this chapter.

The irradiance can be written as

$$I(x,y) = I_{avarage}\{1 + \gamma\cos[\phi(x,y) + \delta]\}. \tag{4.2.4}$$

To have a better understanding of what we want to do, the equation can be rewritten as

$$I(x,y) = a_0 + a_1\cos\delta + a_2\sin\delta \tag{4.2.5}$$

and a_0 through a_2 are defined as follows:

$$a_0 = I_{avarage} \tag{4.2.6}$$

$$a_1 = I_{avarage}\gamma\cos\phi(x,y) \tag{4.2.7}$$

$$a_2 = I_{avarage}\gamma\sin\phi(x,y). \tag{4.2.8}$$

With this notation the phase and the contrast are expressed by the following equations:

$$\tan\phi(x,y) = \frac{a_2}{a_1} \tag{4.2.9}$$

$$\gamma = \frac{\sqrt{a_1^2 + a_2^2}}{a_0}. \tag{4.2.10}$$

These are the two most useful equations in PSI. Up to this point, it is clear that PSI algorithms try to find the unknowns a_0, a_1 and a_2 by varying δ in Eq. (4.2.4). At least three equations are needed for three unknowns.

4.3 Phase-shifting algorithms

In this section the algorithms related to the "PSI on the Fly" method are reviewed. First the very simple four step algorithm is discussed, because the Schwider-Hariharan five frame error compensating algorithm, which is the algorithm used for our measurements, can be derived by weighted coefficients[50] or extended averaging techniques[55] from the four step algorithm.

4.3.1 Four step algorithm

For mathematical simplicity, we start from Eq. (4.2.4). Set δ to take four values of 0, $\frac{\pi}{2}$, $-\pi$ and $\frac{3\pi}{2}$; then we end up with four equations:

$$I_1 = I_{avarage}(1 + \gamma \cos \phi) \tag{4.3.1}$$

$$I_2 = I_{avarage}(1 - \gamma \sin \phi) \tag{4.3.2}$$

$$I_3 = I_{avarage}(1 - \gamma \cos \phi) \tag{4.3.3}$$

$$I_4 = I_{avarage}(1 + \gamma \sin \phi). \tag{4.3.4}$$

It is clear that

$$\tan \phi = \frac{I_4 - I_2}{I_1 - I_3}. \tag{4.3.5}$$

This calculation is performed at each position (x, y), i.e. at every CCD element. The great advantage of this algorithm is that by taking the difference, any fixed pattern noise is eliminated.

In the four step method shown above, the phase difference is changed in discrete steps. For practical reasons it is generally better to vary the phase at a constant rate. Then we can not only reduce effects of ringing in phase shifter and phase shifting

electronics, but also minimize the environmental factors by decreasing the total measurement time. This method is called the integrating bucket technique[60]. The only penalty for allowing the phase difference to vary during the detector integration time is a small reduction in the fringe contrast.

Let Δ be the phase over the integration. Then the signal can be written as

$$I(x,y,\Delta) = \frac{1}{\Delta}\int_{\delta_n-\frac{\Delta}{2}}^{\delta_n+\frac{\Delta}{2}} I_{avarage}(1+\gamma\cos[\phi(x,y)+\delta])d\delta \qquad (4.3.6)$$

$$= I_{avarage}(1+\gamma sinc\left(\frac{\Delta}{2}\right)\cos[\phi(x,y)+\delta_n]). \qquad (4.3.7)$$

The contrast reduces by a factor of $sinc\left(\frac{\Delta}{2}\right)$. Think of the 90° phase step case, $\Delta = \frac{\pi}{2}$; the reduction is about 10% and can be regarded as negligible.

4.3.2 Weighted coefficients

Schwider pointed out that many of the errors, especially errors due to phase shifter miscalibration, occur at twice the frequency of the interference fringes. Therefore, performing the measurement twice with a 90° offset in the phase shift and then averaging the two results having errors 180° out of phase nearly cancels the double frequency error. In reality, we do not have to actually perform the measurement twice: as long as the phase step is 90° all we have to do is to add one more frame of data, use frames 1 through M for the first calculation and frames 2 through M+1 for the second calculation, and average the two results. The result has greatly reduced error due to phase shifter calibration.

The above approach for averaging two 90° offset phase measurements was well known before Schwider's paper. He went one step further. Schwider showed that rather than averaging the calculated phase after the arctangent was performed, the numerators and the denominators of the arctangent function could be averaged.

Given a phase algorithm for M frames separated by 90° in the following form.

$$\tan \phi_M = \frac{N}{D} \qquad (4.3.8)$$

$$\gamma_M = \frac{\sqrt{N^2 + D^2}}{I_{average}} = \frac{AC\{V\}}{DC\{V\}}, \qquad (4.3.9)$$

to calculate a new algorithm for M+1 frames, an N and D can be calculated for the first M frames and the other set of N and D can be calculated for the 2 to M+1 frames. A new M+1 frames algorithm is given by

$$\tan \phi_{M+1} = \frac{N_1 + N_2}{D_1 + D_2} = \frac{N'}{D'} \qquad (4.3.10)$$

$$AC\{V\} = \sqrt{N'^2 + D'^2}. \qquad (4.3.11)$$

This technique can be extended to as many frames as desired. In the next section we will show that the Schwider-Hariharan algorithm can be derived by this weighted coefficients method from the simple four step algorithm.

4.3.3 Schwider-Hariharan algorithm

The Schwider-Hariharan algorithm is a five step algorithm which is insensitive to phase shifter calibration errors. The algorithm assumes a linear phase shift of α between frames:

$$\delta_i = -2\alpha, \; -\alpha, \; 0, \; \alpha, \; 2\alpha; \qquad i = 1, 2, 3, 4, 5. \qquad (4.3.12)$$

Then the intensity of each frame can be expressed as

$$I_1(x,y) = I'(x,y) + I''(x,y)\cos[\phi(x,y) - 2\alpha] \qquad (4.3.13)$$

$$I_2(x,y) = I'(x,y) + I''(x,y)\cos[\phi(x,y) - \alpha] \qquad (4.3.14)$$

$$I_3(x,y) = I'(x,y) + I''(x,y)\cos[\phi(x,y)] \qquad (4.3.15)$$

$$I_4(x,y) = I'(x,y) + I''(x,y)\cos[\phi(x,y) + \alpha] \qquad (4.3.16)$$

$$I_5(x,y) = I'(x,y) + I''(x,y)\cos[\phi(x,y) + 2\alpha]. \qquad (4.3.17)$$

By solving these equations, the intermediate result is

$$\frac{\tan[\phi(x,y)]}{2\sin\alpha} = \frac{I_2 - I_4}{2I_3 - I_5 - I_1}. \qquad (4.3.18)$$

And further simplification leads to

$$\sin^2\alpha = \frac{4(I_2 - I_4)^2 - (I_1 - I_5)^2}{-I_1 + 2I_3 - I_5}, \qquad (4.3.19)$$

and the contrast is

$$I'\gamma = \frac{(I_2 - I_4)^2\sqrt{[4(I_2 - I_4)^2 - (I_1 - I_5)^2] + (-I_1 + 2I_3 - I_5)^2}}{4(I_2 - I_4)^2 + (I_1 - I_5)^2}. \qquad (4.3.20)$$

The phase step α is still arbitrary. The step which minimizes the variation in errors in the phase shift will be explored as following. Differentiating Eq. (4.3.18) with respect to α, we get

$$\frac{d}{d\alpha}\left\{\frac{\tan[\phi(x,y)]}{2\sin\alpha}\right\} = \frac{-\cos\alpha\tan[\phi(x.y)]}{2\sin^2\alpha}, \qquad (4.3.21)$$

which becomes zero when $\alpha = \frac{\pi}{2}$ and $\alpha = \frac{3\pi}{2}$. Fig. 4.1 shows Eq. (4.3.18) for the case when $\phi(x,y) = \frac{\pi}{4}$. When these values are used for the phase shift, Eq. (4.3.18) becomes insensitive to the phase shift calibration errors. The phase and contrast can
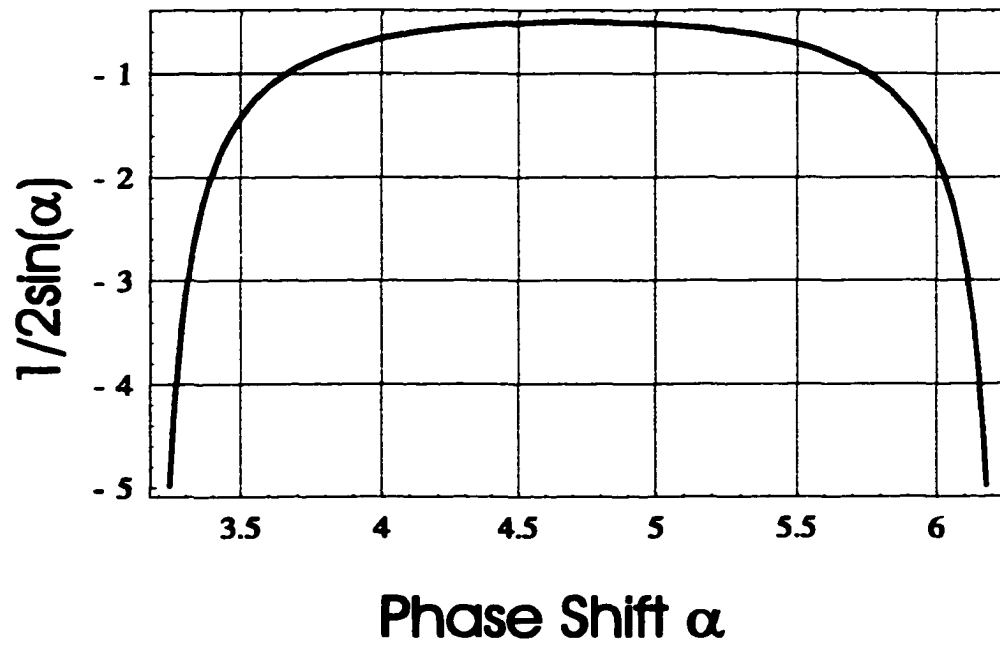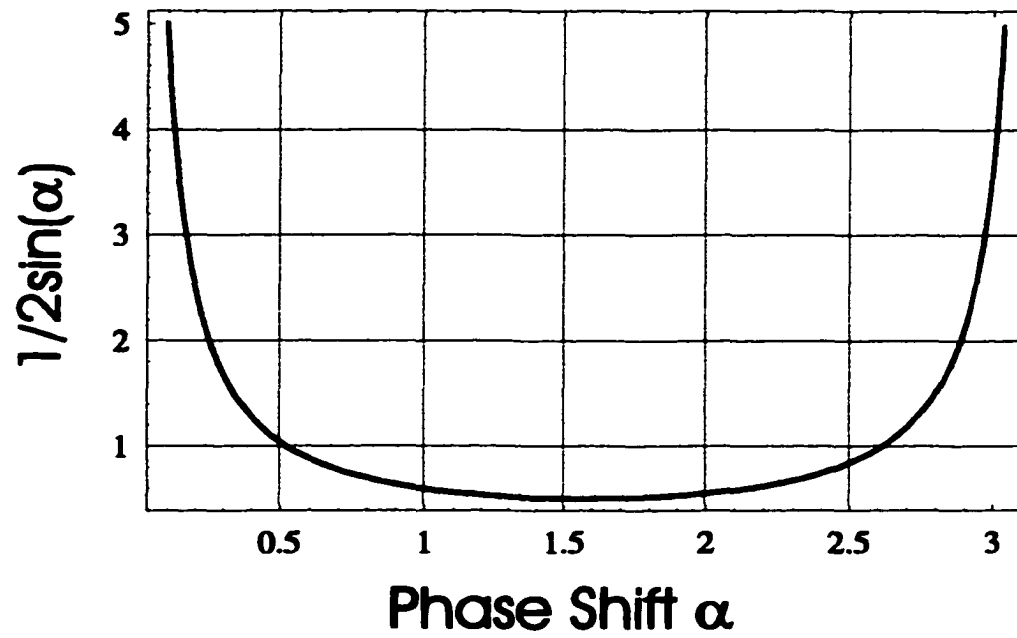
Figure 4.1: **A plot of Eq.(4.3.18) as a function of the value of the phase shift.**

be simplified to

$$\phi(x,y) = \arctan\left[\frac{\pm 2(I_2 - I_4)}{2I_3 - I_5 - I_1}\right] \qquad (4.3.22)$$

$$\gamma = \frac{3\sqrt{4(I_4 - I_2)^2 + (I_1 + I_5 - 2I_3)^2}}{2(I_1 + I_2 + 2I_3 + I_4 + I_5)} \qquad (4.3.23)$$

where the plus sign is for the $\frac{\pi}{2}$ phase shift and the minus sign is for $\frac{3\pi}{2}$.

The extremes in the plot of Eq. (4.3.18) are centered at $\frac{\pi}{2}$ and $\frac{3\pi}{2}$ and are quite broad. As a results, the Schwider-Hariharan algorithm can tolerate fairly large errors in the phase shift before significant errors appear in the calculated phase[6] in the wavefront. If the actual phase shift between measurements is $\frac{\pi}{2} + \varepsilon$, then there is a corresponding measured phase $\phi'(x,y) = \phi(x,y) + \Delta\phi(x,y)$. Assuming here ε is small, then the measured phase error can be approximated using Eq. (4.3.18):

$$\frac{\tan\phi'(x,y)}{2\sin\left(\frac{\pi}{2} + \varepsilon\right)} = \frac{\tan\phi(x,y) + \frac{\Delta\phi(x,y)}{\cos^2\phi(x,y)} + \cdots}{2\left[\sin\frac{\pi}{2} - \frac{1}{2}\varepsilon^2 + \cdot\right]} \qquad (4.3.24)$$

$$\cong \left(1 + \frac{\varepsilon^2}{2}\right)\tan\phi(x,y).$$

The error in the measurement of the phase can also be easily determined:

$$\tan\phi'(x,y) = \tan\phi(x,y) + \frac{\Delta\phi(x,y)}{\cos^2(x,y)} + \cdot$$

$$\cong \left(1 + \frac{\varepsilon^2}{2}\right)\tan\phi(x,y).$$

And we get

$$\Delta\phi(x,y) = \phi'(x,y) - \phi(x,y) \cong \frac{\varepsilon^2}{4}\sin[2\phi(x,y)]. \qquad (4.3.25)$$

Fig. 4.2 shows the phase error due to a 2° phase-shifting calibration error. The error is fairly small compared to three or four step algorithms.

Next shows that the Schwider-Hariharan algorithm is derived by the weighted coefficients method from the four step algorithm. The phase calculated by the four
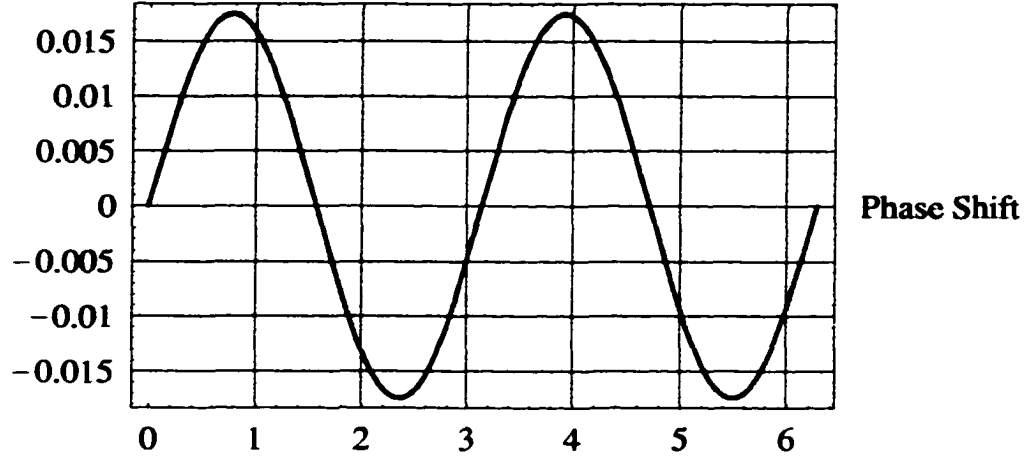
Figure 4.2: **Phase error of 2° phase-shifting error in calibration. The peak to valley error is about 0.04°.**

step algorithm is

$$\tan \phi(x,y) = \frac{-I_2 + I_4}{I_1 - I_3},$$

(4.3.26)

so the N and D for the averaging are

$$N_1 = -I_2 + I_4$$

(4.3.27)

$$D_1 = I_1 - I_3.$$

(4.3.28)

Likewise, when we take another frame,

$$N_2 = -I_3 + I_5$$

(4.3.29)

$$D_2 = I_2 - I_4,$$

(4.3.30)

and average denominators and numerators before taking arctangent, we arrive at exactly the form of the Schwider-Hariharan algorithm. The process can be iterated

as much as necessary, and the phase errors due to various noise sources decrease as adding more and more frames.

4.4 White light phase-shifting error analysis

When using a white light source to pursue PSI measurement, the contrast of interferograms is no longer a constant. The contrast varies as we shift the phase between test beam and reference beam. Therefore the monochromatic PSI algorithm may produce errors. In this section errors due to the contrast change from a white light source is analyzed. The Schwider-Hariharan algorithm is adopted for the "PSI on the Fly" algorithm so that the error analysis is done for this particular algorithm only. In later chapter the PSI on the Fly algorithm will be discussed. We choose here a numerical method to simulate the phase measuring errors from the encoded phase. First we generate a correlogram for an 8 bit system with the maximum modulation contrast of 1, and the total scan length of 127Δ, with the coherence function located at position 64Δ:

$$g(n) = INT\left(2^7 + 2^7 \exp\left\{-\frac{[(n-64)\Delta]^2}{\sigma^2}\right\} \cos\left[\frac{4\pi}{\lambda}(n-64)\Delta + \phi_0\right]\right) \quad (4.4.1)$$

where the mean wavelength $\bar{\lambda}$ = 600 nm, and the scanning step Δ is $\frac{\bar{\lambda}}{8}$ for 90° and $\frac{3\bar{\lambda}}{8}$ for the 270° phase shift. The parameter σ is set at 500 nm, such that the coherence length of the correlogram is about 1.2 microns as in our Mirau interference microscope. Fig. 4.3 shows the generated correlogram and its recovered modulation contrast using Eq. (4.3.22) when setting the phase ϕ_0 of the zero OPD position as $\frac{\pi}{10}$. Fig. 4.4 shows the correlogram, modulation contrast, measured phase and its phase error from the encoded phase for the positions with significant modulation contrast.

Figure 4.3: **The generated correlogram from Eq.(4.4.1) and its recovered modulation contrast calculated using the Schwider-Hariharan algorithm for 90° phase shift.**

Figure 4.4: (a) The generated correlogram from Eq. (4.4.1) at the position with significant contrast for 90° phase step. (b) its modulation contrast extracted using the Schwider-Hariharan algorithm. (c) The measured phase calculated using the Schwider-Hariharan algorithm. (d) The measured phase error from the encoded phase.

The phase error at the maximum contrast position is -5 mrad which corresponds to 4×10^{-5} wavelength of height error. From Fig. 4.4, we see a trend of increasing phase errors when the phase is measured from the maximum contrast position. The result is quite normal since the contrast variation is minimum at the maximum contrast position. Thus the condition is close to the monochromatic phase shifting.

Next we vary the phase value ϕ_0 of the zero OPD and see how the error changes at scanning positions relatively close to the zero OPD position. Fig. 4.5 shows the phase error as a function of ϕ_0 at positions of $n=61$, 62, 63, 64, 65, 66 and 67. Since the modulation contrast is symmetric around the zero OPD position and the Schwider-Hariharan algorithm is symmetric around the center position, the phase error functions have the same shape at the position $n = 64 \pm \Delta n$, where Δn is an integer. The peak-to-valley phase error at zero OPD position ($n=64$) is 23 mrad ($\frac{1}{500}\lambda$ height error), which is much less than the error caused by other error sources like vibration, phase shift calibration error, detector nonlinearity etc.

The same analysis can be applied to the 270° phase-shift case. We have less freedom in choosing the position to measure the phase since the contrast changes more rapidly from one frame to the other. The next three figures (Fig. 4.6 - Fig.4.8) show the simulated correlogram for a 270° phase step, the measured phase using the Schwider-Hariharan algorithm, and the error from the encoded phase, as well as the error trend as a function of phase ϕ_0 of the zero OPD position. Fig. 4.8 shows that when using a 270° phase shift which saves the measurement time by a factor of three, the measured peak-to-valley phase error at the zero OPD position due to contrast variation is about 80 mrad. This corresponds to $\frac{\lambda}{200}$ height error, whereas the monochromatic PSI reduces the height error to $\frac{\lambda}{1000}$ at the best calibration condition. While the 270° phase shift produces considerable error, it may be acceptable for some
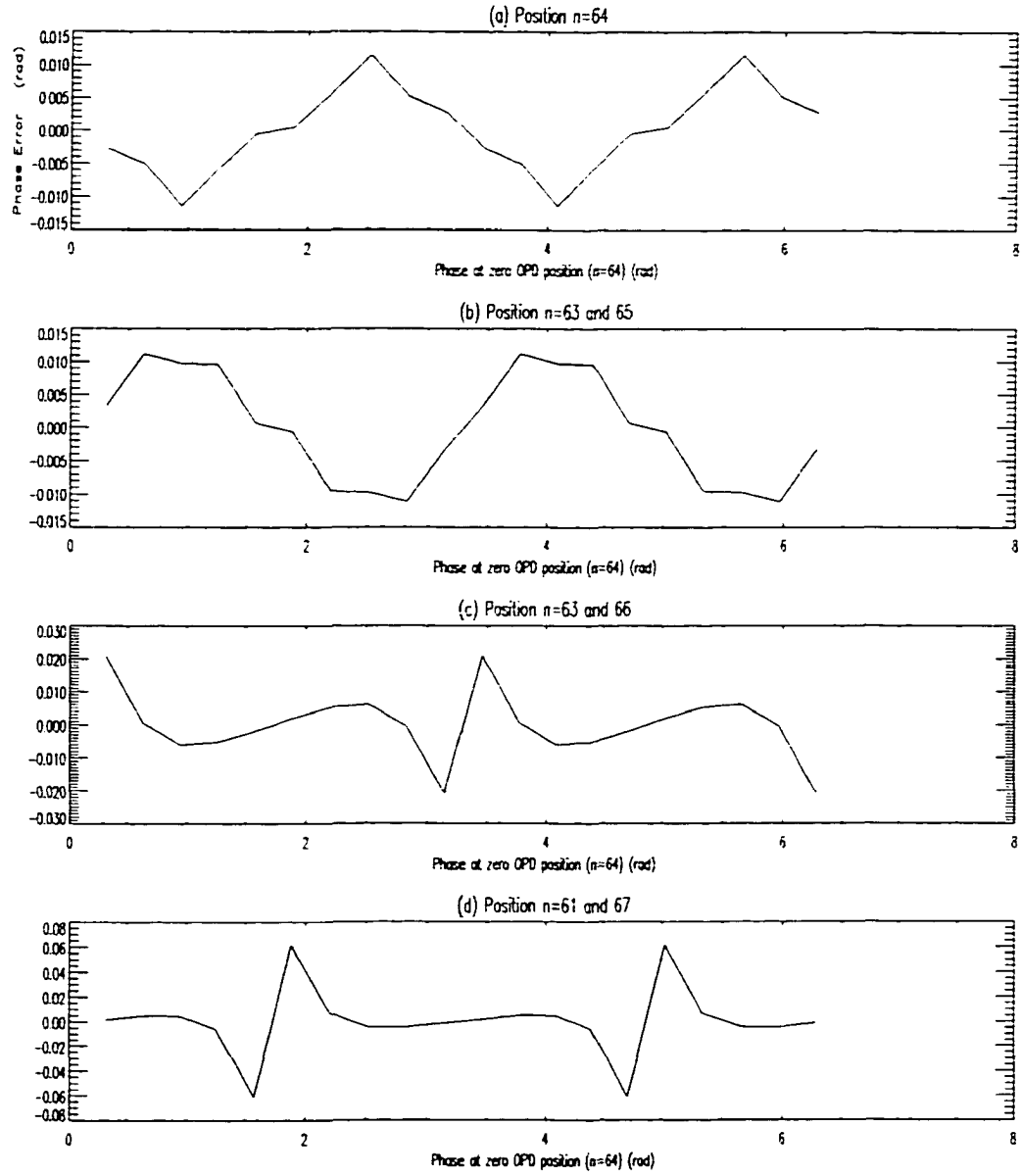
Figure 4.5: **Phase error as a function of phase ϕ_0 of the zero OPD position for 90° phase shifting. (a) at n=64, which is the zero OPD position. (b) at n=63 and 65. (c) at n=62 and 66 and (d) at n=62 and 67.**
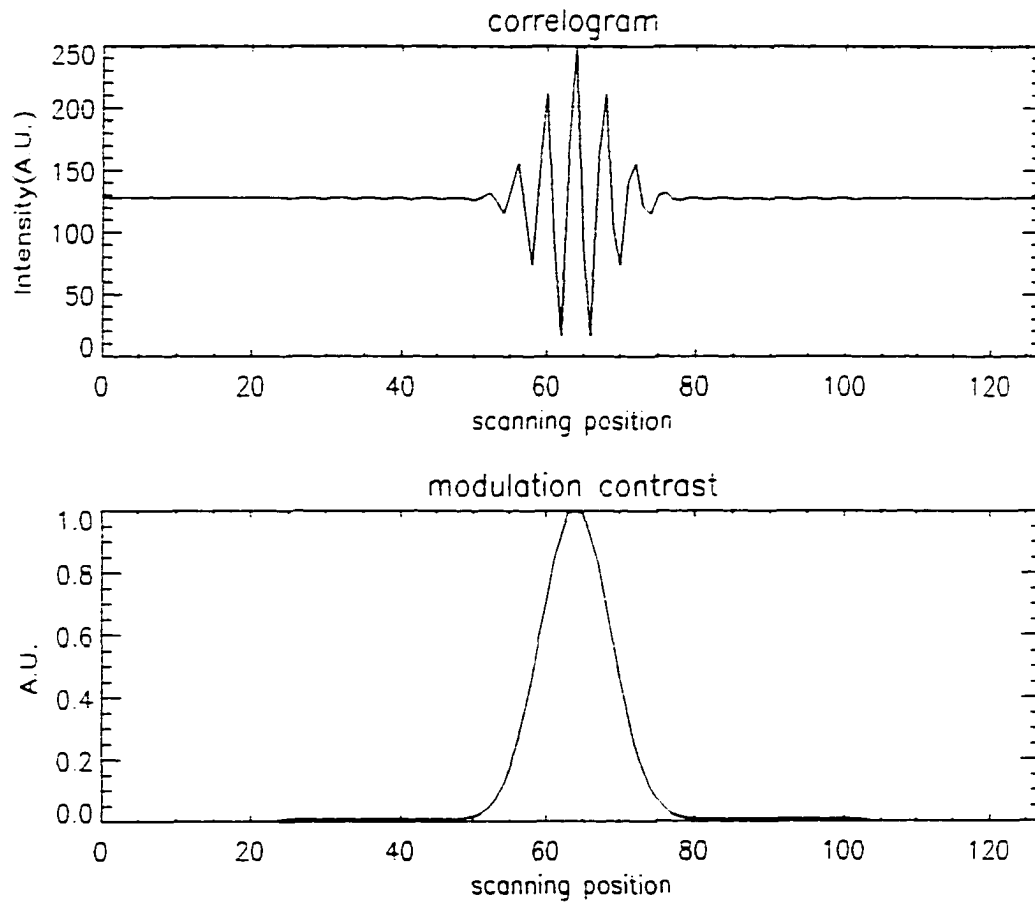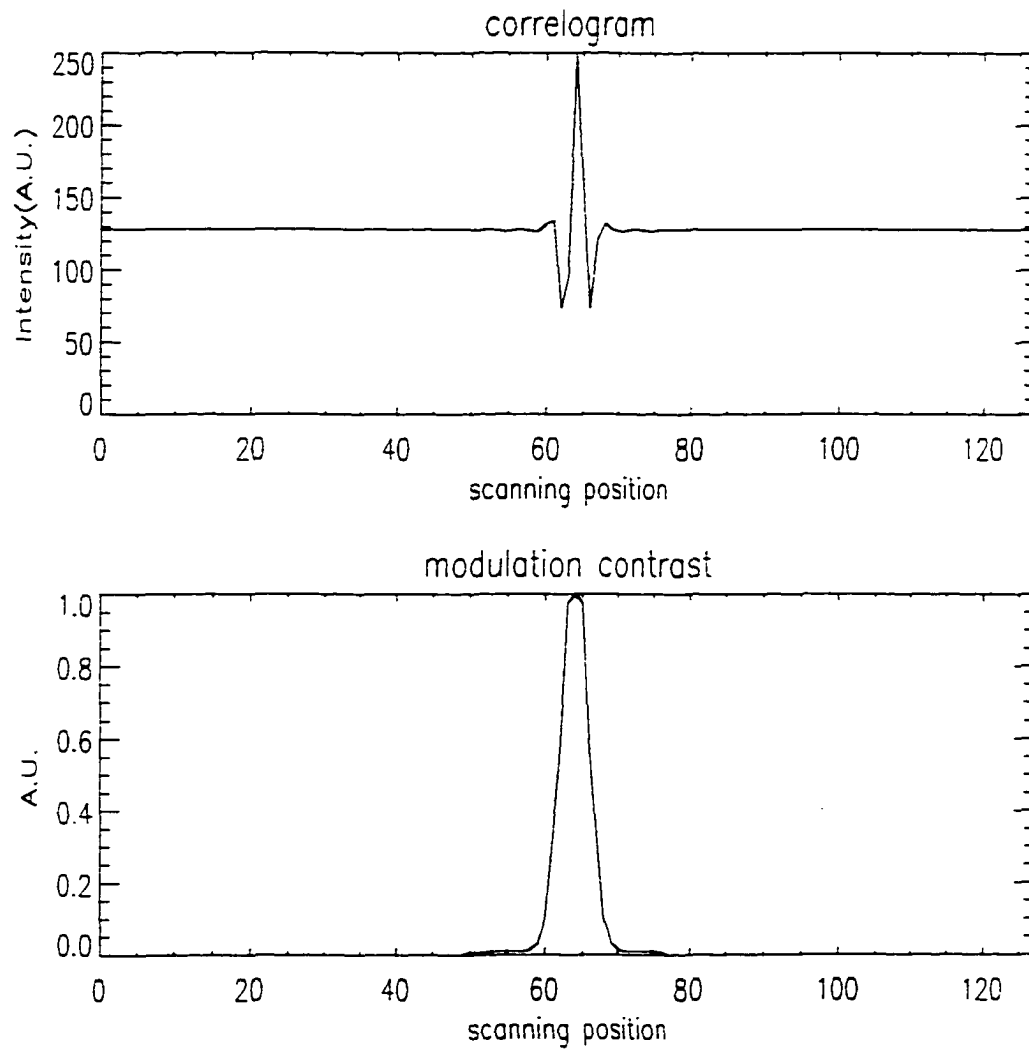
Figure 4.6: **A generated correlogram from Eq. (4.4.1) and its recovered modulation contrast calculated using the Schwider-Hariharan algorithm for 270° phase shift.**
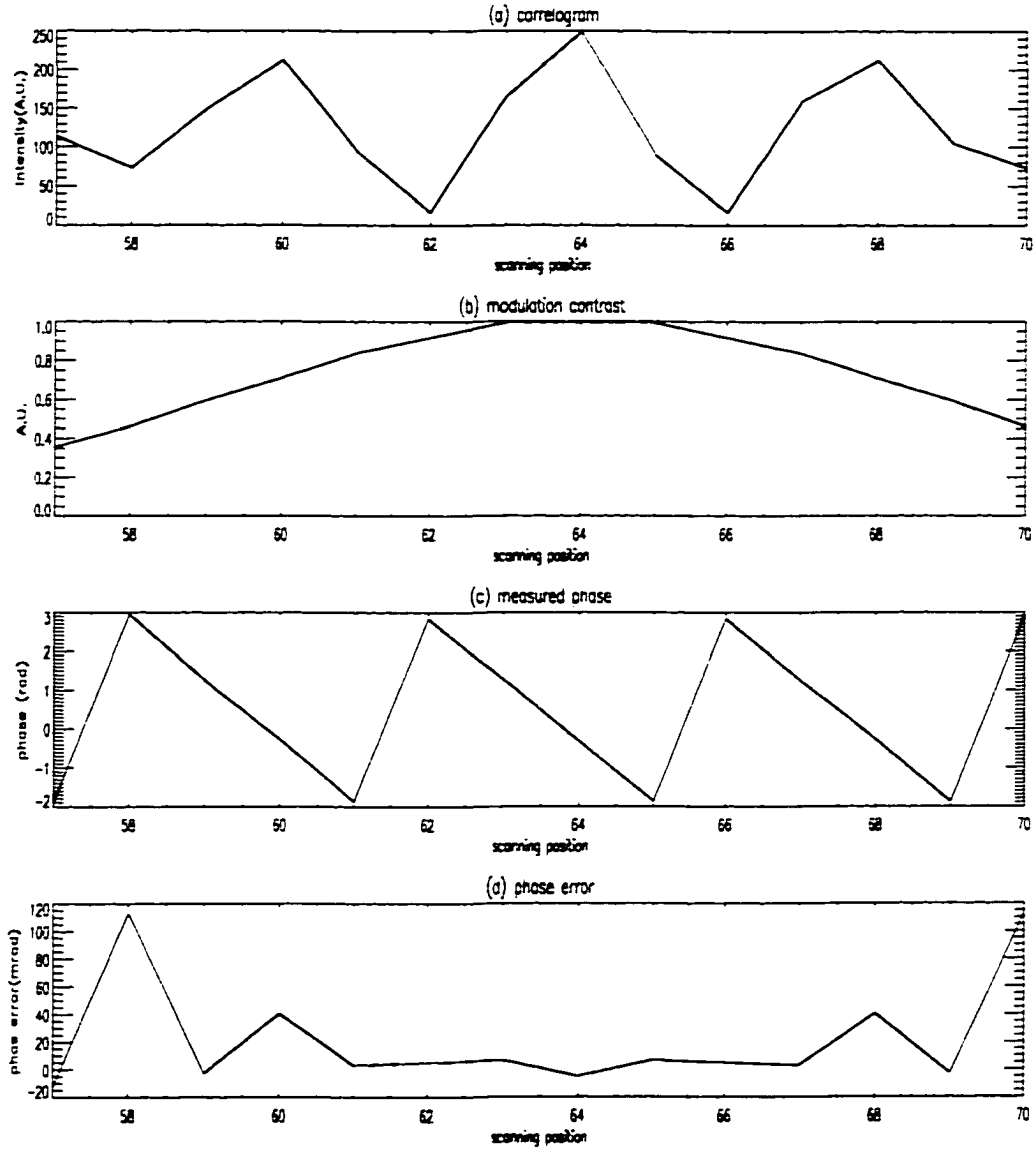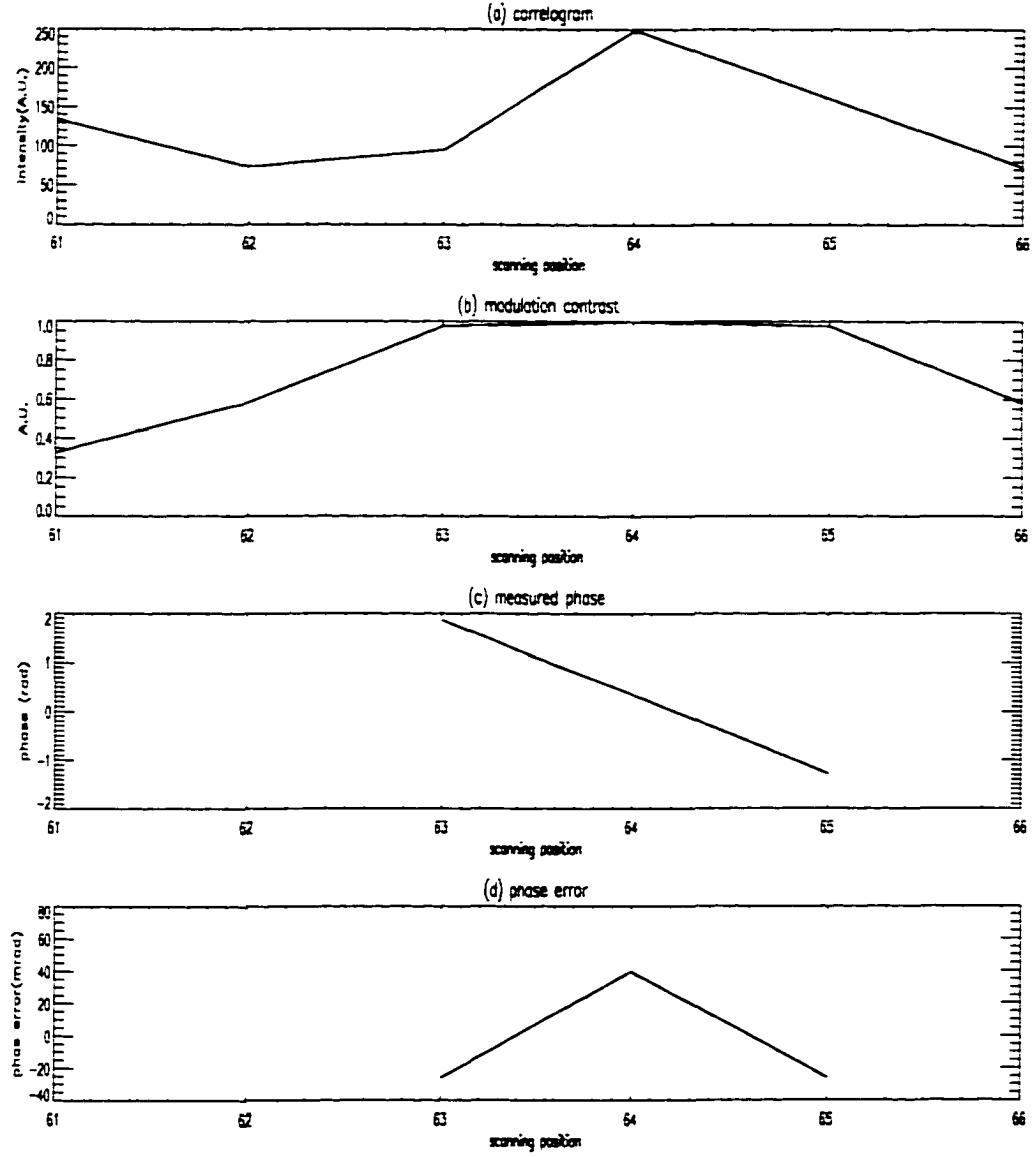
Figure 4.7: (a) A generated correlogram from Eq. (4.4.1) at the position with significant contrast for 270° phase step. (b) its modulation contrast extracted using the Schwider-Hariharan algorithm. (c) The measured phase calculated using the Schwider-Hariharan algorithm. (d) The phase error from the encoded phase.
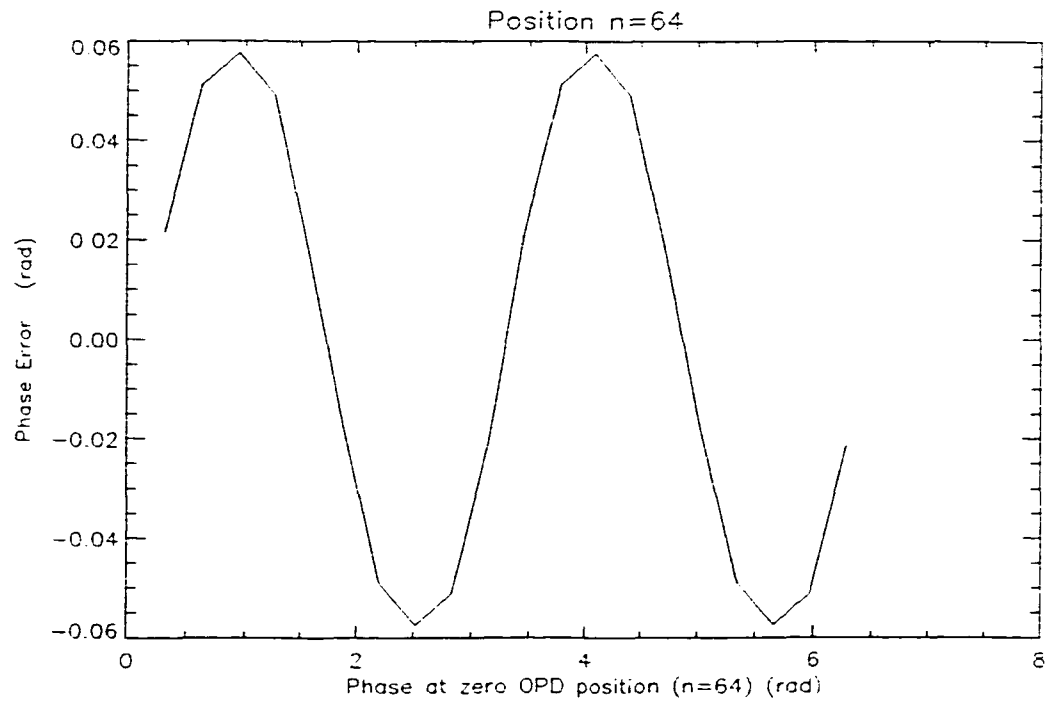
Figure 4.8: **Phase error as a function of phase ϕ_0 of the zero OPD position for 270° phase step. The phase is measured at the zero OPD position ($n=64$).**

applications because of the great reduction of measurement time.

4.5 Conclusion

One important finding from the error analysis in this chapter is that to avoid unnecessary phase errors the fractional phase should be measured from the maximum contrast position of the correlogram. Thus if combining the VSI with the PSI technique for the improvement of height resolution, the WLI algorithm discussed in Section 2.4 is expected to achieve a higher resolution than the centroid type approach.

Chapter 5

BAT WINGS ARTIFACT AND ITS MECHANISM

This chapter describes an interference fringe modulation skewing effect in white light vertical scanning interferometry that can produce a "bat wings" artifact in a step height measurement. The skewing occurs at the position on or close to the edge of a step in the sample under measurement, when the step height is less than the coherence length of the light source used. A diffraction model is used to explain the effect.

5.1 Introduction

One method of determining surface height involves the use of a broad-spectral-width light source in an interferometer and measuring the degree of modulation contrast as a function of path difference[7, 12, 15, 19, 22, 23, 26, 34, 35, 36, 39, 48, 52, 54, 63]. Due to the large spectral bandwidth of the source, the coherence length of the source is short so that good contrast fringes will be obtained only when the two paths of

the interferometer are closely matched in length. By looking at the sample posi-
tion for which the fringe contrast is a maximum while the optical path difference
(OPD) is varied, the height variations across the sample can be determined. In
this measurement there are no height ambiguities or focus errors since the interfer-
ometer is adjusted so that the sample is in focus when the OPD is zero. Many
excellent features of white light vertical scanning interferometry have previously been
published[7, 12, 15, 19, 22, 23, 26, 34, 35, 36, 39, 48, 52, 54, 63]. While this is a very
useful technique for measuring many surfaces, it does not work especially well with
step heights[30] less than the coherence length of the light source in use.

The problem has been known as "bat wings" because of the shape of the false
information. To our best knowledge, bat wings appear for every well-established
white light vertical scanning technique, as shown in Fig. 5.1. We would like to
explain the exact nature of bat wings in the next section and discuss the artifact
from the coherence envelop skewing in correlograms which is the interference intensity
distribution along the vertical scanning direction. In Section 5.3 a diffraction model
to explain this effect is proposed.

5.2 Bat wings

The surface profiles of 80 nm, 460 nm and 1.7 microns step height standard (VLSI
Standards Inc.) measured with white light vertical scanning techniques is shown in
Fig. 5.2. The light source used in the measurement has a coherence length of 1.2
microns. Bat wings clearly appear in profiles of the 80 nm and 460 nm step height
standards, but not in the 1.7 microns step height standard whose step height exceeds
the coherence length of the light source. The top portion close to the edge of the step
discontinuity, whose height is less than the coherence length, always appears higher
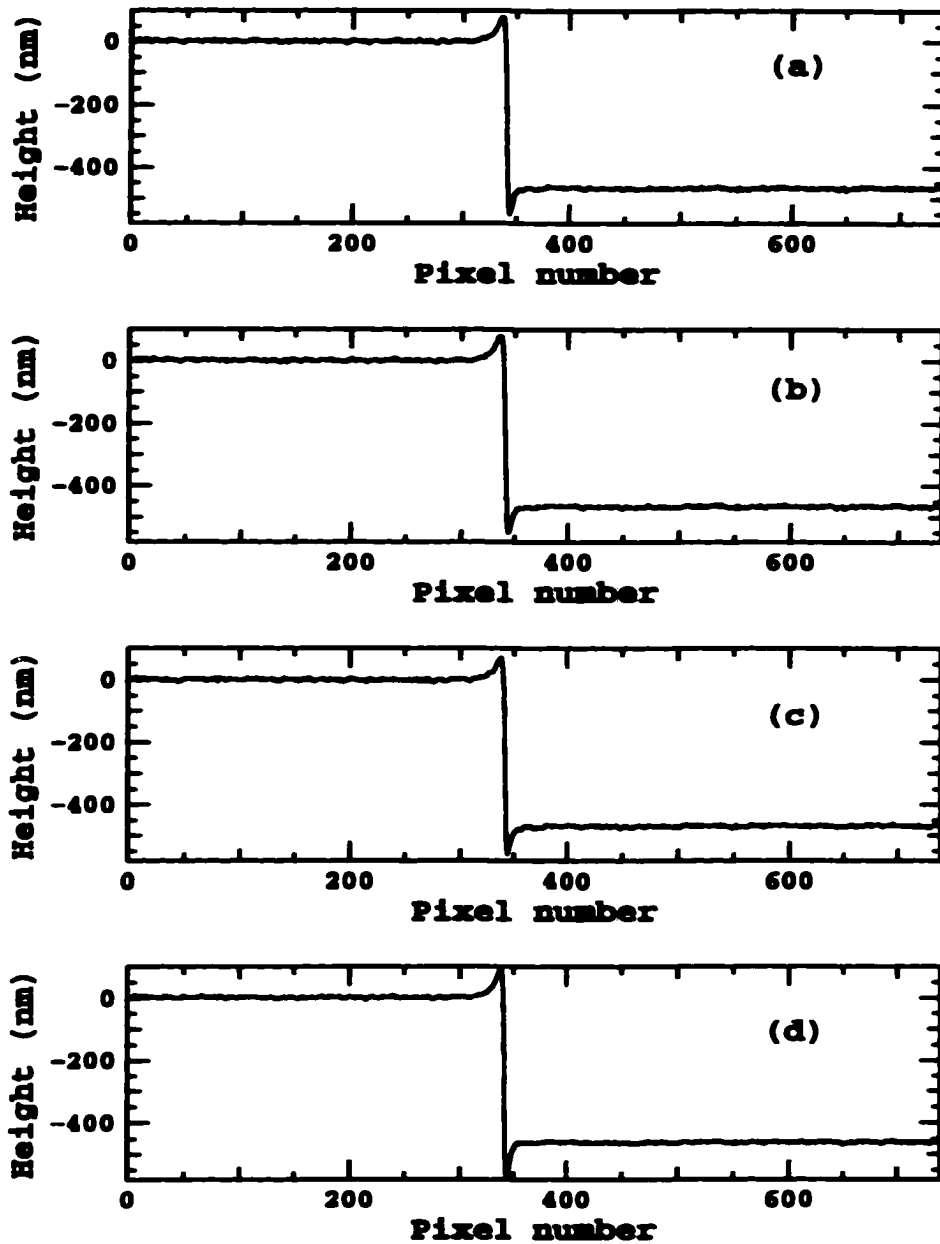
Figure 5.1: **The processed surface profiles of the 460 nm height standard** ($VLSI$, $SHS4600\text{Å}$). **(a) by the centroid algorithm (Section 2.6), (b) from the centroid of the recovered modulation contrast by Fourier transform algorithm (Section 2.2), (c) from the centroid of the recovered modulation contrast by Hilbert transform algorithm (Section 2.3), (d) from the phase slope in Fourier domain (Section 2.7).**
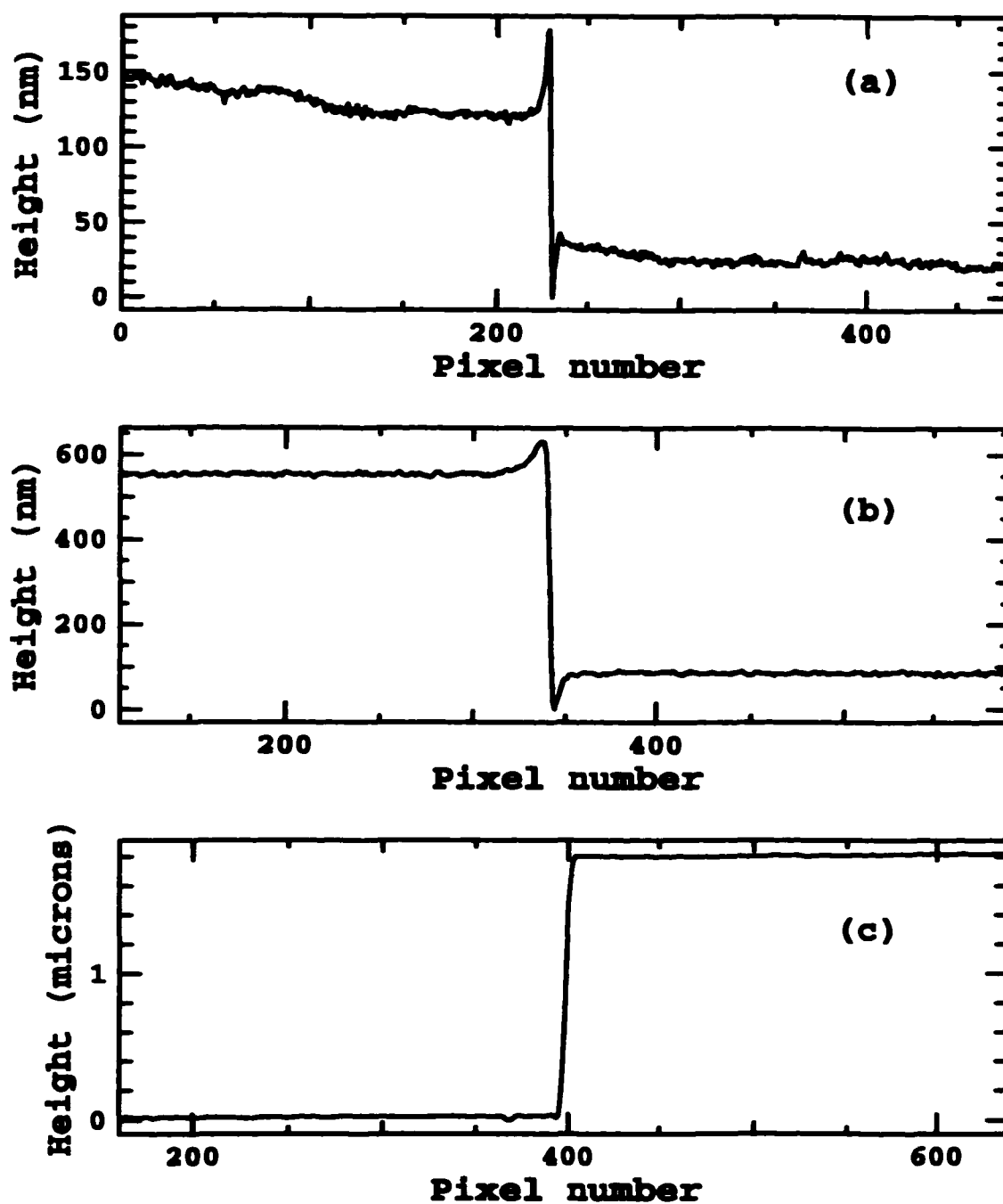
Figure 5.2: **The measured profile of (a) 80 nm step height standard, (b) 460 nm step height standard and (c) 1.7 micron step height standard using a Mirau interference microscope, shown in Fig. 6.4.**
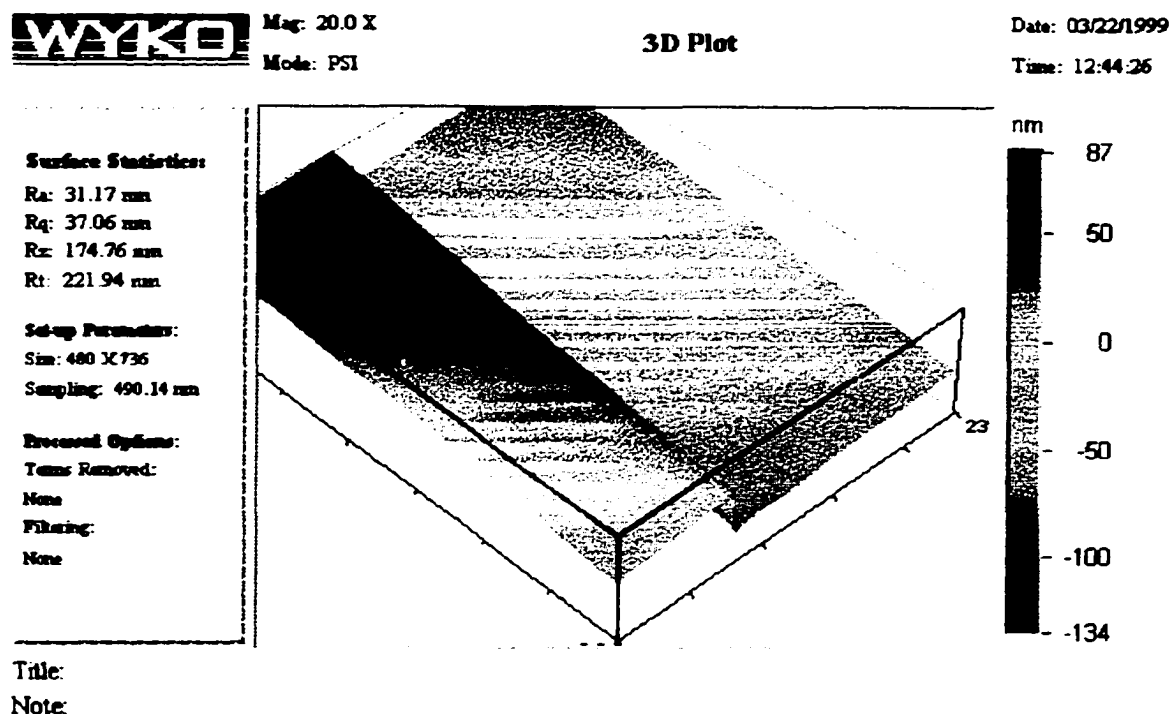
Figure 5.3: **The measured profile of 80 nm step height standard by phase shifting technique with a Mirau microscope shown in Fig. 6.4.**

and the bottom portion appears lower than they actually are. From Fig. 5.2 it is clear that the false information is named bat wings because of its appearance. The 80 nm height standard can also be measured with phase-shifting interferometry (PSI). In that case the false information does not appear. PSI measurement on the 80 nm height standard is shown in Fig. 5.3. The result suggests that the false information has more effect on intensity than phase which might give us a clue to solving the problem[30]. Table 5.1 summarizes the results obtained from careful measurements[44] on gratings of different periods and depths. The first two rows in the table tell us that the bat wings artifact appears only when the coherence length of the light source is larger than the step discontinuity. The third and fourth parameters are essentially the

Table 5.1: The influences of measurement parameters on bat wings.

Parameter	Discription
Wavelength	shorter $\rightarrow$ narrow the width of the bat wings
Grating depth	very strong up to several hundred nanometers; not much when larger than 1 micron
Objective magnification	higher magnification $\rightarrow$ more bat wings
Numerical aperture (N.A.)	larger N.A. $\rightarrow$ more bat wings
Data points	containing many defocus frames $\rightarrow$ the height of bat wings increases
Grating period	short period $\rightarrow$ the height of bat wings increases

The profile is calculated by locating the centroid of correlogram[5].

same, since the higher magnification interference-microscope objective has a larger numerical aperture (N.A.). The N.A. of the objective determines the cutoff spatial frequency of the system. As shown in Fig. 5.2, the bat wings contain high spatial components so that high N.A. permits large bat wings. The next parameter, the number of data points along the vertical scan, changes the bat wings effect, strongly suggesting to examine the correlogram which might deform at the positions having bat wings. The result that a short grating period increases the height of bat wings can be explained from signal-to-noise ratio (SNR). It is expected that more light is trapped in the grating wells when the period is reduced and depth remains same. Anything happening on or near the step edges which provides false information enhances the effects when the signal light carrying the information decreases.

The surface height information is retrieved from the modulation contrast of the correlograms. The correlograms at the positions of bat wings would give us good insight about the phenomenon. Fig. 5.4 - Fig. 5.6 show the correlograms for the 80 nm, 460 nm and 1.7 micron step height standard along a line across the step discontinuity. Figures, (a) and (j) show correlograms of positions far from the step edge either on the top side or the bottom side. The pixel numbers above the correlograms of each step standard correspond to the pixel number in Fig. 5.2. First we notice the fringe contrast reduction at the positions on or close to the step edge due to the decrease of the light reflected back to the system from the sample surface. The integrating energy distributions across the step standards are shown in Fig. 5.7 to illustrate the effect. The light coming back to the system decreases as the step height increases. The contrast reduction from the decrease of test beam intensity results in poor SNR, but it does not directly cause bat wings since the bat wings effect does not appear in the measured surface profile of 1.7 micron step height standard which suffers from
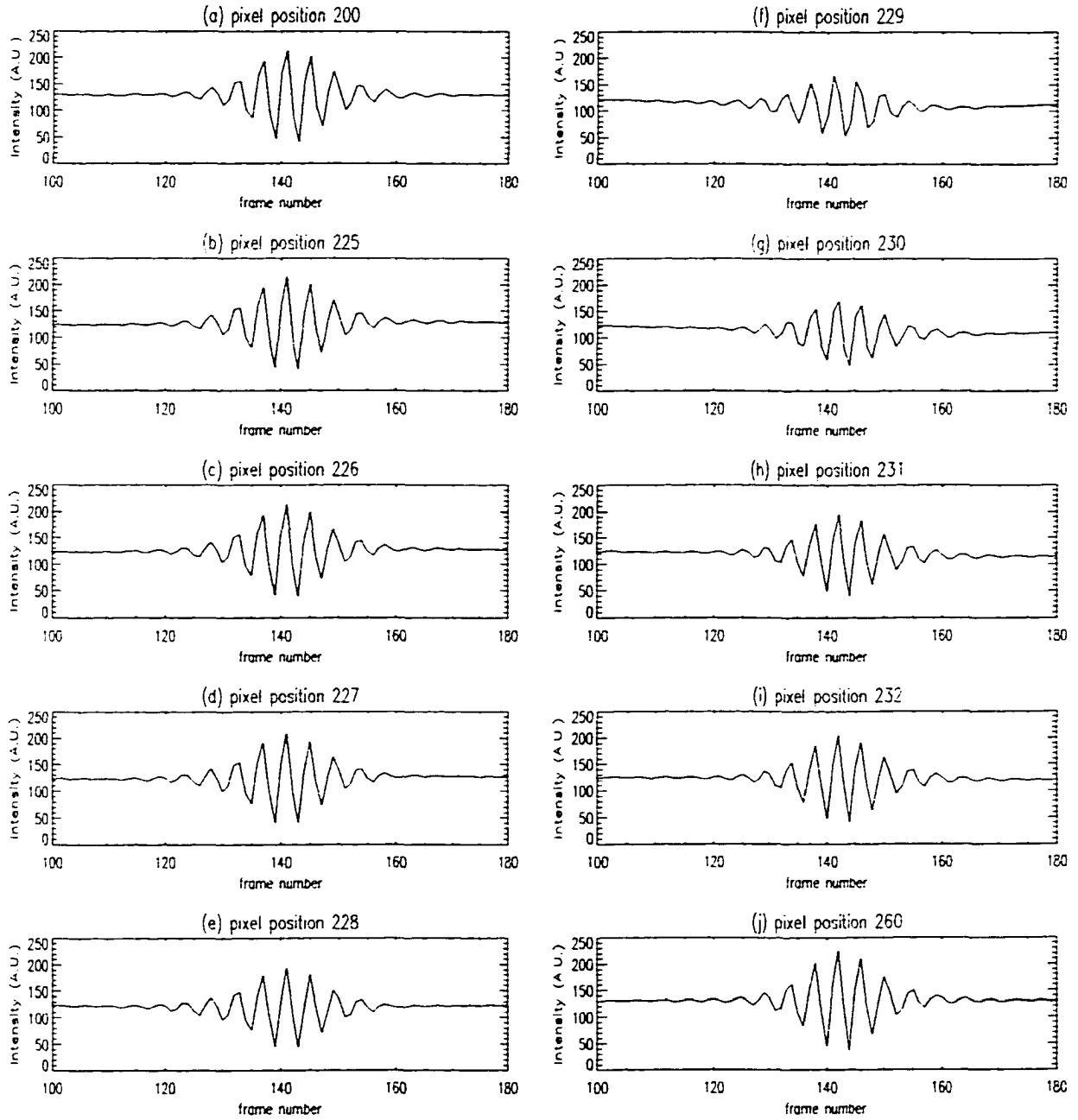
Figure 5.4: **The correlograms of 80 nm height standard across the step discontinuity. (a) far from the edge on the top side. (b) to (i) close to the edge. (j) far from the edge on the bottom side.**
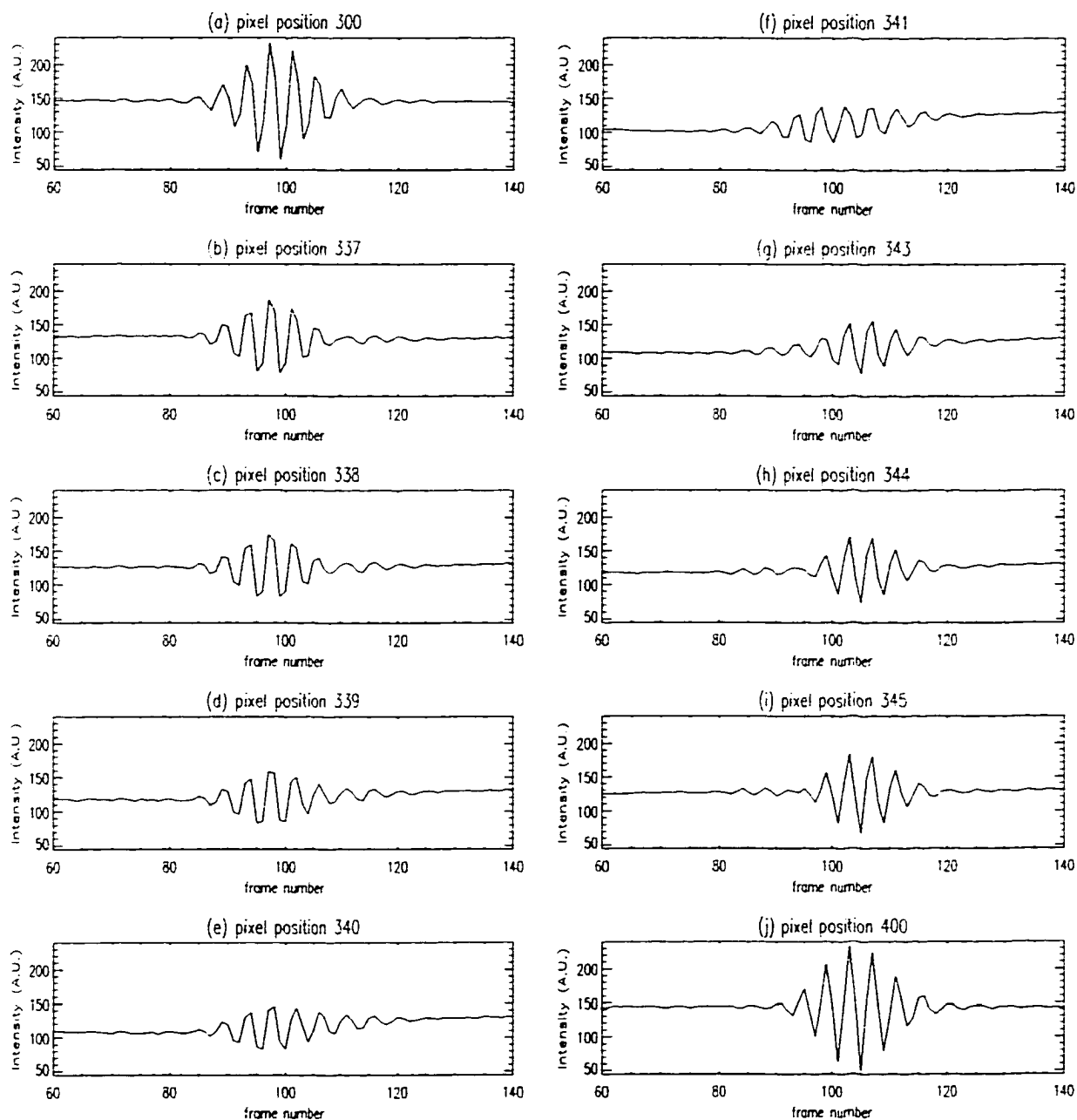
Figure 5.5: **The correlograms of 460 nm height standard across the step discontinuity. (a) far from the edge on the top side. (b) to (i) close to the edge. (j) far from the edge on the bottom side.**
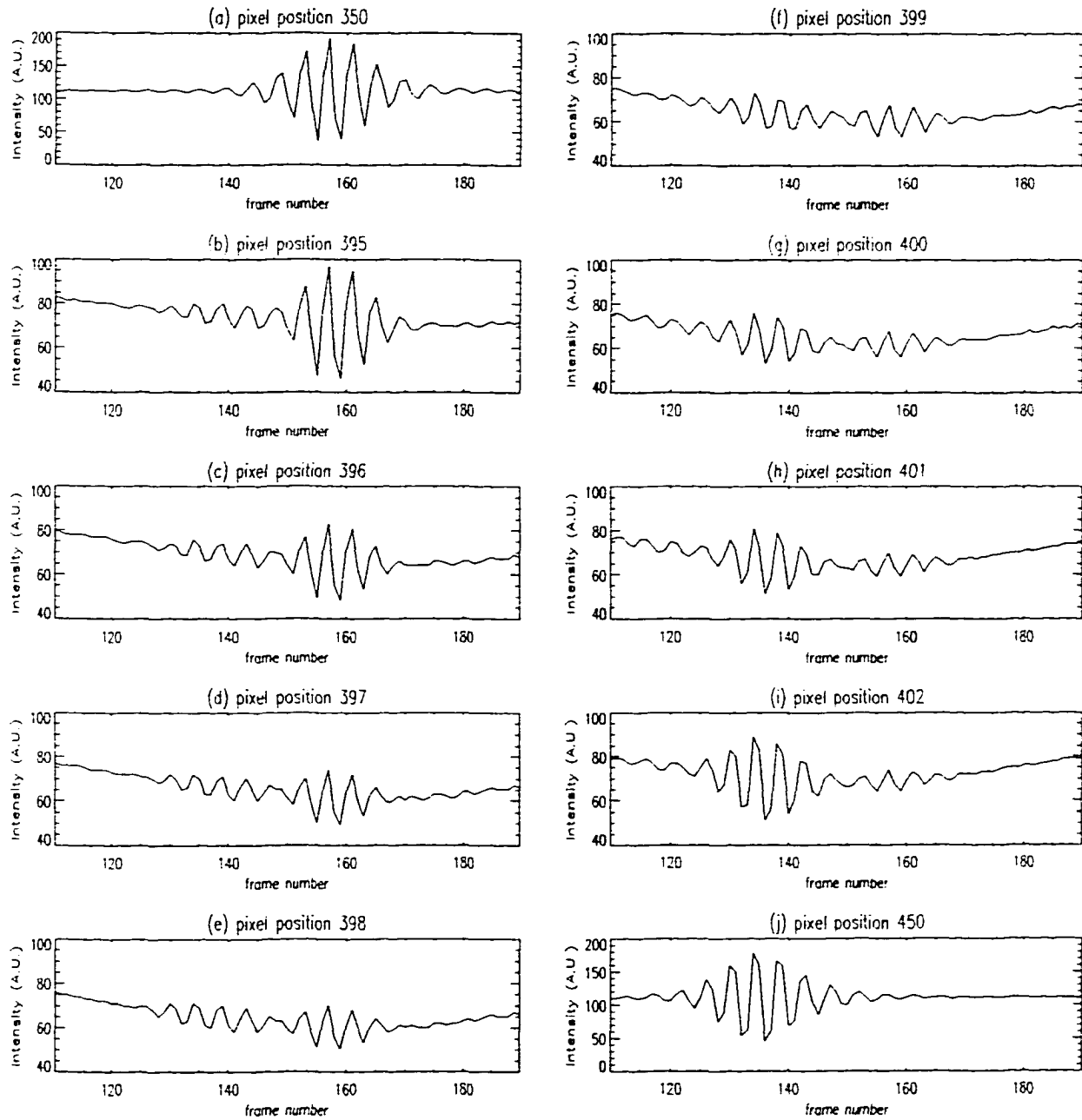
Figure 5.6: **The correlograms of 1.7 micron height standard across the step discontinuity. (a) far from the edge on the bottom side. (b) to (i) close to the edge. (j) far from the edge on the top side.**
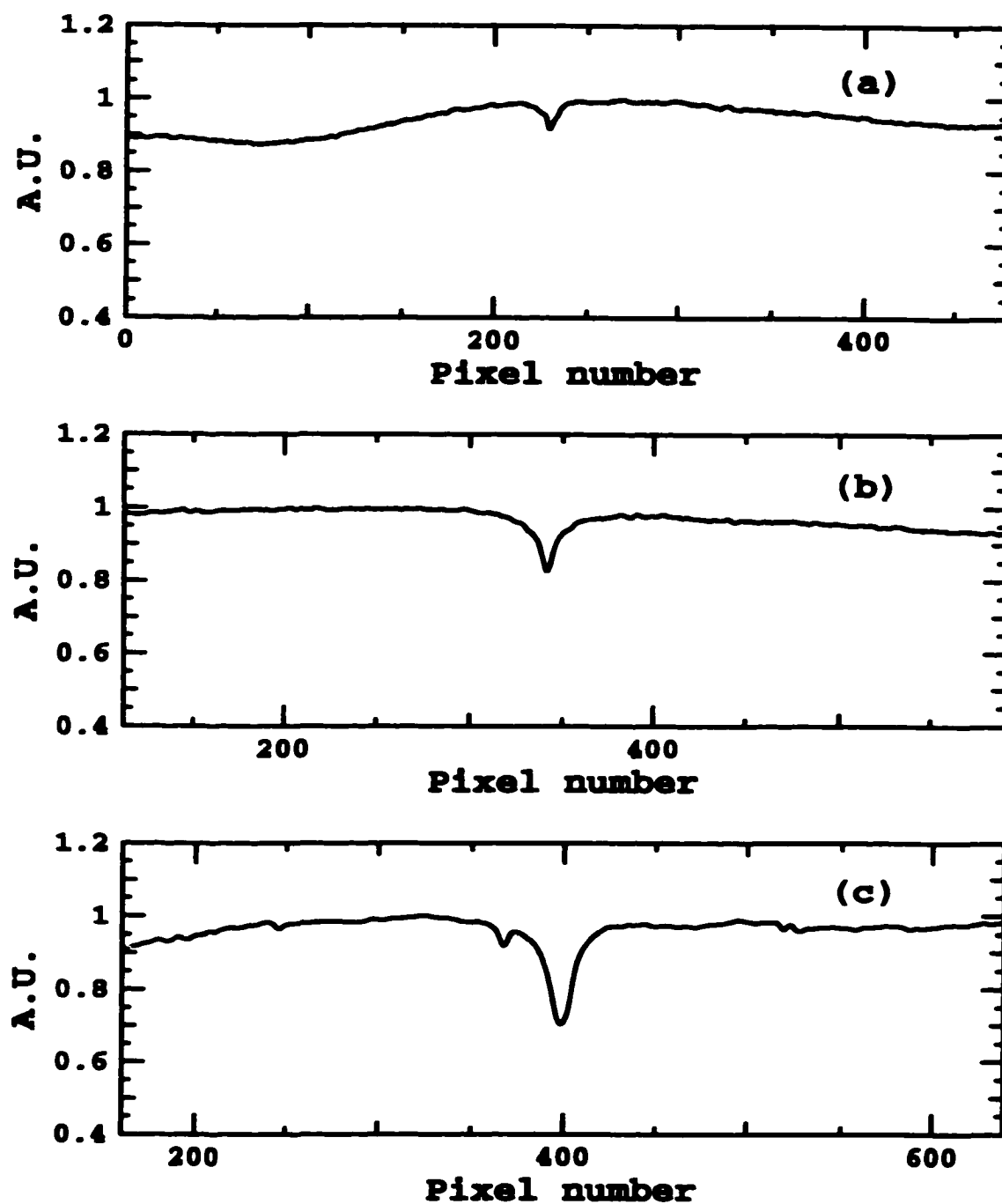
Figure 5.7: **The integrating energy of (a) 80 nm step height standard, (b) 460 nm step height standard and (c) 1.7 micron step height standard across the step discontinuity.**

the most energy reduction.

The surface heights are determined either by locating the modulation contrast peak position using the least square fit (LSF) method[35] to the discrete data points or by calculating the centroid[5, 15, 34] of the contrast. Usually calculating the centroid takes less time[5] and therefore saves computing power. From Fig. 5.4 and Fig. 5.5 we can clearly see that the peak and centroid are not necessarily coincident if there is noise in the correlogram. Also, at positions close to edges on the top (bottom) side, the peak and centroid move toward larger (smaller) frame positions than they should be. Further, the position of the centroid shifts more than the position of the modulation peak does. This explains why including more defocus data points could increase the height of bat wings[30, 35]. For simple white light two beam interference, the fringe modulation contrast is Gaussian when the light source has a Gaussian distribution as in this case, but it somehow skews at the positions close to the edges. We can imagine that the diffraction effect around the edge changes the effective reflectivity from the sample and deforms the modulation contrast when the step height is smaller than the coherence length of the light source. In the next section we will show that diffraction by two shifted apertures can cause bat wings.

5.3   Diffraction model

We model the step edge as two shifted apertures as illustrated in Fig. 5.8, assuming a plane wave normally incident to the step edge and reflecting back to the system after being diffracted by the edge. When the step height is less than the coherence length of the illumination light source, the diffracted and reflected beams from the top and bottom sides of the step edge interfere with each other and travel back to the system. The Mirau objective collects the light amplitude at the focal plane which interferes with the reference beam. The objective only transmits the amplitude distribution of the spatial frequencies lower than $\lambda/N.A.$, where λ is the wavelength. When using a white light source, the intensity collected by the CCD array is the sum of the intensities of each wavelength contained in the white light source.

We are trying to calculate the diffraction light amplitude at a distance much less than one wavelength, so the Fresnel approximation is not valid. If we limit ourselves to propagation between parallel planes, the rigorous diffraction equation can be expressed as[31]

$$u(x, y, z) = \int_{-\infty}^{\infty} \int_{-\infty}^{\infty} u(x_0, y_0, z = 0) u_{ph}(x - x_0, y - y_0, z) dx_0 dy_0. \qquad (5.3.1)$$

u_{ph} is the pinhole wave,

$$u_{ph}(x, y, z) = -\frac{1}{2\pi} \frac{\partial}{\partial z} \left(\frac{e^{ikr}}{r} \right), \qquad (5.3.2)$$

k is the wavenumber, and $r = \sqrt{x^2 + y^2 + z^2}$. $u(x, y, z)$ is the complex amplitude of the diffracted light at distance z from the aperture plane and $u(x_0, y_0, z = 0)$ is the complex amplitude at the aperture plane. Since Eq. (5.3.1) is in the form of a convolution, Fourier transforming the equation leads to a simplification of the
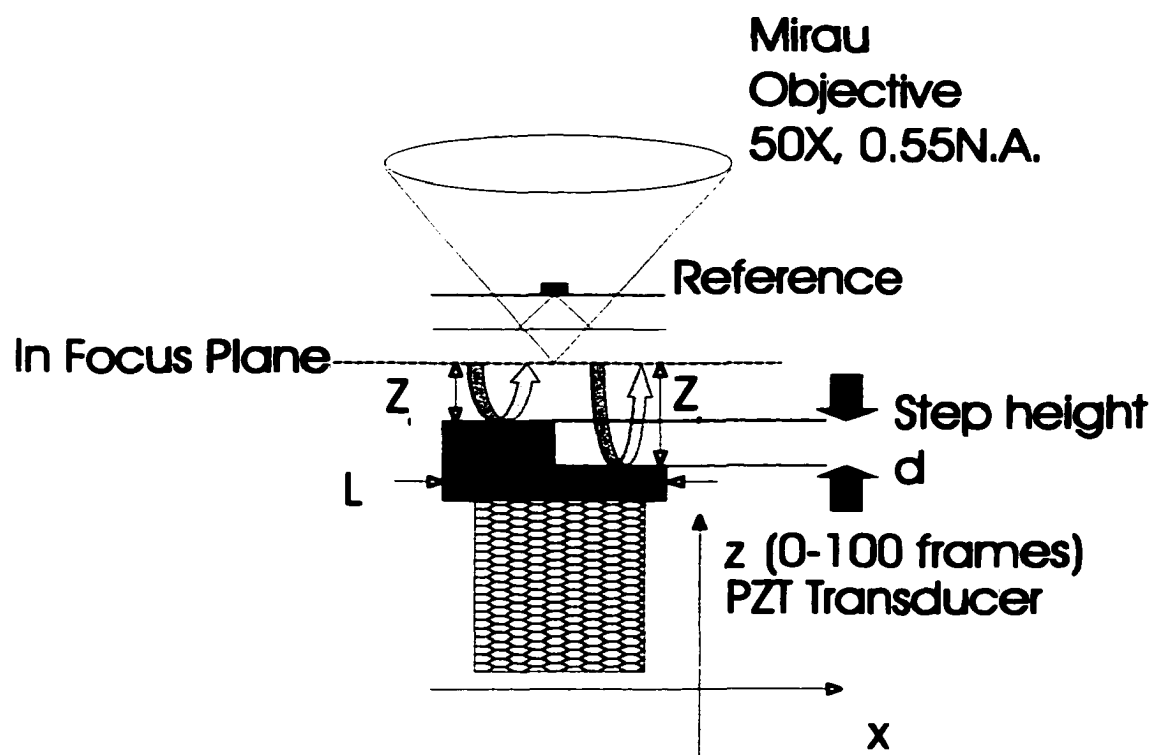
Figure 5.8: **Schematic configuration of a Mirau interference microscope and a step edge sample.**

2-dimensional convolution to a product:

$$U(\xi,\eta,z) = U(\xi,\eta,z=0) \times U_{ph}(\xi,\eta,z) \tag{5.3.3}$$

Here $U(\xi,\eta,z)$, $U(\xi,\eta,z=0)$ and $U_{ph}(\xi,\eta,z)$ are the 2-dimensional Fourier transform of $u(x,y,z)$, $u(x,y,z=0)$ and $u_{ph}(x,y,z)$, respectively. The Fourier transformed pinhole wave has a simple form,

$$U_{ph}(\xi,\eta,z) = e^{-2\pi i z \sqrt{\frac{1}{\lambda^2}-(\xi^2+\eta^2)}}, \tag{5.3.4}$$

with $z > 0$. By inverse Fourier transforming Eq. (5.3.3), we can calculate the diffraction pattern at any plane close to the diffraction aperture. The light is collected by a lens so that in this case, there are no Evanescent components and the Fourier spectrum only needs to be integrated from $-\frac{1}{\lambda}$ to $\frac{1}{\lambda}$ (Strictly speaking, $\xi^2 + \eta^2 < \frac{1}{\lambda^2}$, which makes the integration over a circle of radius of $\frac{1}{\lambda}$. To make life easier we want to separate variables, let's make the integration over a square aperture):

$$u(x,y,z) = \int_{-\frac{1}{\lambda}}^{\frac{1}{\lambda}} \int_{-\frac{1}{\lambda}}^{\frac{1}{\lambda}} U(\xi,\eta,z)e^{i2\pi(\xi x+\eta y)}d\xi d\eta. \tag{5.3.5}$$

This procedure can be easily performed with the help of the fast Fourier transform (FFT) algorithm and a fast computer.

Let's return to the Mirau interference microscope shown in Fig. 5.8. The system is essentially one dimensional, or there is no dependence on y direction so that the integral in Eq. (5.3.5) can be carried out:

$$u(x,z) = \int_{-\frac{1}{\lambda}}^{\frac{1}{\lambda}} U(\xi,z)e^{i2\pi\xi x}d\xi \tag{5.3.6}$$

and

$$U(\xi,z) = U(\xi,z=0)e^{-2\pi i z\sqrt{\frac{1}{\lambda^2}-\xi^2}}. \tag{5.3.7}$$

For wavelength λ the Fourier spectrum of the test arm beam amplitude at the focal plane of the objective is

$$U(\xi, z, \lambda) = [U_l(\xi, z = 0, \lambda)U_{ph}(\xi, z_l, \lambda) + U_r(\xi, z = 0, \lambda)U_{ph}(\xi, z_r, \lambda)] \times rect\left(\frac{\xi}{N.A./\lambda}\right).$$

(5.3.8)

U_l and U_r are the Fourier transforming of the amplitudes u_l and u_r from left and right sides, respectively of the step in Fig. 5.8.

$$u_l(x, z_l, \lambda) = a_l \, e^{-i\frac{2\pi}{\lambda}z_l} \, rect\left(\frac{x - \frac{L}{4}}{\frac{L}{2}}\right)$$

(5.3.9)

and

$$u_r(x, z_r, \lambda) = a_r \, e^{-i\frac{2\pi}{\lambda}z_r} \, rect\left(\frac{x - \frac{3L}{4}}{\frac{L}{2}}\right).$$

(5.3.10)

L is the lateral extension of the step sample. Fig. 5.8 shows $z_l = z$ and $z_r = z + d$. a_l and a_r are the relative amounts of light the objective collects from the left and right sides of the step. For the positions close to the edge on the left side, $a_l > a_r$, and for the right side, vise versa. The rectangular function represents the coherent optical transfer function of the objective. The test arm beam interferes with the reference beam, and the detector sees the intensity:

$$I(x, z) = \int_{\lambda_1}^{\lambda_2} \left| u(x, z, \lambda) + rect\left(\frac{x - \frac{L}{2}}{L}\right) \right|^2 d\lambda.$$

(5.3.11)

We performed Eq. (5.3.11) numerically. The number of sampling points in the lateral direction is $N = 1024$, and the sampling distance is $\Delta x = 1.2$ microns. So the total lateral extension $L = 1.2276$ mm in our simulation. The largest spatial frequency here is $\xi_{max} = 1/\Delta x = 834$ $lines/mm$, so that up to the wavelength of 660 nm all frequencies go through the bandpass filter set by the objective. The Mirau interference microscope we used to collect data for Figs. 5.1, 5.2 and 5.4 - 5.6

Figure 5.9: The simulated correlograms of the top portion of the 460 nm height standard. (a) far from the step edge. (b) to (e) close to the step edge.

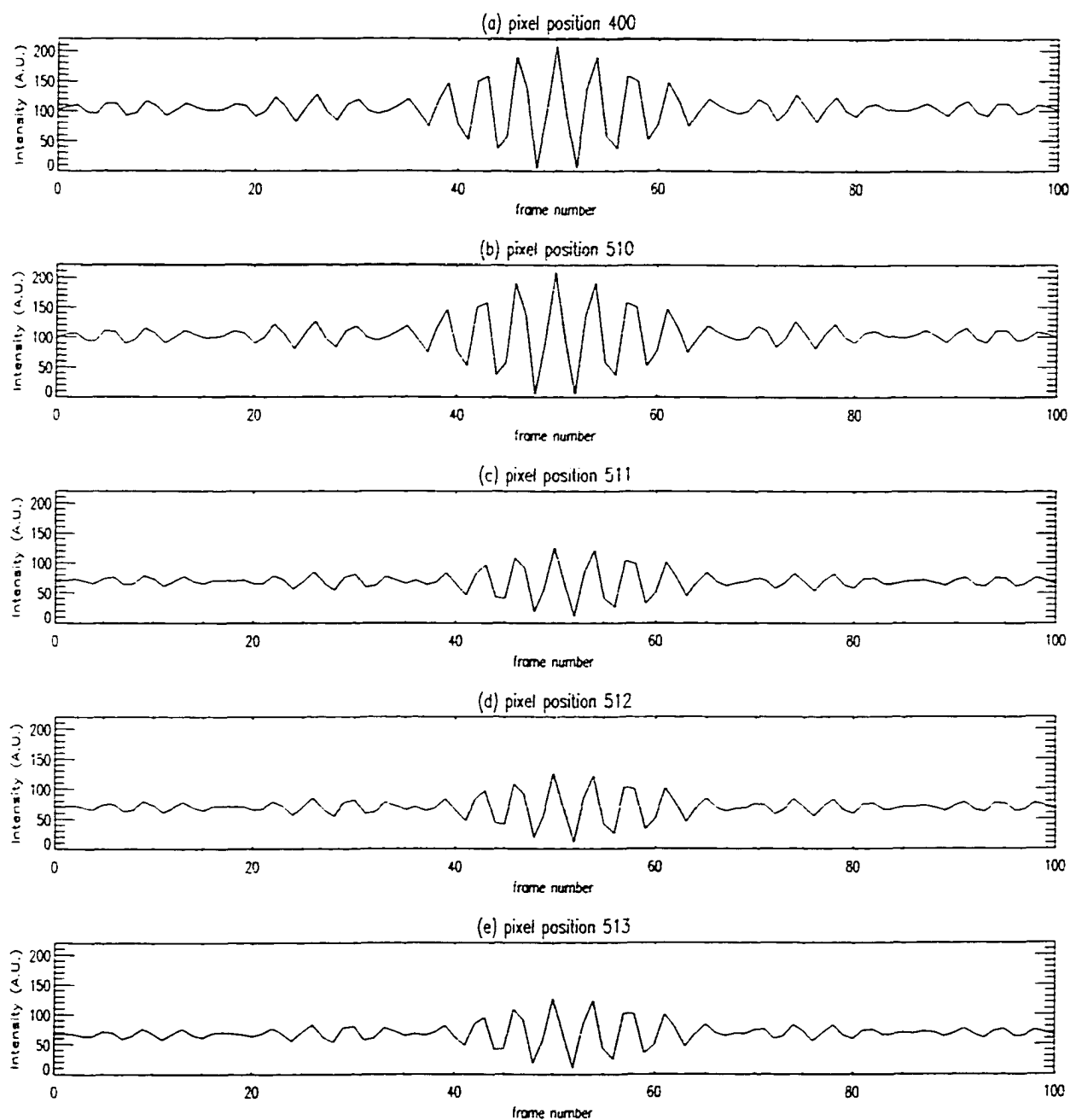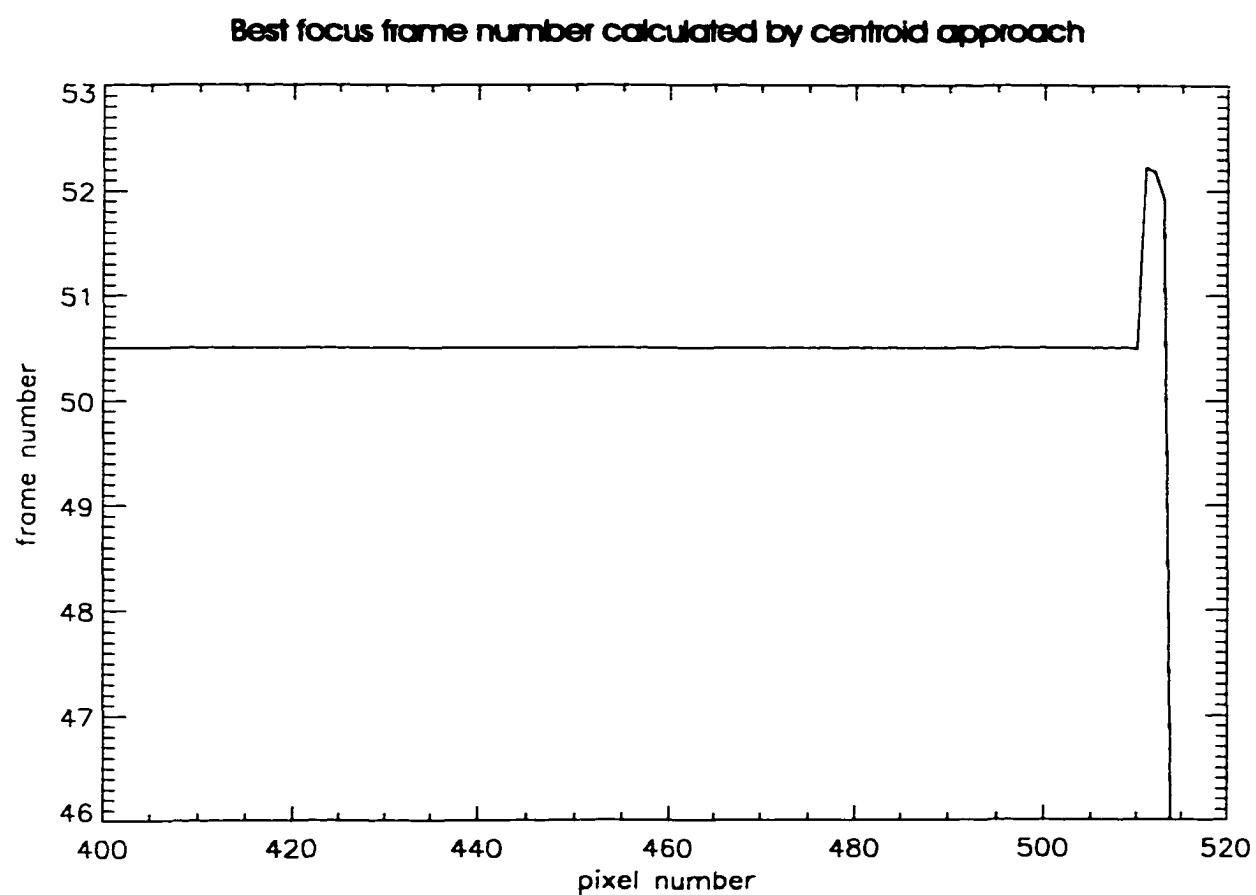Figure 5.10: **The calculated best-focus frame of the top portion of the 460 nm height standard.**
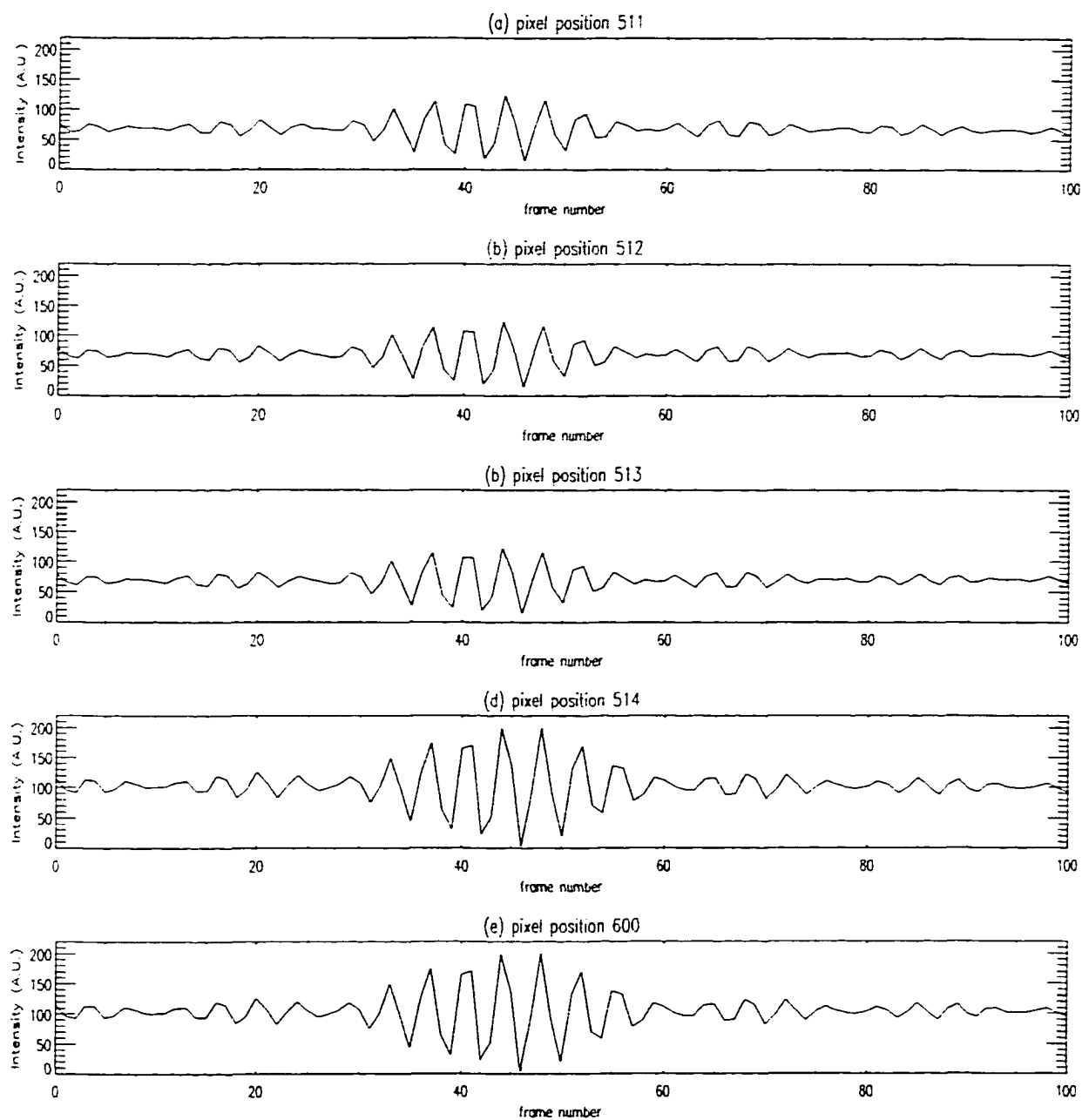
Figure 5.11: **The simulated correlograms of the bottom portion of the 460 nm height standard. (a) to (d) close to the step edge. (e) far from the step edge.**
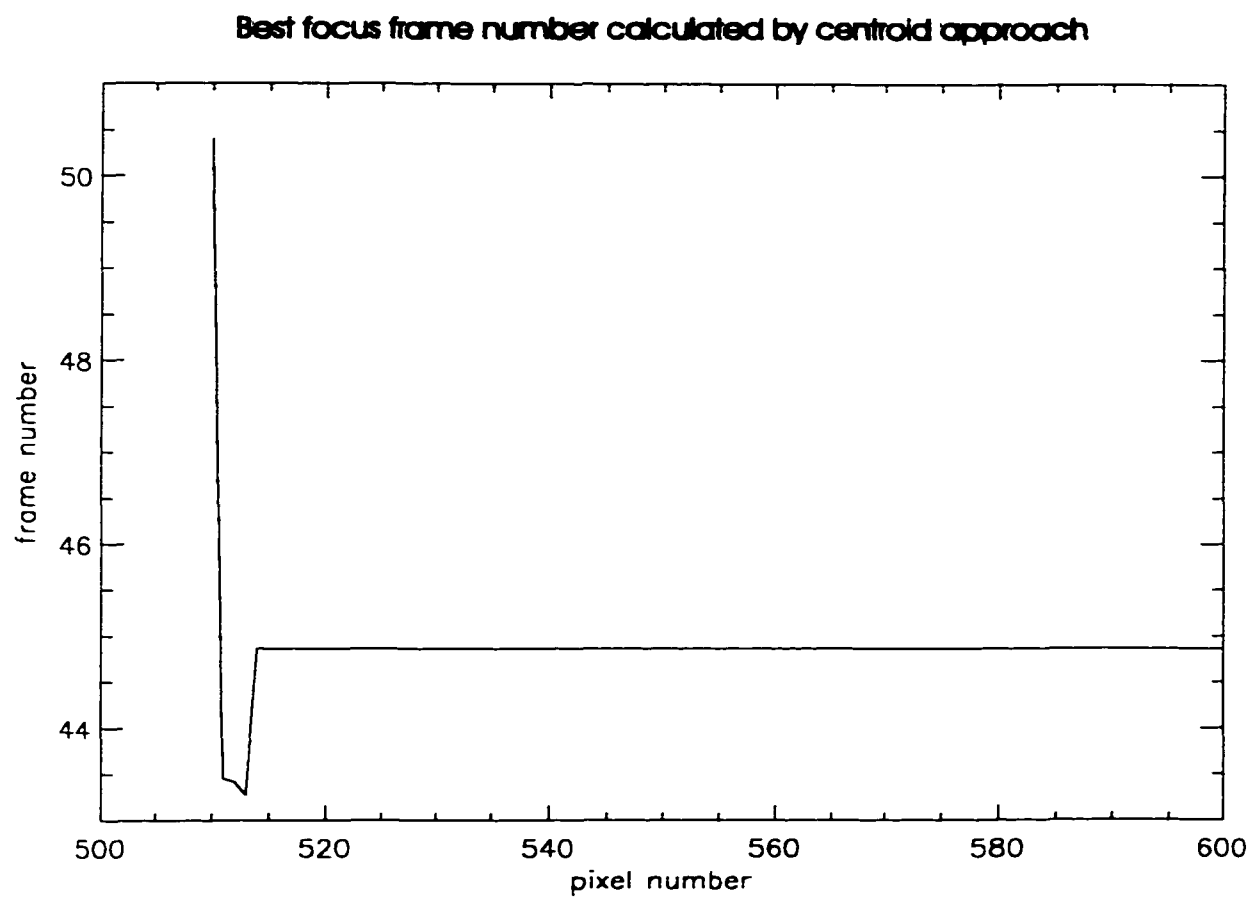
Figure 5.12: The calculated best-focus frame of the bottom portion of the 460 nm height standard.

operates at center wavelength of 600 nm when using an unfiltered tungsten light bulb as a white light source. To meet this condition we chose a flat wavelength distribution from $\lambda_1 = 540$ nm to $\lambda_2 = 660$ nm in our simulation. Therefore we can eliminate the rect function from Eq. (5.3.8), which makes the calculation much simpler. The interference microscope moves the objective or the sample stage in 80 nm steps and sends CCD images to the computer through the whole vertical scanning range. We set the sampling distance in the axial direction at $\Delta z = 80$ nm as in the real case. Fig. 5.9 shows the simulated correlograms for the top portion of the 460 nm height standard by setting the step height $d = 460$ nm and the relative light ratio from left side (top, [0, 510]) $a_l = 2$ and right side (bottom, [514, 1023]) $a_r = 1$. $a_l = 1.5$ and $a_r = 0.5$ at the boundary positions x=[511, 513], such that the objective collects light from both sides. The best-focus frame calculated from the correlograms using centroid approach[5] is shown in Fig. 5.10. By setting $a_l = 1$ for the positions x=[0, 510], $a_r = 2$ for the positions x=[514, 1023] and $a_l = 0.5$, $a_r = 1.5$ for the boundary positions x=[511, 513], the bottom side profile is calculated as well. Fig. 5.11 and Fig. 5.12 show the correlograms and profile, respectively. The simulated correlograms clearly possess the properties the measured correlograms have: (a) the energy and modulation contrast decreases, and (b) the modulation contrast envelope skews at the positions close to the step edge. Consequently, the profile calculated using the same algorithm shows significant bat wings. The simulation results can be explained as follows:

1. The objective collects the light from an area having the Airy disk diameter ($1.22\frac{\lambda}{N.A.}$) extension. At the positions close to the step edge, part of the light comes from the top portion of the step edge, and the other part comes from the bottom portion of the edge. If the CCD array pixel sees the top (bottom) part

close to the edge, there is relatively more light reflected and diffracted back to the system from the top (bottom) part.

2. When the step height is less than the coherence length of the white light source, the light from the top portion and bottom portion interfere with each other. As a result, the fringe modulation envelope skews so that both the peak position and the centroid shift away.

3. Constructing the surface profile by locating the peak position or the centroid of the modulation contrast gives bat wings.

We have to mention a few things about the measurement results of the 1.7 micron height standard. The correlograms of the positions close to the step edge in Fig. 5.6 clearly show two coherence envelopes shifted about the distance of the step height. The two envelopes can be explained as two independent interference phenomena, interference of the test beam from the top portion and reference beam, and interference of the test beam from the bottom portion and reference beam. The contrasts of the two interference patterns give us the intensity ratio of the light from the top and bottom of the step edge. Since the step height exceeds the coherence length of the white light source, the reflected and diffracted light from the top and bottom of the step edge do not interfere with each other. We have to point out that in this case the profile (Fig. 5.2) from the correlogram's centroid does not show bat wings but it does not give the correct surface height at the positions close to the step edge either. The centroid locates at the frame position between the two coherence envelopes; it is not the actual height position. Locating the larger peak from the two envelopes gives a better estimation of the surface height, since it is the surface height where the objective collects more light. Detailed discussion on locating the coherence envelope

peak or centroid position is given in reference [35].

5.4 Conclusion

The bat wings effect affecting all white light vertical scanning techniques in interference microscopes is discussed from the fringe contrast envelope skewing effect. A diffraction model is given to explain the envelop skewing close to the step discontinuity when the step height is less than the coherence length of the source. The model has successfully simulated the envelop skewing and the bat wings.

Chapter 6

PSI ON THE FLY TECHNIQUE

This chapter describes a method combining phase-shifting and coherence-peak-sensing (also referred as vertical scanning interferometry (VSI), white light interferometry (WLI), and so on.) techniques, called here "PSI on the Fly" technique, that enables measurements with the height resolution of phase-shifting interferometry without the $\lambda/4$ per data sample interval slope limitation of phase-shifting interferometry. A five frame algorithm is used to determine both best-focus frame position and the fractional phase from the best-focus frame of the correlogram acquired through vertical scanning. The two surface profiles retrieved from the phase and modulation contrast of correlograms are compared in the phase unwrapping process to remove fringe order ambiguity.

6.1   Introduction

Phase-shifting interferometry (PSI)[18, 20, 38, 55, 63] (Chapter 4) accompanied by large CCD arrays and powerful, low cost computers can obtain measurements with precision up to $\lambda/1000$. However, PSI suffers from phase ambiguity problems that limit the height difference between two adjacent data points to $\lambda/4$, where

λ is the wavelength of the light used. One technique that has been successful in extending this height difference limitation is multiple wavelength interferometry (MWI)[14, 21, 32, 62]. MWI gives the precision of the wavelengths in use and the dynamic range of the equivalent wavelength given by

$$\lambda_{eq} = \frac{\lambda_1 \lambda_2}{|\lambda_1 - \lambda_2|}. \tag{6.1.1}$$

Thus, by selecting the two wavelengths, it is possible to increase the dynamic range to hundreds, even to thousands of microns. This is an excellent method to measure step heights[32], however it does not work especially well with rough surfaces[40]. On the other hand, a broad range of wavelengths and the coherence-peak-sensing approach[5, 7, 12, 15, 19, 22, 34, 35, 36, 39, 52, 54] (Chapter 2) work well with rough surfaces but are less precise. Due to the large spectral bandwidth of the source, the coherence length is short and good contrast fringes are obtained only when the two path lengths of the interferometer are closely matched in length. The interference intensity distribution along the vertical scanning direction, called here a correlogram, is attenuated by the coherence envelope with its peak (best contrast fringes) being at about the best-focus position. There are many algorithms[5, 12, 19, 22, 35, 52, 54] for finding the coherence peak that leads to improved height resolution. In order to keep the time required for measuring and computing reasonable when measuring deep surfaces, the correlograms are sampled at or below twice of the Nyquist frequency. However, these algorithms do not provide correct surface heights when the object being measured has a step-like discontinuity with a height smaller than the coherence length of the broad-band light source[4]. A diffraction effect at the discontinuity causes the coherence envelope of the correlogram to skew and the peak to shift. This false information is referred to as "bat wings" because of its appearance

in measurement. The surface heights processed by well-established coherence-peak-sensing algorithms[5, 15, 19, 22, 34] appear higher (lower) close to the top (bottom) side of the step discontinuity as shown in Fig. 5.1 in the previous chapter. It can be shown that diffraction effects modify the coherence envelope more than the phase[4] of the correlogram. Thus, phase measurement is preferred when step-like discontinuities cause bat wings.

It is very natural to arrive at the idea that combining phase-shifting interferometry with the coherence-peak-sensing technique might provide the advantages of both methods, i.e. high precision and large dynamic range, and in addition overcome the bat wings effect. K. G. Larkin[35] and P. Sandoz et al.[23] have proposed white light phase-shifting interferometry (WLPSI)[48] to achieve unambiguous and nanometric resolution measurement of objects. Their idea is to find the best-focus frame position by locating the largest modulation contrast position of the coherence envelope of correlograms and at the same time measuring the fractional phase from the best-focus frame position. P. Sandoz et al.[23] showed great height resolution improvement in measuring a tilted smooth surface and a deep silicon sample. However, no experimental results have been reported that show bat wings can be removed.

This chapter presents a simple WLPSI algorithm that gives large dynamic range and high precision measurement and removes the bat wings effect. Since the fractional phase is measured as the objective scans through focus, this technique is called "PSI on the Fly". The "PSI on the Fly" technique also removes phase ambiguities that monochromatic and white light phase-shifting interferometry are prone to.

6.2 Phase measurement from coherence peak position

Two of the first documented automated methods for determining 3-dimensional information from white light correlograms are a patent by N. Balsuramanian[7] and a paper by Davidson[39]. Today there are at least 10 different metrology companies competing in this growing market. Although a considerable number of papers describing algorithms[5, 12, 15, 19, 22, 36, 34, 35, 52, 54] retrieving 3-dimensional information from white light correlograms exist, not all are published in detail. The main concern in the correlogram analysis is how to find the coherence peak from the discrete intensity data points, without limiting the height resolution to the scanning step distance[5, 12, 19, 22, 35, 54, 52]. For the purpose of further improving height resolution, the phase information, called fractional phase, in the white light correlogram is extracted from the best focus, i.e the largest contrast axial scanning position, using PSI algorithms as proposed in WLPSI techniques. The phase information is expected to be more sensitive to the height variations[23, 26, 35, 48] than any coherence-peak-sensing techniques. The measured fractional phase from the best-focus frame[26, 41] may result in 2π ambiguities and has to be unwrapped to retrieve height information, which is an essential step in white light phase-shifting methods. Sandoz et al.[23] introduced a fringe order function to remove 2π ambiguities, which shows well-separated values for different fringe orders when the correlogram has such low noise that the assumption of local linearity of the coherence envelope is valid.

In this chapter a more intuitive way to perform 2π ambiguity corrections is proposed. Two profiles are obtained: one from the coherence-peak-sensing technique and the other from phase measurement at the best-focus frame position. The two profiles

are compared to each other and the phase ambiguities are removed as described in Section 6.3. It is necessary to have a good profile from the coherence-peak-sensing technique in order to ensure the unwrapping process works. There are two ways of finding the coherence peak position between frames from the recovered discrete modulation contrast data sets. One is a least square fitting (LSF) method[12, 35], which assumes a function form for the coherence envelope from the source distribution. The other is calculating the centroid[5, 15, 34] of the correlogram. These two methods give identical results for ideal noise-free correlograms. However, Larkin[35] showed that the centroid is more susceptible to noise. We show in Fig. 6.1 (b) an example whose centroid of correlogram is not a good estimator for the best focus position. The centroid of the coherence envelope function may shift away from the envelope peak at positions on or close to a discontinuity[4]. If the centroid shifts away from the coherence envelope peak, the obtained fractional phase may contain false information. As a result, the phase measurement should be done from the actual coherence peak position rather than the centroid position.

6.3 Phase unwrapping algorithm

To measure the fractional phase from the best-focus frame position we have to first find the frame position with maximum modulation contrast of the correlogram. The modulation contrast M at each pixel is calculated in accordance with Eq. (6.3.1) at each step of scanning[6, 35]:

$$M^2 \propto (I_2 - I_4)^2 - (I_1 - I_3)(I_3 - I_5). \tag{6.3.1}$$
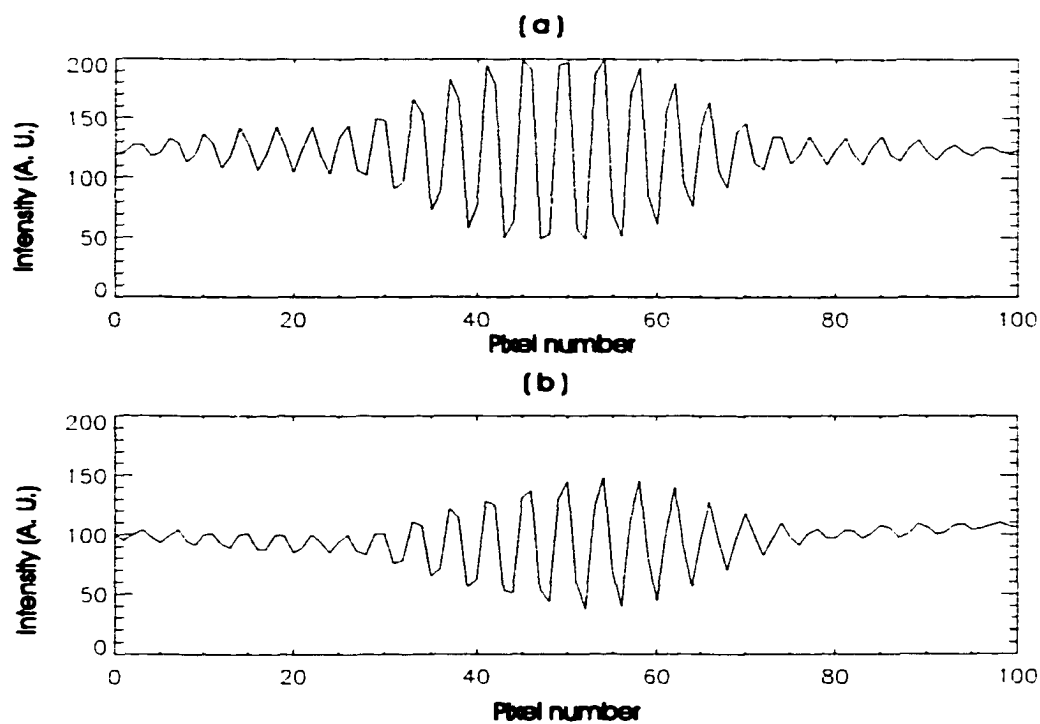
Figure 6.1: **The typical correlograms obtained with Mirau interference microscope. (a) at the position far from the step edge. (b) at the position on or close to the step edge.**
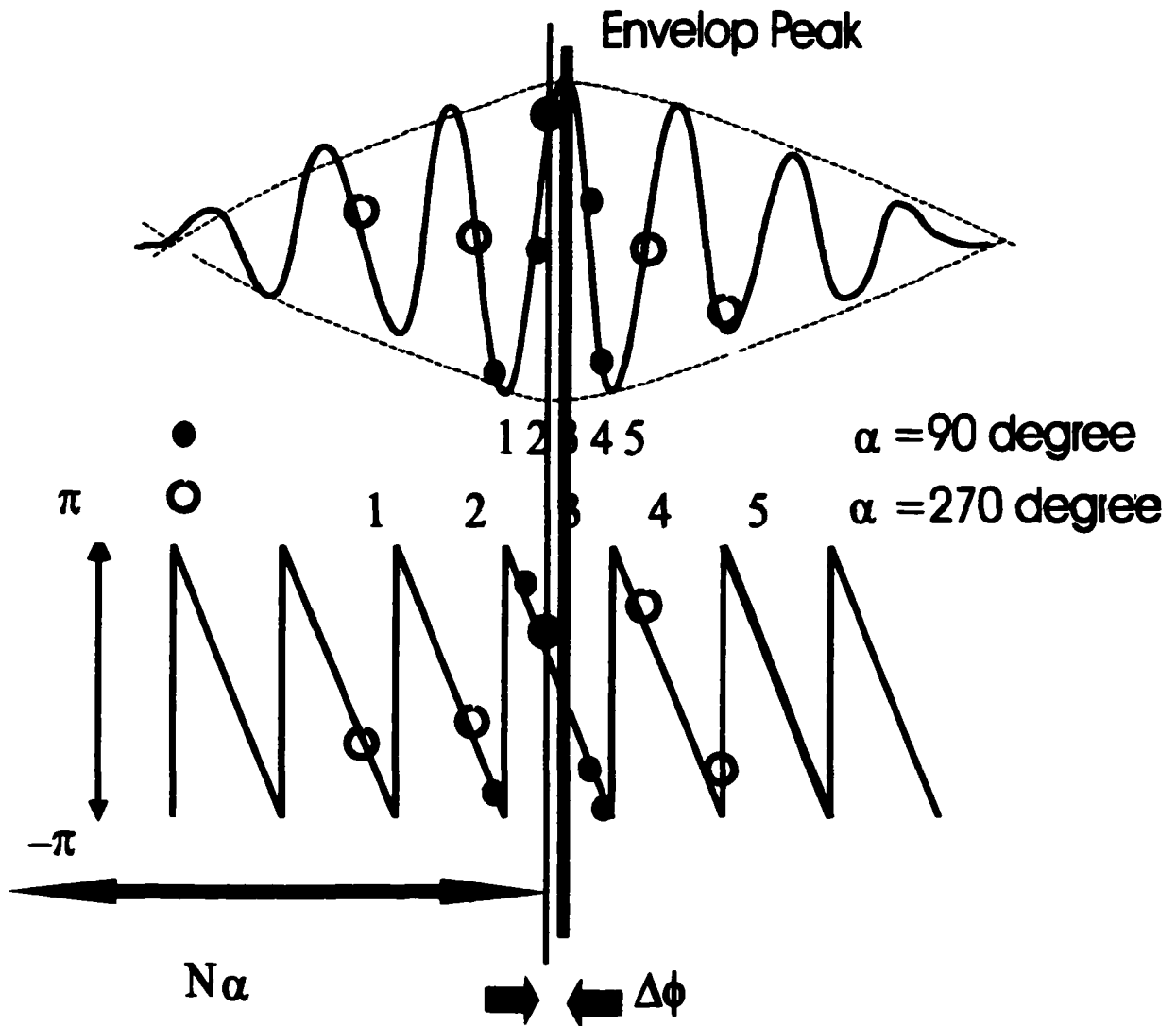
Figure 6.2: **The correlogram obtained and it's retrieved phase information while the optical path difference is scanned. The filled circle indicates 5 consecutive intensity data points apart by 90° phase shift (scanning step $\Delta = \frac{\lambda}{8}$), while the clear circle indicates 5 consecutive intensity data points apart by 270° phase shift (scanning step $\Delta = \frac{3\lambda}{8}$). $\Delta\phi$ is the relative phase from the best-focus position and $N\alpha$ is the absolute best-focus position.**

The phase step α between frames is adjusted to 90° (scanning step $\Delta = \frac{\bar{\lambda}}{8}$, where $\bar{\lambda}$ is the mean wavelength) or 270° (scanning step $\Delta = \frac{3\bar{\lambda}}{8}$). I_1 through I_5 are five consecutive frames of intensity data measured for each pixel as shown in Fig. 6.2. When the modulation is at maximum, the best-focus scanning frame position (step number) is determined. Then the phase difference $\Delta\phi$ between the zero optical path difference and the best-focus scanning position is evaluated using a five frame algorithm discussed in Chapter 2:

$$\tan[\Delta\phi] = 2\sin\alpha \frac{I_2 - I_4}{2I_3 - I_5 - I_1}$$

(6.3.2)

and

$$\sin^2\alpha = \frac{4(I_2 - I_4)^2 - (I_1 - I_5)^2}{4(I_2 - I_4)^2}.$$

(6.3.3)

The surface height is then expressed as

$$z_{phase}(x, y) = \Delta \times (step\ number) + \frac{f}{2}\left[\frac{\Delta\phi\bar{\lambda}}{2\pi}\right].$$

(6.3.4)

Here f is the so-called numerical aperture (N.A.) factor. The N.A. of an interferometric microscope objective can affect the fringe spacing and thus the surface heights measured with that objective[11, 17]. The N.A. effect is briefly discussed in Section 2.3. The N.A. factor in Eq. (6.3.4) takes care of this effect and is regarded to be determined experimentally.

Sandoz et al.[23] point out that the phase ambiguity in Eq. (6.3.2) can be avoided if the central intensity I_3 is recorded within the zero-order fringe. However, it is difficult to ensure this condition, especially for the 270° phase step between frames. Thus Eq. (6.3.4) should be rewritten as

$$z_{phase}(x, y) = \Delta \times (step\ number) + \frac{f}{2}\left[\frac{(\Delta\phi + 2k\pi)\bar{\lambda}}{2\pi}\right],$$

(6.3.5)

where k is the fringe order which has to be determined in the unwrapping process.

In this chapter we propose removing the phase ambiguity from $z_{phase}(x, y)$ by introducing a surface profile, $z_{envelope}(x, y)$, obtained from a coherence-peak-sensing technique as a reference. The reference surface profile can be calculated by finding first the best-focus frame. Then the peak location of the coherence envelope is calculated from the best focus frame, using the LSF of the modulation contrast[35]. Therefore, our reference profile can be expressed as

$$z_{envelope}(x, y) = \Delta \times (step \ number) + \Delta z, \qquad (6.3.6)$$

where

$$\Delta z = 0.4\Delta \frac{L_1 + 3L_2 - 3L_4 - L_5}{L_1 - 2L_3 + L_5} \qquad (6.3.7)$$

and L_n represents the logarithm of the modulation contrast value M_n. The small correction Δz is important to ensure the phase unwrapping process works. By simply comparing the surface profile $z_{phase}(x, y)$ to the other surface profile $z_{envelope}(x, y)$, the 2π ambiguity ($\frac{1}{2}\bar{\lambda}$ in height) can be removed from $z_{phase}(x, y)$ and the resulting height resolution obtained is as good that obtained through as regular phase-shifting interferometry[18, 20, 38, 55, 63].

To achieve this the 2π phase ambiguities can be removed in three steps. In the first step, the phase unwrapping process should start from a reliable position, for example, using the modulation contrast of correlograms as an indicator for a smooth surface. However, we have found that integrating the energy through the vertical scan shown in Fig. 6.3(a) could be a better indicator for a surface with discontinuities to avoid the suspicious positions. The energy reduction is clear at the positions close to edges in the height standard ($VLSI$, $SHS4600\text{Å}$), which has 460.6 nm step and same height wells on the surface. For this particular sample, the unwrapping is done
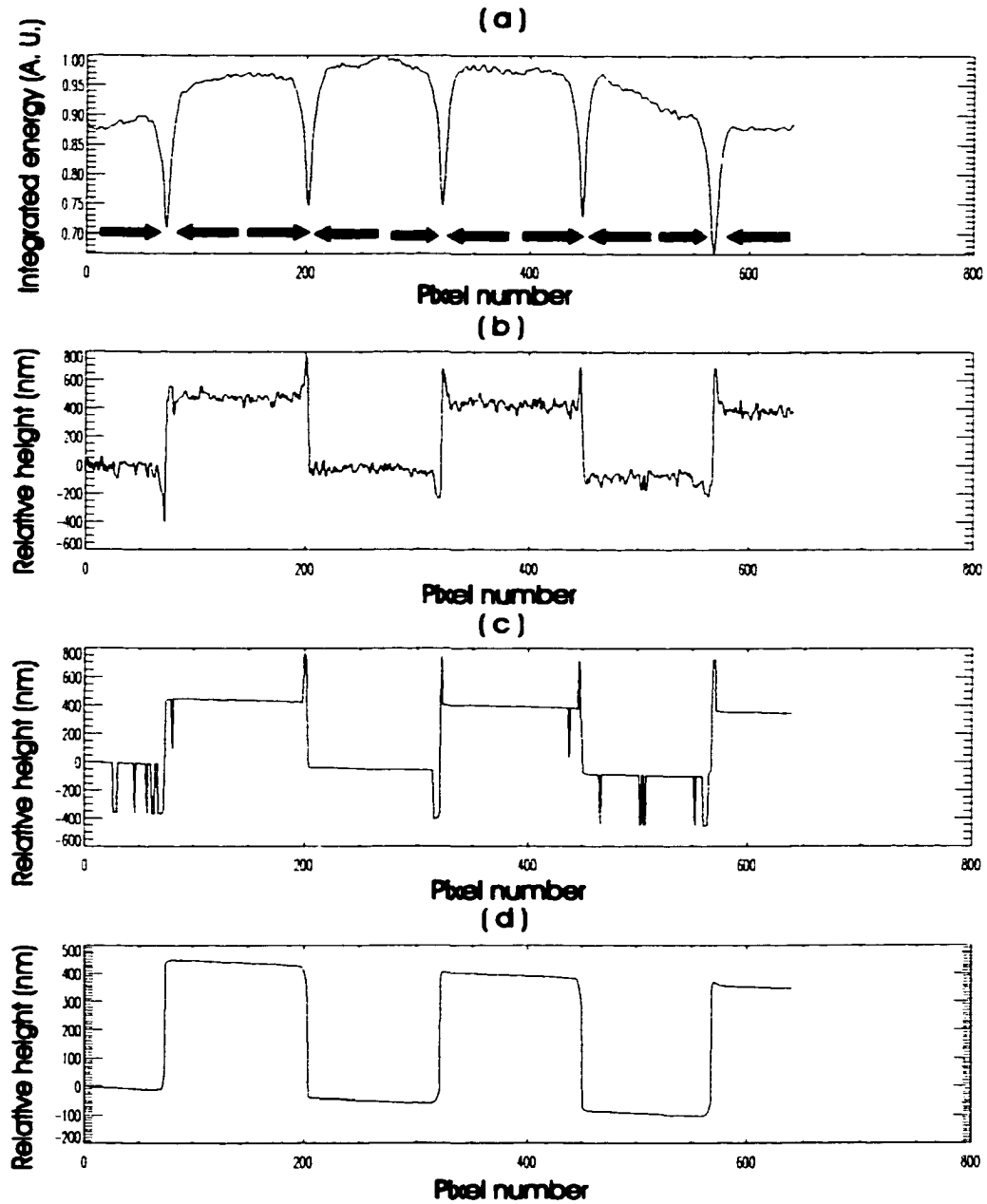
Figure 6.3: **The processed surface profile of a 460nm height standard** ($VLSI$, $SHS4600\mathring{A}$). **(a) Energy distribution along pixel positions. (b) The surface profile obtained using Eq.(6.3.6). (c) The surface profile obtained using Eq.(6.3.4). (d)The resulting unwrapped surface profile.**

from the relatively high energy positions to the energy minimums as illustrated by arrows in Fig. 6.3(a). Fig. 6.3 (b) and (c) show the surface profile calculated from Eq.(6.3.6) and Eq. (6.3.4), respectively. Bat wings are significant in the coherence-sensing-technique, as expected, since the coherence length of the light source[42] is larger than the step height. We can clearly see at this point that the integrated energy is a very good indicator of the possibility of the existence of bat wings[4]. In the second step, $z_{phase}(i)$ and $z_{envelope}(i)$ are compared at lateral position i to see if the height difference between them is smaller than $\frac{f}{4}\bar{\lambda}$, i.e.

$$|z_{phase}(i) - z_{envelope}(i) + offset| \leq \frac{f}{4}\bar{\lambda}. \qquad (6.3.8)$$

If this condition is not satisfied, then $\frac{f}{2}\bar{\lambda}$ needs to be added or subtracted to the surface height obtained from Eq. (6.3.4) until the condition is filled. The offset can be estimated by taking the average of the difference of the two surface profiles, i.e., offset$\simeq \frac{1}{N}\sum_{i=1}^{N} [z_{envelope}(i) - z_{phase}(i)]$. The offset takes care of the constant phase shift upon reflection, though we do not need to know or measure what it is. The process described by Eq. (6.3.8) is effective for the continuous portion of the surface but can not remove the 2π jumps at positions close to edges because of the bat wings effect. The third step in the unwrapping procedure needs to be taken in order to remove the bat wings effect. For the positions in which the height difference between two adjacent points in $z_{envelope}$ is smaller than $\frac{f}{4}\bar{\lambda}$ while the difference in z_{phase} is larger than $\frac{f}{4}\bar{\lambda}$, such that,

$$|z_{envelope}(i) - z_{envelope}(i-1)| < \frac{f}{4}\bar{\lambda} \quad and \quad |z_{phase}(i) - z_{phase}(i-1)| > \frac{f}{4}\bar{\lambda}, \qquad (6.3.9)$$

$n\frac{f}{2}\bar{\lambda}$ is added or subtracted to z_{phase} to satisfy the condition

$$|z_{envelope}(i) - z_{envelope}(i-1)| < \frac{f}{4}\bar{\lambda} \quad and \quad |z_{phase}(i) - z_{phase}(i-1)| < \frac{f}{4}\bar{\lambda}. \qquad (6.3.10)$$

Fig. 6.3(d) shows the resulting surface profile after the full correction processes. We see that both the 2π jumps and bat wings are completely removed. Consequently, a great improvement in surface resolution is achieved. It is questionable if the correction process described by Eq. (6.3.9) and Eq. (6.3.10) works when the bat wings' height changes by more than $\lambda/4$ between data points. The bat wings usually have lateral extension over several pixels, and the maximum height is less than 200 nanometers[4] measured with a white light source having mean wavelength near 600 nanometers. Therefore, we can assume the bat wings artifact introduces an error in the height difference between two adjacent data points of less than $\bar{\lambda}/4$ for most cases. At this time it is prudent to discuss situations in which the proposed method works and those in which it does not. As mentioned before, this method requires a good surface profile from the coherence-peak-sensing measurement, which should not be off randomly more than $\bar{\lambda}/4$. In other words, if the surface profile calculated by Eq. (6.3.6) is not meaningful, the proposed algorithm probably will not work well. One situation in which the algorithm does not work well is periodic structures like gratings that diffract the illuminating light away from the system so that the signal-to-noise ratio is so low that it is difficult to produce the correct surface profile from the modulation contrast of the correlograms.

6.4   Experimental results

The experiments were carried out using a Mirau interference microscope (Veeco, WYKO NT-2000) as illustrated in Fig. 6.4. A Nikon 50X magnification objective ($N.A. = 0.55$) was used since bat wings effects are significant for large numerical apertures[4]. Correlograms were detected by a CCD video camera while a PZT transducer (Queensgate instruments, NPS-Z-15B stage position) was used instead of the
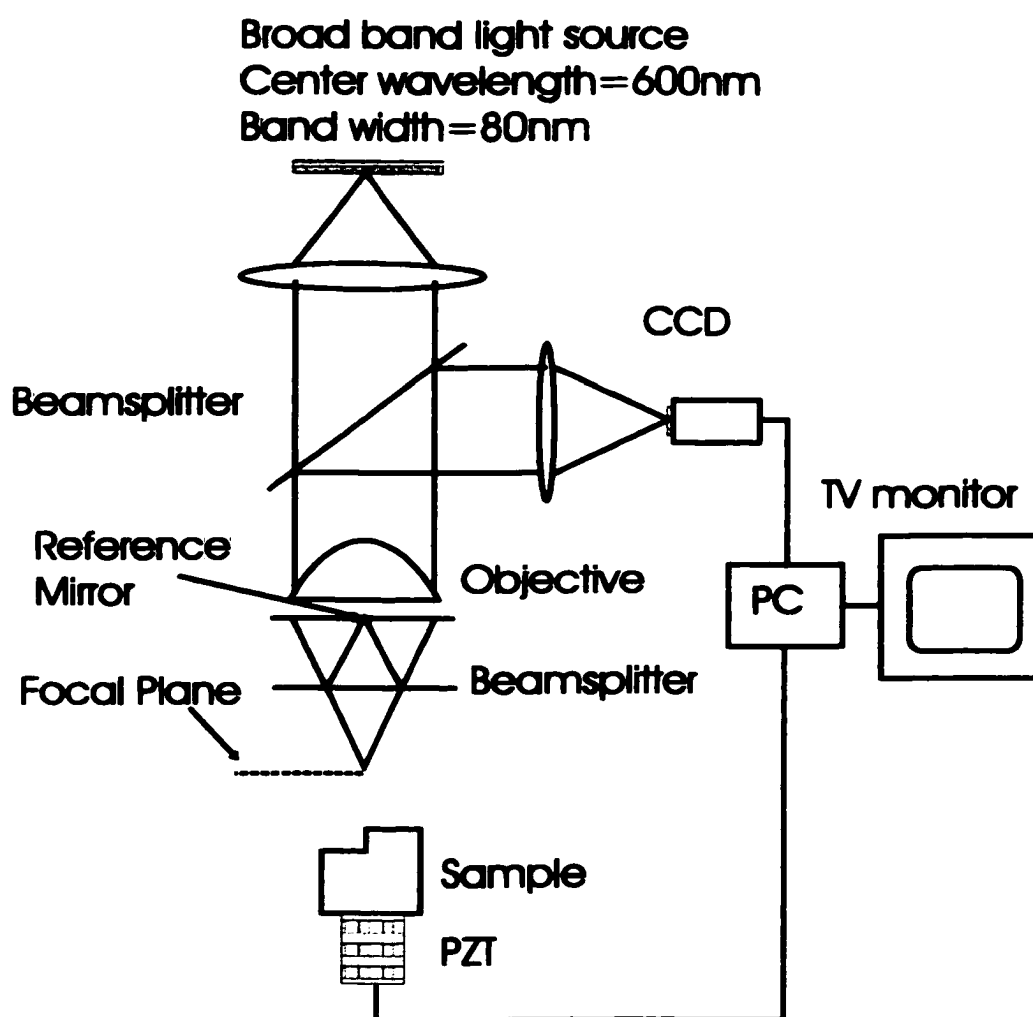
Figure 6.4: **Experimental set-up of Mirau interference microscope (Veeco, WYKO NT-2000).**

high precision motor in the commercial version WYKO NT-2000 for vertical scanning. The PZT transducer was used because equally spaced scanning steps between frames are required to minimize phase-shifting errors[18, 38]. A high precision motor may be used for scanning through samples having surface structures over millimeters, as long as the errors caused by the motor have been measured and can be removed by signal-processing techniques[1, 6, 20, 35, 55]. The broadband light source was either an unfiltered tungsten bulb or filtered source of center wavelength at 600 nm with 80 nm bandwidth. The former gives better resolution in the coherence-peak-sensing technique[5, 7, 12, 15, 19, 22, 34, 35, 36, 39, 52, 54, 63] and the latter is preferred for phase-shifting interferometry[18, 20, 38, 55, 63] with high magnification objectives.

Fig. 6.5 and Fig. 6.6 present measured surface profiles of a ball bearing, which cannot be measured by the regular phase-shifting technique with high magnification objectives, because the objective depth of focus is smaller than the depth of the sample. From the top, (a) is the result obtained by coherence-peak-sensing technique according to Eq. (6.3.5), (b) is the raw output from Eq. (6.3.4), and (c) is the final result after 2π corrections using the algorithm proposed in Section 6.3.

Table 6.1 summarizes the roughness average (R_a) and root mean square (rms) roughness (R_q), which are defined as follows:

$$R_a = \frac{1}{N} \sum_{i=1}^{N} |z(i) - z_{fit}(i)| \qquad (6.4.1)$$

and

$$R_q = \sqrt{\frac{1}{N} \sum_{i=1}^{N} [z(i) - z_{fit}(i)]^2}, \qquad (6.4.2)$$

where z_{fit} is found by fitting the sag equation to the mean average of the surface heights of (a) and (c) in Fig. 6.5 and Fig. 6.6. The rms deviation for different

Figure 6.5: **Surface profile of ball bearing obtained with 90° white light phase shifting. (a) Obtained by coherence-peak-sensing technique using Eq. (6.3.6). (b) Obtained using Eq. (6.3.4). (c) The final result after 2π correction.**
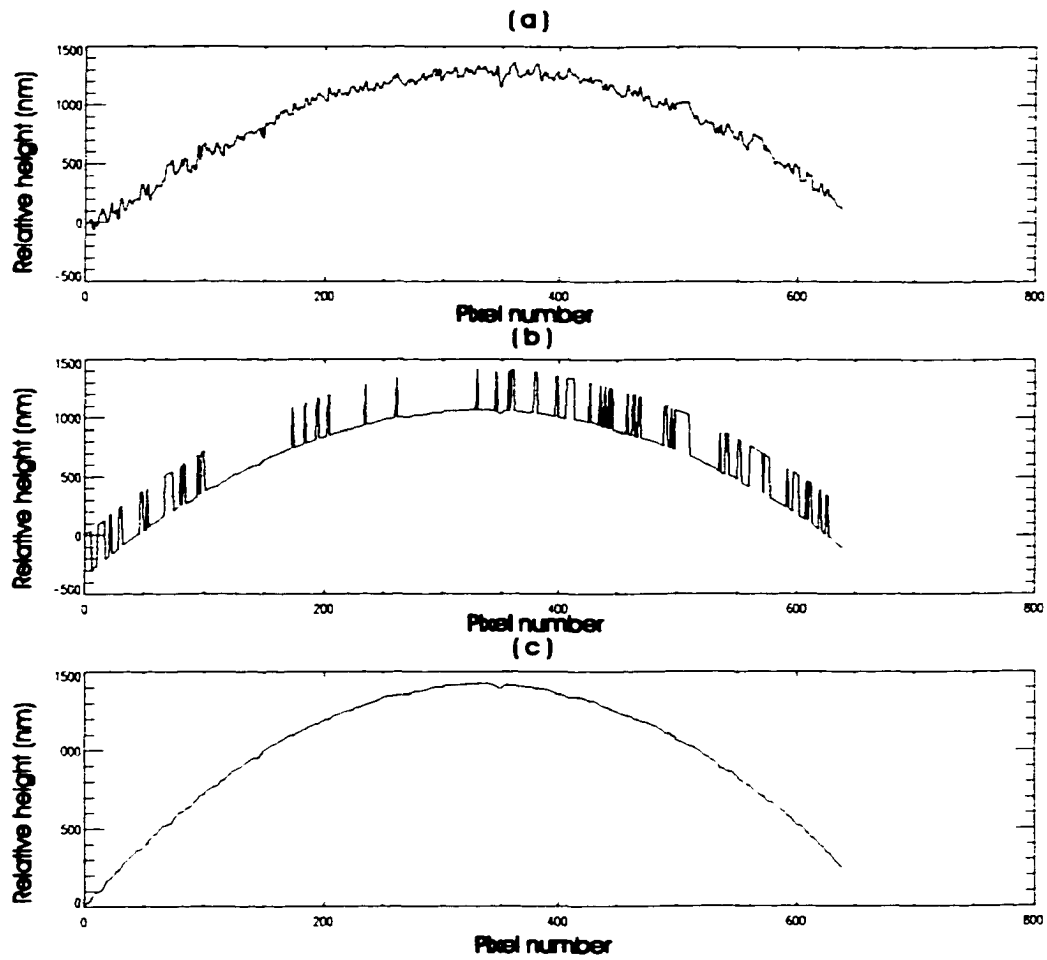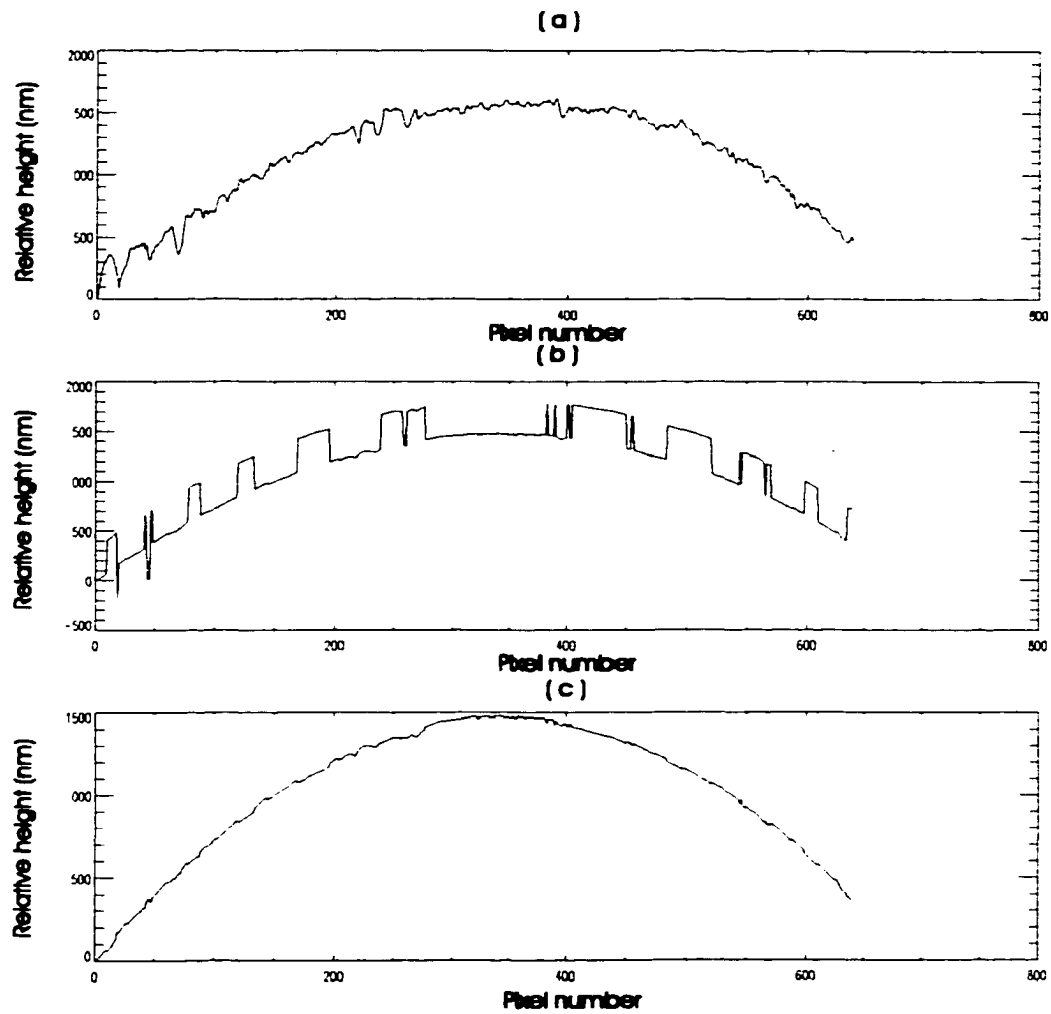
Figure 6.6: **Surface profile of ball bearing obtained with 270° white light phase shifting. (a) Obtained by coherence-peak-sensing technique using Eq.(6.3.6). (b) Obtained using Eq.(6.3.4). (c) The final result after 2π correction.**

Table 6.1: Surface roughness parameters of ball bearing for various algorithms.

	90° phase shifting		270° phase shifting		rms deviation
	R_a (nm)	$R_q(nm)$	R_a (nm)	R_q (nm)	(nm)
Coherence peak sensing[1]	36	45	41	56	68
Phase shifting[2]	9	11	14	16	14

1.based on Eq.(6.3.6), from Reference [35].
2.based on Eq.(6.3.4), after unwrapping.

techniques between 90° and 270° phase shift results is estimated and listed in Table 6.1 and can be an indicator of the repeatability of the algorithm. The numbers here do not give the absolute accuracy for the method proposed. They indicate that the height resolution indeed can be improved using the proposed algorithm as compared
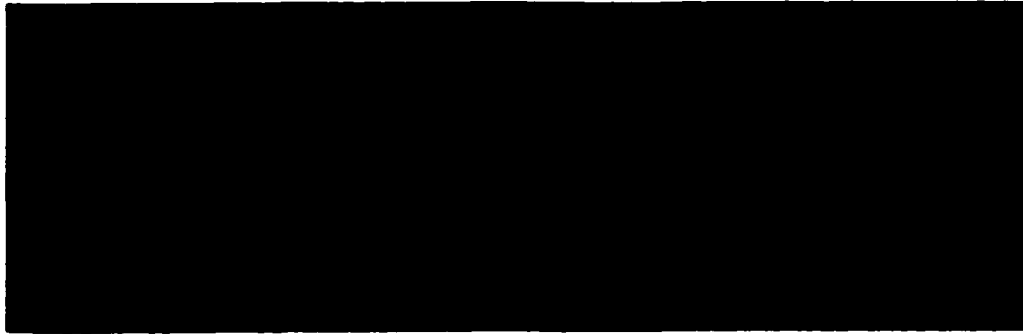
Figure 6.7: **Camera image of the step height standard** ($VLSI$, $SHS4600Å$).
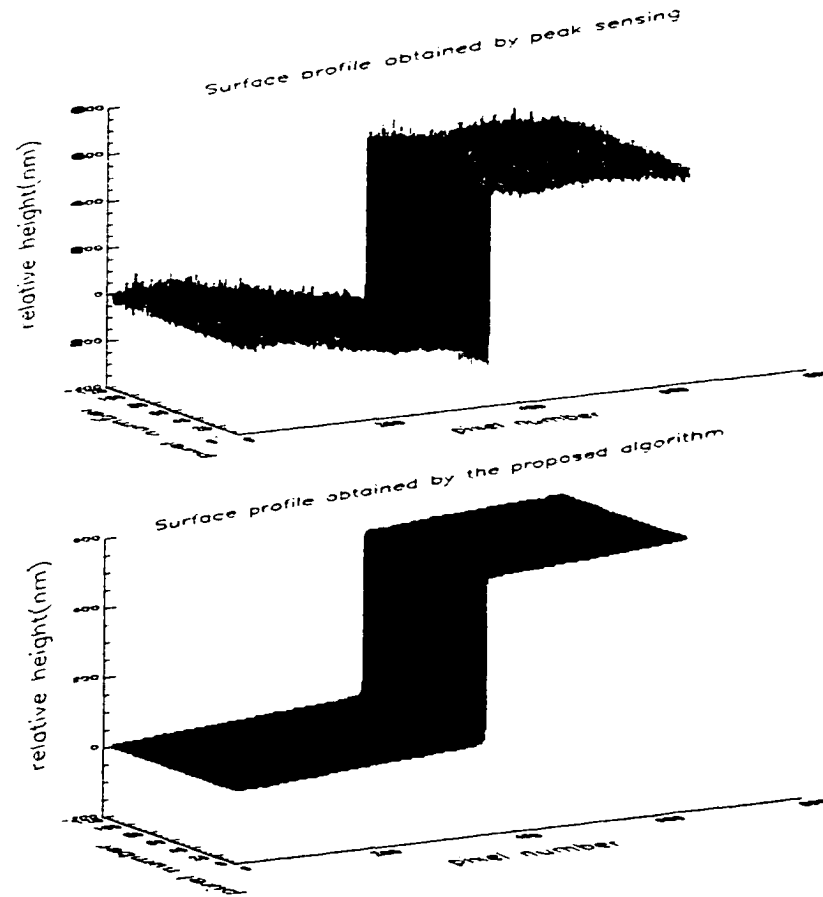
Figure 6.8: **Processed surface profile of the step height standard** ($VLSI$, $SHS4600\text{Å}$). **The measurement was done with a 80 nm band pass filter at the center wavelength of 600 nm. Top figure is the profile obtained by the regular coherence-peak-sensing algorithm**[35] **and the bottom one is obtained by the white light phase-shifting algorithm proposed in this paper.**
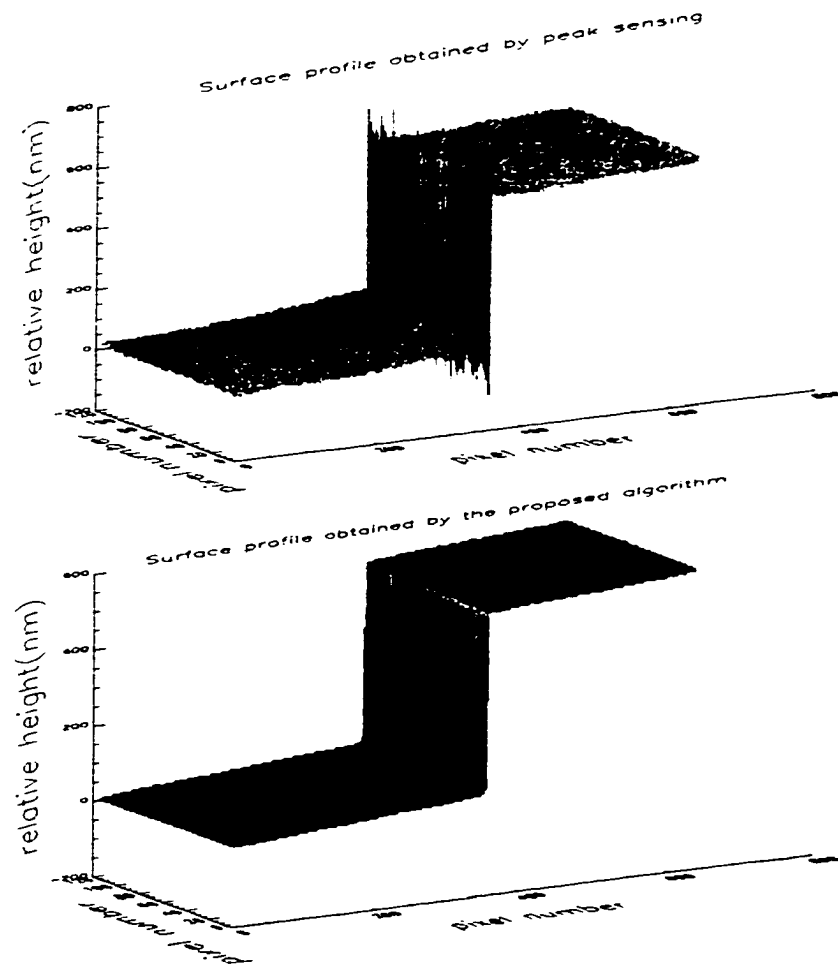
Figure 6.9: **Processed surface profile of the step height standard** ($VLSI$, $SHS4600\text{Å}$). **The measurement was done with unfiltered Tungsten light source . Top figure is the profile obtained by the regular coherence-peak-sensing algorithm**[35] **and the bottom one is obtained by the white light phase-shifting algorithm proposed in this paper.**

Figure 6.10: **Same as in Fig. 6.8. Obtained from Veeco surface processing software WYKO Vision32. (a) and (b) a hole close to the step, (c) and (d) a bump far off to the left side, in Fig. 6.7.**

to the resolution of the regular coherence-peak-sensing technique.

As stated in Section 6.3, this method is capable of removing the bat wings and revealing the surface structure on or close to edges. A step height standard ($VL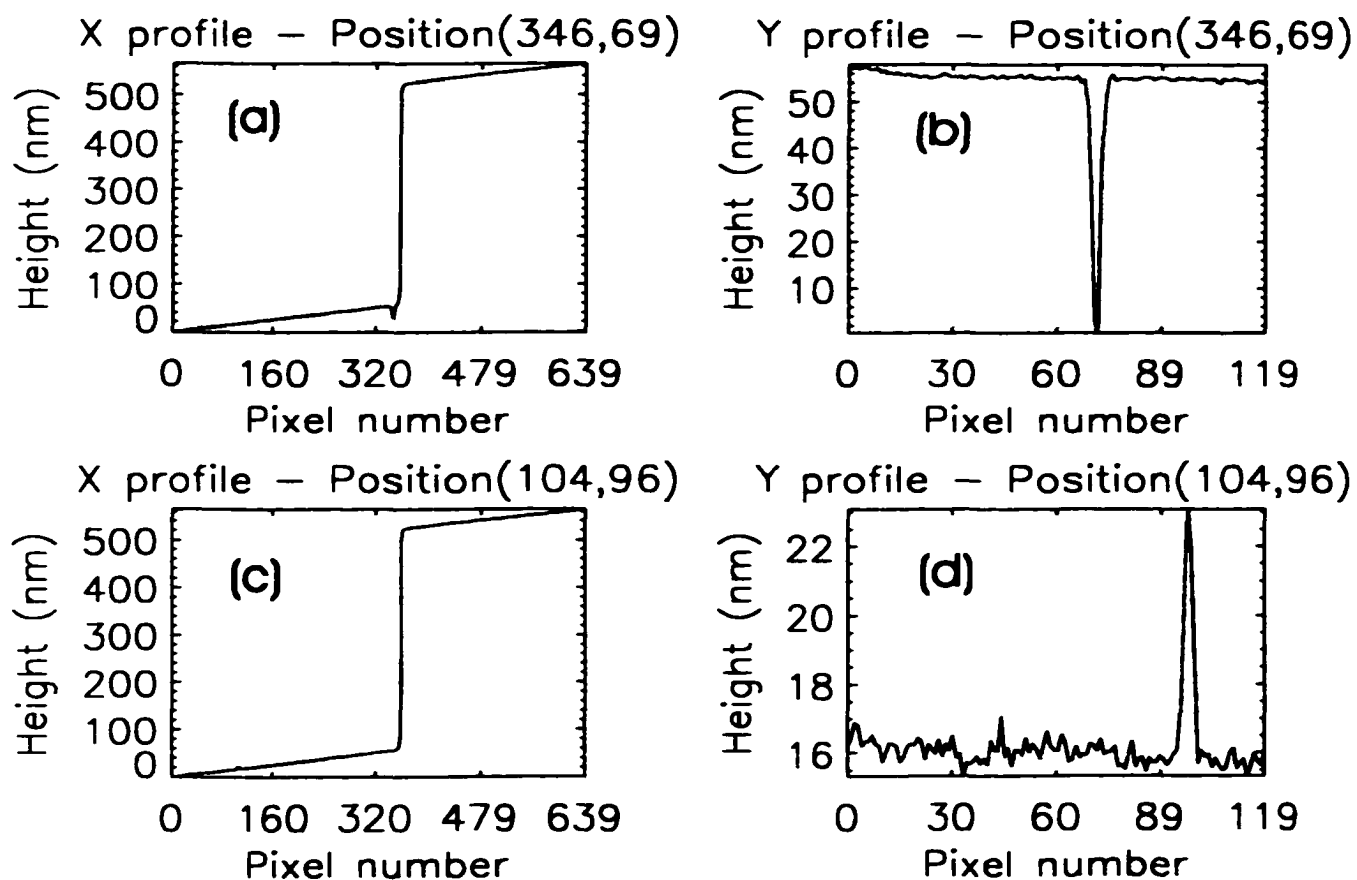SI$, $SHS4600\overset{\circ}{A}$) measurement was conducted to demonstrate the effect. The camera images of the step are shown in Fig. 6.7. Fig. 6.8 and Fig. 6.9 shows the processed profiles obtained by the method proposed in this chapter for filtered and unfiltered tungsten sources, respectively. The surface profiles from the regular coherent-peak-sensing technique are also shown in these figures for comparison. The height resolution improvement is obvious, and the bat wings are completely removed. On the left side (lower side) of the step, there are two defects on the surface, which have the appearance of stains in Fig. 6.7. With the new method the two defects were measured as a hole and a bump, which is not possible using either the coherence-peak-sensing technique or the phase-shifting method by itself. The detailed analysis is shown in Fig. 6.10 by Veeco's software WYKO Vision32. The hole close to the step was found to be 55 nm, and the bump far off to the left side was found to be 7 nm. The results powerfully prove the advantages of the proposed white light phase-shifting technique: high resolution and large dynamic range.

Every month there are several papers published on new algorithms for surface metrology and the most important claim in many of the papers is how fast the algorithm will acquire and process the surface information. From Section 6.3, it is clear that the computation time required for the white light phase-shifting method proposed in this paper is the sum of the time for regular coherence peak sensing and phase-shifting calculation. Efforts in surface metrology over the last thirty years have yielded fast algorithms to calculate surface profiles by both coherence-peak-sensing and phase-shifting technique so that the combined method, PSI on the Fly technique,

is guaranteed to be a fast algorithm for practical requirements.

6.5   Conclusion

We have shown the advantages of using a white-light, phase-shifting technique which possesses the accuracy of regular phase-shifting interferometry without the $\lambda/4$ dynamic range limitation. A simple phase unwrapping algorithm is proposed and applied to a 460 nm square well, ball bearing and 460 nm step height surface. The algorithm can remove the bat wings effect and reveal the surface structures close to the step edge.

CONCLUSION

A diffraction model is provided to explain the bat wings phenomenon. Despite the simplification, i.e. dealing only with the normally incident plane wave, which allows us to use scalar diffraction theory without any approximations, the simulations successfully generates fringe-modulation skewing effects and therefore bat wings. Thus, we can conclude that the diffracted light from the step edges interfere with each other and deform the coherence envelope shape. The key point here is that deformation of the phase information in the correlogram by the diffraction and interference effect is much less than that of the shape deformation, which led us to the idea of the PSI on the Fly technique. The PSI on the Fly technique is capable of extracting the surface information close to or on edges without bat wings, by measuring the fractional phase from the envelope peak position.

The analysis of correlograms reveals that locating the actual coherent peak position in correlograms may give better results in terms of error tolerance. Moreover, for the positions close to discontinuities, regardless of the height, the peak detection algorithm is the only way to retrieve the surface information since the conventional centroid approach loses the theoretical validity if the correlogram is not symmetrical.

The PSI on the Fly algorithm is proposed to solve the bat wings problem using the results of the correlogram analysis and the diffraction model. Because of its mathematical simplicity and large error tolerance, Hariharan's five-step WLI algorithm is adopted to locate the coherence envelope peak position and measure the fractional phase from the largest contrast frame position. The PSI on the Fly algorithm not only removes the bat wings from the edge discontinuities, but also greatly improves the height resolution to the level of the regular PSI measurement. To the second question we asked in the introduction, "Can we fix the bat wings artifact? and how?", the answer is that using the PSI on the Fly algorithm, bat wings can be removed for certain shapes.

A simple preliminary survey on the phase change upon reflection has been conducted and the results suggest that the PSI on the Fly algorithm can be applied to dissimilar material as well as same-material objects with a calibration of coherence envelope position shift because of dispersion of the dissimilar materials' refractive indices.

FUTURE WORK

A new algorithm combining VSI and PSI has been presented for the purpose of removing the bat-wings effect and improving height resolution at the same time. However, improvements in hardware and software are needed to maximize system performance.

We mentioned in Chapter 6 that the PSI on the Fly algorithm does not work well with diffraction gratings because a large part of the reflected light cannot be corrected back to the CCD with the Mirau interference objective of $N.A.=0.55$. If we use a Linnik interference microscope with $N.A.$ larger than 0.95, the signal levels of the object can be increased; therefore the SNR is expected to increase, and as a result, the surface profile might be retrieved. Fig. 6.11 and Fig. 6.13 are the surface profiles[43] obtained by a Linnik interference microscope (Veeco) with the regular VSI technique. At least there are signals going back to the system to be processed in contrast to the case of the Mirau objective. Unfortunately, the Queensgate PZT transducer cannot be connected to this Linnik profilometer for vertical scanning, so that we are not able to verify the performance of the PSI on the Fly algorithm in a Linnik configuration at this time.

Improvement in software is necessary for a fully automatic system. At this point, processing the surface information with the PSI on the Fly algorithm requires the
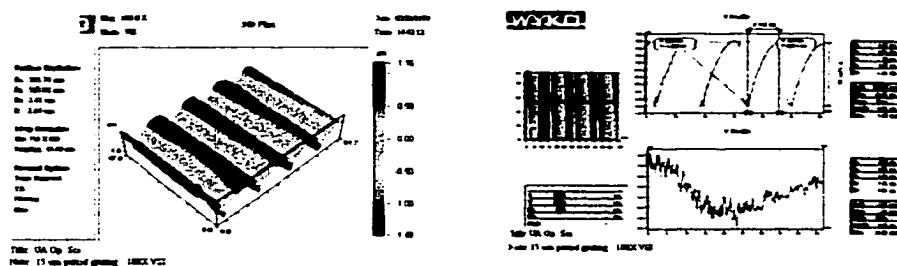
Figure 6.11: **The 3-dimensional surface profile of a 15 micron period grating and its cross profiles.**
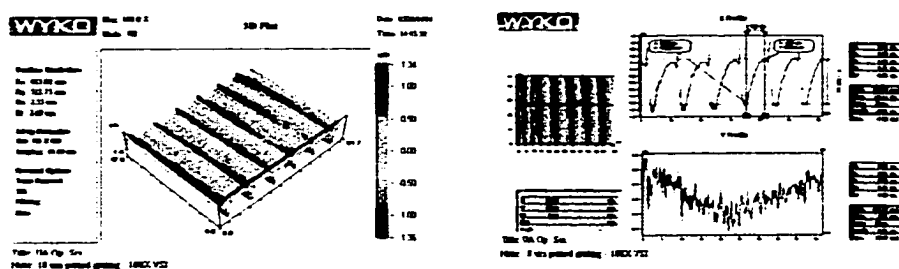
Figure 6.12: **The 3-dimensional surface profile of a 10 micron period grating and its cross profiles.**
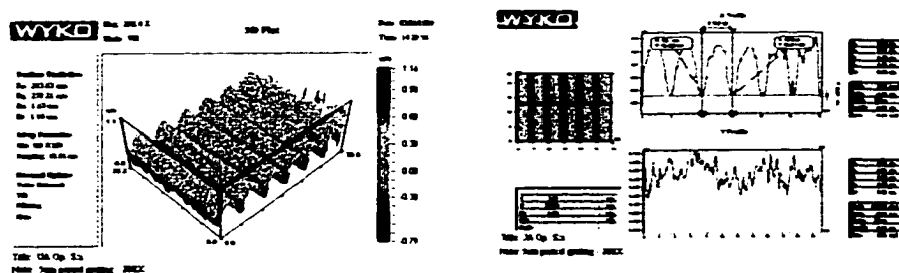
Figure 6.13: **The 3-dimensional surface profile of a 5 micron period grating and its cross profiles.**

operator's intervention, such as setting the total energy curve as the merit function to determine the starting positions of the phase unwrapping process. Choosing an appropriate merit function for a surface can be implemented on software after we have enough experience finding reliable surface positions which possess large SNRs.

In Chapter 3 the influence of the phase change upon reflection has been discussed; the shape of the coherence envelope is preserved, although the peak position is shifted depending on the functional form of the phase dispersion curve. We are not able to verify our theory experimentally due to the lack of dissimilar material samples. Therefore it would be one of our future goals to complete a calibration table for dissimilar materials as proposed in Chapter 3.

REFERENCES

[1] K. Hibino, B. F. Oreb, D. I. Farrany and K. G. Larkin, *Phase shifting for nonsinusoidal waveforms with shifting errors*, J. Opt. Am. A. **12** (1995), 761–768.

[2] J. H. Bruning, D. R. Herriott, J. E. Gallagher, D. P. Rosenfeld, A. D. White and D. J. Brangaccio, *Digital wavefront measuring interferometer for testing optical surfaces and lenses*, Appl. Opt. **13** (1974), no. 11, 2693–703.

[3] J. M. Combes, A. Grossmann and P. Tchamitchian, *Wavelets : time-frequency methods and phase space*, Springer-Verlag, Berlin and New York, 1989.

[4] A. Harasaki, and J. C. Wyant, *Fringe modulation skewing effect in white light vertical scanning interferometry*, Appl. Opt. (1999), submitted.

[5] C. Ai and E. L. Novac, *Centroid approach for estimating modulation peak in broad-bandwidth interferometry*, U.S. Patent # 5,633,715 (May 27, 1997; filed May 19, 1996).

[6] P. Hariharan, B. L. Oreb and T. Eiju, *Digital phase-shifting interferometry: a simple error-compensating phase calculation algorithm*, Appl. Opt. **26** (1987), no. 13, 2504–2506.

[7] N. Balsubramanian, *Optical system for surface topography measurement*, U.S. Patent #4,340,306 (July 20,1982; filed February 4,1980).

[8] James R. Benford, *Applied Optics and Optical Engineering vol. III, R. Kingslake Ed.*, ch. Microscope, pp. 145–183, Academic Press, New York and London, 1960.

[9] Max Born and Emil Wolf, *Principle of Optics*, Pergamon Press, New York, 1980.

[10] B. Bowe and V. Toal, *White light interferometric surface profiler*, Opt. Eng. **37** (1998), 1796–1799.

[11] C. J. R. Sheppard and K. G. Larkin, *Effect of numerical aperture on interference fringe spacing*, Appl. Opt. **34** (1995), no. 22, 4731–4734.

[12] P. J. Caber, *Interferometric profiler for rough surface*, Appl. Opt. **32** (1993), 3438–3441.

[13] Fang Cheng Chang and Gordon S. Kino, *325-nm interference microscope*, Appl. Opt. **37** (1998), 3471–3479.

[14] Y. Y Cheng and J. C. Wyant, *Two-wavelength phase shifting interferometry*, Appl. Opt. **23** (1984), 4539–4543.

[15] S. S. C. Chim and G. S. Kino, *Three-dimensional image realization in interference microscopy*, Appl. Opt. **31** (1992), no. 14, 2550–2553.

[16] G. Q. Xiao, T. R. Corle and C. G. Kino, *Real-time confocal scanning optical microscope*, Appl. Phys. Lett. **53** (1990), 716–718.

[17] K. Creath, *Calibration of numerical aperture effects in interference microscope objectives*, Appl. Opt. **28** (1989), no. 15, 3333–3338.

[18] Katherine Creath, *Progress in Optics vol. 26, E. Wolf Ed.*, ch. Phase-measurement interferometry techniques, pp. 349–393, Elsevier Science Publishers, Amsterdam, 1988.

[19] M. Hart, D. G. Vass and M. L. Begbie, *Fast surface profiling by spectral analysis of white-light interferograms with fourier transform spectroscopy*, Appl. Opt. **37** (1998), no. 10, 1764–1769.

[20] P. de Groot, *Derivation algorithms for phase-shifting interferometry using the concept of a data-sampling window*, Appl. Opt. **34** (1995), 4723–4730.

[21] P. J. de Groot, *Extending the unambiguous range of two-color interferometers*, Appl. Opt. **33** (1994), 5948–5953.

[22] L. Deck and P. de Groot, *High-speed noncontact profiler based on scanning white-light interferometry*, Appl. Opt. **33** (1994), no. 31, 7334–7338.

[23] P. Sandoz, R. Devillers and A. Plata, *Unambiguous profilometry by fringe-order identification in white-light phase-shift interferometry*, J. mod. Optics **44** (534), no. 3, 519.

[24] Jack. D. Gaskill, *Linear Systems, Fourier Transforms, and Optics*, John Wiley & Sons, New York, 1978.

[25] Joseph W. Goodman, *Introduction to Fourier Optics, Second Edition*, ch. 6 Frequency Analysis of Optical Imaging, pp. 126–171, McGraw-Hill, New York, 1996.

[26] P. Hariharan and M. Roy, *White-light phase-stepping interferometry: measurement of the fractional interference order*, J. Mod. Optics **42** (1995), 2357–2360.

[27] John Hayes, *Applied Optics and Optical Engineering vol. XI*, R. R. Shannon and J. C. Wyant Ed., ch. Fast Fourier Transformations and Their Applications, pp. 56–123, Academic Press, New York and London, 1991.

[28] J. C. Wyant, *Optical sciences course chapter notes*, ch. Phase Shifting Interferometry, personal homepage, www.optics.arizona.edu/jcwyant, 1998.

[29] J. Hardy, J. Feinleib, and J. C. Wyant, *Real time phase correction of optical imaging systems*, OSA Topical Meeting on Opt. Propagation through Turbulence (Boulder, Colorado), July 1975, p. 2622.

[30] A. Harasaki, J. Schmit and J. C. Wyant, *Improved vertical scanning interferometry*, Appl. Opt. (1999), submitted.

[31] A. Jendral and O. Bryngdahl, *Synthetic near-field holograms with localized information*, Opt. Lett. **20** (1995), 1204.

[32] K. Creath, *Step height measurement using two-wavelength phase-shifting interferometry*, Appl. Opt. **26** (1987), 2810–2816.

[33] C. G. Kino and G. Q. Xiao, *Scanning Optical Microscope, T. Wilson Ed.*, ch. Real-Time Scanning Optical Microscopes, Pergamon, London, 1990.

[34] G. S. Kino and S. S. C. Chim, *Mirau correlation microscope*, Appl. Opt. **29** (1990), no. 26, 3775–3783.

[35] K. G. Larkin, *Effective nonlinear algorithm for envelop detection in white light interferometry*, J. Opt. Am. A. **13** (1996), no. 4, 832–843.

[36] B. S. Lee and T. C. Strand, *Profilometry with a coherence scanning microscope*, Appl. Opt. **29** (1990), 3784–3788.

[37] S. Suja Helen, M. P. Kothiyal, and R. S. Sirohi, *Phase shift by a rotating polarizer in white-light interferometry for surface profiling*, J. Mod. Optics **46** (1999), 993–1001.

[38] Daniel Maracara (ed.), *Optical shop testing*, ch. Phase Shifting Interferometers, pp. 501–598, Jon Wiley & Sons, New York, 1992.

[39] M. Davidson, K. Kaufman, I. Mazor and F. Cohen, *An application of interference microscope to integrated circuit inspection and metrology*, Proc. Soc. Photo-Opt.

Instrum. Eng. **775** (1987), no. Integrated Circuit Metrology, Inspection, and Process Control, 233–241.

[40] note 1, Rough surfaces have local steep slops, which result in narrow fringe spacings, so that the condition of two detector per fringe is easily violated. Comparing to step height which consists of smooth surfaces and step discontinuities the surface profile obtained by the two-wavelength phase-shifting interferometer technique is less accurate.

[41] note 2, Please refer to Fig. 6.2. The interferogram is taken every $90°$ ($270°$) corresponding to $\frac{\lambda}{4}$ ($\frac{3\lambda}{4}$) distance. The frame position with largest modulation contrast (best-focus frame position) should be found to minimize focus error and the fractional phase is measured from the best-focus position.

[42] note 3, The coherence length of the unfiltered tungsten light source is 1.2 microns and after 80 nm band pass filter at center wavelength of 600 nm, the coherence length is 2.2 microns which is limited by the numerical aperture of the 50X objective rather than the filter bandwidth[34].

[43] note 4, provided by Raviv Levy in Professor Michael Descour's research group at OSC/UA.

[44] note 5, measured and provided by Dr. Eric Novac of Veeco Corporation.

[45] P. A. Reinholdsten and B. T. Khuri-Yakub, *Three-dimensional image processing for acoustic microscopy*, Proc. IEEE, B. R. McAvoy Ed. **1113** (1988), no. 2, 757–761.

[46] P. Carré, *Installation et utilisation du comparateur photoelectrique et interferentiel du bureau international des poids de mesures*, Metrologia **13** (1966), 13.

[47] P. de Groot, *Derivation algorithms for phase-shifting interferometry using the concept of data-sampling window*, Appl. Opt. **34** (1995), no. 22, 4723–4730.

[48] D. K. Cohen, P. J. Caber and C. P. Brophy, *Rough surface profiler and method*, U.S. Patent #5,133,601 (July 28,1992; filed June 12,1991).

[49] H. D. Polster, J. Pastor, R. M. Scott, R. Crane, P.H Langenbeck, R. Pilston and G. S. O. Steinberg, *New developments in interferometry*, Appl. Opt. 8 (1969), no. 3, 521–556.

[50] J. R. Schwider, R. Burow, K. E. Elssner, J. Grzanna, R. Spolaczyk and K. Merkel, *Digital wavefront measuring interferometry: Some systematic error sources*, Appl. Opt. 22 (1983), 3421.

[51] Lawrence R. Rabiner and Bernard Gold, *Theory and Application of Digital Signal Processing*, ch. 2.26 The Discrete Hilbert Transform, pp. 67–73, Prentice-Hall, Englewood Cliffs, N. J., 1975.

[52] R. J. Recknagel and G. Notni, *Analysis of white light interferograms using wavelet methods*, Opt. Commun. 148 (1998), 122–128.

[53] B. Richards and E. Wolf, *Electromagnetic diffraction in optical systems: Ii. structure of image field in an aplanatic system*, Proc. Soc. London Ser. A 253 (1959), 358–379.

[54] P. Sandoz, *Wavelet transform as a processing tool in white-light interferometry*, Opt. Lett. 22 (1997), no. 14, 1065–1067.

[55] J. Schmit and K. Creath, *Extended averaging technique for derivation of error-compensating algorithm in phase shifting interferometry*, Appl. Opt. 34 (1995), no. 19, 3610–3619.

[56] J. Schmit and K. Creath, *Window function influence on phase error in phase-shifting algorithms*, Appl. Opt. 35 (1996), no. 28, 5642–5649.

[57] T. G. Dresel and H. Venzke, *Three-dimensional sensing of rough surfaces by coherence rader*, Appl. Opt. 31 (1992), no. 7, 919–925.

[58] Kunio Turuta, *Pencil of Ray*, vol. 3, ch. Three dimensional imaging theory, pp. 391–433, New Technology Communications, Tokyo, 1993.

[59] T. Wilson and C. J. R. Sheppart, *Theory and Practice of Scanning Optical Microscope*, Academic, New York, 1984.

[60] J. C. Wyant, *Use of an ac heterodyne lateral shear interferometer with real-time wavefront correction systems*, Appl. Opt. **14** (1975), no. 11, 2622–2626.

[61] J .C. Wyant, *Phase-shifting interferometry*, www.optics.arizona.edu/jcwyant, September 1999, in Adobe .pdf file.

[62] J. C. Wyant and K. Creath, *Two-wavelength phase-shifting interferometer and method*, U.S. Patent #4,832,489 (May 23, 1989; filed March 19, 1986).

[63] J. C. Wyant and J. Schmit, *Computerized interferometric measurement of surface microstructure*, Proc. Soc. Photo-Opt. Instrum. Eng. **2782** (1996), 26–37.

[64] James. C. Wyant, Measurement of surface microstructure (Optical testing short course, 1998).